SPATIAL DIVERSITY IN A SIMO-OFDM HYBRID POWERLINE-WIRELESS SYSTEM

by

Kealeboga Mokise

Submitted in partial fulfillment of the requirements for the degree
Master of Engineering (Electronic Engineering)

in the

Department of Electrical, Electronic and Computer Engineering
Faculty of Engineering, Built Environment and Information Technology

UNIVERSITY OF PRETORIA

October 2019

SUMMARY

SPATIAL DIVERSITY IN A SIMO-OFDM HYBRID POWERLINE-WIRELESS SYSTEM

by

Kealeboga Mokise

Supervisor(s):	Prof. HC Myburgh
Department:	Electrical, Electronic and Computer Engineering
University:	University of Pretoria
Degree:	Master of Engineering (Electronic Engineering)
Keywords:	Spatial diversity, power line communication, multiple antenna wireless system, hybrid powerline-wireless channel, orthogonal frequency division multiplexing, selection combining, maximal ratio combining, equal gain combining, spatial correlation.

Spatial diversity is an effective diversity technique used in multiple antenna wireless systems. It requires that antenna elements be sufficiently distributed by at least ten times the signal wavelength (10λ). Sufficient spatial distribution of antenna elements renders performance improvements through diversity gain. In consumer electronics, antenna elements are often located in close proximity, $< \lambda$, due to form size constraints. Therefore performance improvement through spatial diversity is limited even though multiple antenna systems are employed. The work in this dissertation addresses the use of power line communication as a method to spatially distribute antenna elements of a multiple antenna wireless system. Addressing this problem requires the cooperative use of both wireless and powerline channels to form a hybrid channel.

A hybrid powerline-wireless channel is defined as the concatenation of a powerline channel and a wireless channel to establish a unified channel. A sequence-based channel sounding approach using maximum length sequences and software-defined radio was designed, implemented and applied to attain channel transfer characteristics of the hybrid channel. The measurement campaign was carried out for an indoor low-voltage level powerline network. The attained results include the channel impulse responses, frequency responses and power delay profiles. Coherence bandwidth, average channel attenuation and power delay profile timing delays are channel parameters that were extracted from the measurements. The extracted channel parameters reveal that the hybrid channel is a challenging medium for data transfer and communication applications.

Based on the attained hybrid channel characterisation parameters, a physical layer structure for a 1×2 single-input multiple-output orthogonal frequency division multiplexing (SIMO-OFDM) hybrid powerline-wireless system was designed and implemented. An investigation of the bit-error-rate performance of single-carrier and multi-carrier modulation for a multipath powerline channel was carried out in simulation. Using OFDM as a suitable candidate for multi-carrier modulation, it was found to outperform single-carrier modulation. OFDM was used as the channel access method for the hybrid channel. Source encoding and decoding of the physical layer structure was designed to be robust against inherent interferences of the hybrid channel. Selection combining, equal gain combining and maximal ratio combining methods were designed and implemented. Estimation methods for error rate, data transfer rate and SNR of the SIMO-OFDM system were designed and implemented. Capacitive signal coupling was used to interface the powerline channel to the wireless propagation environment, hence establishing the hybrid channel. This method also allowed powerline transmission to be performed at a much lower frequency than wireless transmission.

An experiment was conducted to investigate the effect of spatial distribution on the 1×2 SIMO-OFDM hybrid powerline-wireless system for indoor environments. The results of the experiment were error rate curves produced for different spatial distribution lengths through a powerline channel for each signal combining method. Error rate performance improvements in the SIMO-OFDM system were achieved with an increase of antenna element spatial distribution due to lowered signal envelope correlation. Small but yet notable diversity gains were observed by the increase in the slope of the produced error rate and signal-to-noise ratio curves for each signal combining method. Experimental parameters and apparatus placed a limitation on the achievable spatial distribution of diversity branches, hence the achievable diversity gains. This was a result of overwhelming inherent interferences of the hybrid channel.

ACKNOWLEDGEMENTS

I would like to thank my supervisor Dr. H.C. Myburgh for his guidance and support.

I extend my gratitude to CeTEIS and Huawei Technologies for their financial support.

To my family, my friends and fellow students, thank you for believing in me. This would not have been possible without the love you have shown me, the endless support you have given me and the constant source of inspiration you are to me.

LIST OF ABBREVIATIONS

AWGN	Additive white Gaussian noise.
BER	Bit error rate.
BM	Branch metric.
BPSK	Bipolar phase shift keying.
CFO	Carrier frequency offset.
CP	Cyclic prefix.
CRC	Cyclic redundancy check.
DFT	Discrete Fourier Transform.
DSSS	Direct sequence spread spectrum.
EGC	Equal gain combining.
FCS	Frame check sequence.
FEC	Forward error correction.
FFT	Fast Fourier Transform.
FSM	Finite state machine.
I	In-phase.
ICI	Inter carrier interference.
ISI	Inter symbol interference.
ISM	Industrial Scientific and Medial.
LFSR	Linear feedback shift register.
LOS	Line of sight.
MIMO	Multiple-input multiple-output.
MISO	Multiple-input single-output.
MLS	Maximal length sequence.
MRC	Maximal ratio combining.
MSRG	Multiple shift register generator.
OFDM	Orthogonal frequency division multiplexing.
PAPR	Peak-to-average power ratio.
PDF	Power distribution function.
PDP	Power delay profile.
PHY	Physical layer.

PLC	Power line communication.
PM	Path metric.
PRBS	Pseudorandom binary sequence.
PSD	Power spectral density.
Q	Quadrature-phase.
QAM	Quadrature amplitude modulation.
QPSK	Quadrature amplitude shift keying.
RMS	Root-mean-square.
SC	Selection combining.
SDR	Software-defined radio.
SIMO	Single-input multiple-output.
SISO	Single-input single-output.
SNR	Signal to noise ratio.
SSRG	Simple shift register generator.
STC	Space-time coding.
STC	Space-time block coding.
STDCC	Swept time delay cross-correlation.
STO	Symbol timing offset.

TABLE OF CONTENTS

CHAPTER 1 INTRODUCTION **1**
1.1 RESEARCH MOTIVATION 1
1.1.1 PROBLEM STATEMENT 3
1.2 RESEARCH QUESTIONS 4
1.3 RESEARCH OBJECTIVES 4
1.4 HYPOTHESIS 4
1.5 METHODOLOGY 5
1.6 CONTRIBUTIONS 5
1.7 RESEARCH OUTPUTS 6
1.8 OVERVIEW 6

CHAPTER 2 LITERATURE STUDY **9**
2.1 CHAPTER OVERVIEW 9
2.2 POWER LINE COMMUNICATION 9
2.2.1 Powerline channel impairments 12
2.3 DIVERSITY TECHNIQUES 16
2.4 HYBRID POWERLINE-WIRELESS CHANNEL 20

CHAPTER 3 PERFORMANCE ANALYSIS OF POWER LINE COMMUNICATION AND DIVERSITY TECHNIQUES **25**
3.1 CHAPTER OVERVIEW 25
3.2 POWERLINE CHANNEL NOISE INTERFERENCE 26
3.2.1 Middleton's Class A noise model 26
3.3 SINGLE-CARRIER AND MULTI-CARRIER MODULATION BER ANALYSIS 27
3.3.1 BER performance of single-carrier in a powerline channel 29
3.3.2 BER performance of multi-carrier in a powerline channel 30

3.3.3 Simulations 32
3.4 TRANSMIT AND RECEIVE DIVERSITY 39
3.4.1 Receive diversity 39
3.4.2 Transmit diversity 44
3.4.3 Simulations 46
3.5 SPATIAL CORRELATION AND MUTUAL COUPLING 48
3.5.1 Effects of spatial correlation 48
3.5.2 Effects of spatial correlation and mutual coupling 50
3.5.3 Simulations 54
3.6 CHAPTER SUMMARY 57

CHAPTER 4 POWERLINE-WIRELESS HYBRID CHANNEL CHARACTERISATION 58
4.1 CHAPTER OVERVIEW 58
4.2 CHANNEL SOUNDING METHODS 59
4.2.1 Channel sounding for frequency-domain 59
4.2.2 Channel sounding for time-domain 60
4.3 POWERLINE-WIRELESS HYBRID CHANNEL 64
4.4 CHANNEL SOUNDING METHOD 66
4.4.1 Pseudorandom binary sequence generator 66
4.4.2 Correlative sounder impulse response 69
4.4.3 Correlative sounder implementation 72
4.4.4 Correlative sounder analysis 75
4.5 PARAMETER ESTIMATION 80
4.5.1 RMS-DS 81
4.5.2 Coherence bandwidth 81
4.5.3 Average channel attenuation 83
4.6 HYBRID CHANNEL PERFORMANCE 83
4.7 SUMMARY 90

CHAPTER 5 SIMO-OFDM HYBRID POWERLINE-WIRELESS SYSTEM PHYSICAL LAYER DESIGNS AND IMPLEMENTATIONS 92
5.1 CHAPTER OVERVIEW 92

5.2 OFDM OVERVIEW 94
    5.2.1 OFDM modulation 95
    5.2.2 OFDM demodulation 96
5.3 OFDM SYSTEM 97
    5.3.1 OFDM symbol 98
    5.3.2 Source encoding and decoding 102
    5.3.3 Synchronisation 107
    5.3.4 Channel estimation and equalisation 109
    5.3.5 Sub-carrier allocation 111
    5.3.6 Data rate and error rate 112
5.4 SIMO-OFDM SYSTEM SIGNAL COMBINING 115
    5.4.1 Selection combining 117
    5.4.2 Maximal ratio combining 118
    5.4.3 Equal gain combining 120
    5.4.4 Diversity gain 122
5.5 GNU RADIO SOFTWARE AND HARDWARE IMPLEMENTATIONS . . . 123
    5.5.1 SIMO-OFDM transmitter 124
    5.5.2 SIMO-OFDM receiver 126
    5.5.3 BladeRF SDR hardware architecture 128
5.6 HYBRID POWERLINE-WIRELESS CHANNEL COUPLING 131
5.7 CHAPTER SUMMARY 136

CHAPTER 6 SIMO-OFDM HYBRID POWERLINE-WIRELESS SYSTEM RESULTS 137
6.1 CHAPTER OVERVIEW 137
6.2 SIMO-OFDM HYBRID POWERLINE-WIRELESS SYSTEM EXPERIMENT 138
6.3 SIMO-OFDM WIRELESS SYSTEM ERROR RATE PERFORMANCE . . . 140
6.4 SIMO-OFDM HYBRID POWERLINE-WIRELESS SYSTEM ERROR RATE PERFORMANCE 142
6.5 SIMO-OFDM HYBRID POWERLINE-WIRELESS SYSTEM THROUGHPUT 147
6.6 CHAPTER SUMMARY 148

CHAPTER 7 CONCLUSIONS 150
7.1 RESEARCH OUTCOMES 150

7.2 FUTURE WORK 152

REFERENCES 153

CHAPTER 1 INTRODUCTION

1.1 RESEARCH MOTIVATION

Wireless communication systems are often faced with the challenge of multipath fading. Multipath signal propagation is a result of radio signals' interaction with obstructions such as trees, mountains, vehicles and buildings. Multiple replicas of the same signal arrive at the receiver with various attenuation levels, phase-shifts and delays. Superposition of the replicas can be constructive or destructive resulting in random fluctuations of the signal strength. This phenomenon is referred to as multipath fading [1–3]. Fading effects can be described by either Rayleigh, Rice, Nakagami-m, Nakagami-q or Weibull distributions [1]. The Rayleigh distribution is used when a strong line-of-sight (LOS) component between the transmitter and receiver is absent, typically found in urban environments. In the presence of a LOS component, the Rice model is used, which is typical for inner-city and suburban areas. The Nakagami and Weibull distributions best describe the variations in instantaneous signal strength at the receiver.

Employing multiple antenna elements transforms the wireless channel into a multiple-input multiple-output (MIMO) channel. Signal diversity invoked in a MIMO channel can effectively mitigate multipath fading effects [4]. Signal diversity refers to multiple identical replicas of the same information-carrying signals that are transmitted from multiple antenna elements and received by multiple antenna elements, and this facilitates improved signal reliability in the presence of fading [5, 6]. Diversity techniques can effectively mitigate fading effects based on the analysis that the probability that multiple signal replicas in multiple statistically independent fading channels will simultaneously experience deep fading is very low. Employing multiple antenna elements means that signal diversity can be achieved at both the transmitter and receiver, namely transmit diversity and receive diversity, respectively.

Transmit diversity is achieved by channel encoding, such as Space-Time Coding (STC). STC introduces redundancy in space dimension by the addition of multiple antenna elements and in time dimension by channel encoding. Receive diversity is achieved by employing diversity combining techniques such as selection-combining (SC), maximal ratio combining (MRC) and equal-gain combining (EGC). SC offers the simplest diversity combining method whereby the received signals' signal-to-noise (SNR) from N diversity branches is estimated, and the signal with the highest SNR is selected for decoding. MRC offers coherent combining whereby the received signals are weighted according to their instantaneous SNRs and then co-phased before they are linearly combined. MRC is an optimal combiner at the cost of increased receiver complexity. While SC is much simpler and cheaper to implement, it offers the worst performance. EGC also offers coherent combining through signal co-phasing, but the same weight is used to combine the signals. EGC offers performance improvement over SC, but it is still inferior to MRC [7, 8].

Signal diversity in multiple antenna wireless systems can be realised in many forms. Spatial diversity is the most attractive because it does not incur excess time and frequency resources. Spatial diversity requires that the receive antennas be sufficiently distributed by at least ten times the signal wavelength (10λ) in order to attain independence of signal propagation paths [4]. Finite separation of antenna elements has been observed to improve output SNR for multiple antenna wireless systems. However, a computational burden is placed on the receiver because diversity combining techniques need to be used [9]. Considering spatial diversity, power line communication (PLC) can be used as a technique to achieve increased diversity branch independence and reduced signal decorrelation through larger antenna element spatial distribution [10, 11]. In most consumer electronic devices, separation of antenna elements is limited by form sizes, thus limited spatial diversity is achieved. Various PLC standards such as Homeplug 1.0, Homeplug AV2, Homeplug Green PHY and Homeplug Access BPL implement PLC as Ethernet access points. To the best of the author's knowledge, after an extensive literature review, multiple antenna wireless systems with diversity branch spatial distribution via a powerline channel has not yet been attempted.

Enhancement of spatial diversity in multiple antenna wireless systems through a powerline channel requires cooperative use of both powerline and wireless channels. Therefore, hybridism must be employed to achieve the goal of enhanced spatial diversity. Hybridism of a powerline channel and a wireless channel is inspired by the channel commonalities shared by the two channels, such as multipath propagation behaviour, wideband frequency selectivity and fading characteristics. The configuration of a hybrid powerline-wireless channel can either be in serial or in parallel form. Two distinct paths are used simultaneously to establish a link from the transmitter to the receiver in a parallel configuration. A serial hybrid powerline-wireless system is established by concatenating the powerline and wireless channel to form a unified channel. The spatial distribution of antenna elements in wireless systems through a powerline channel requires the use of a serial hybrid powerline-wireless channel. The parallel hybrid channel has received considerable attention in literature [12–17] compared to the serial hybrid channel [18–20]. Therefore, there is a considerable lack of attention in literature on characterisation of serial hybrid powerline-wireless channels owing to the challenges of such channels for broadband applications. Furthermore, no attention is given to the application of such channels in multiple antenna wireless systems.

1.1.1 PROBLEM STATEMENT

Multipath fading severely deteriorates wireless channel transfer characteristics. Diversity techniques are an effective solution to mitigate fading effects in multiple antenna systems. Amongst forms of achieving diversity, spatial diversity is the most attractive because it does not incur excess time and spectral resources. Spatial diversity requires that antenna elements be sufficiently separated by at least ten times the signal wavelength (10λ) in order to achieve independent signal propagation paths [4]. Antenna element separation can be effectively improved by utilising powerline communication methods, thereby obviating the need for additional infrastructure.

Powerline networks were originally designed to carry high-voltage low-frequency waveforms, not low-voltage high-frequency signals. Therefore, powerline channel data transfer and communication applications are met with two main challenges, multipath signal propagation and noise interferences of the powerline channel. The channel exhibits multipath behaviour as a result of impedance mismatches at discontinuities, which results in channel frequency selectivity [21]. Powerline cable losses cause high attenuation and low-pass transfer characteristics, which limit both coverage of the network and usable bandwidth [22].

To the best of the author's knowledge, after an extensive literature review, multiple antenna wireless systems with antenna element spatial distribution via a powerline channel have not yet been attempted. Thus, the problem to be addressed is spatial diversity in a multiple antenna wireless system using PLC methods to achieve sufficient antenna element spatial distribution.

1.2 RESEARCH QUESTIONS

The following questions will be addressed in this dissertation in order to solve the posed problem.

- What are the effects of a serial powerline-wireless hybrid channel on high-frequency low-voltage information-carrying signals ?
- How can power line communication be used as a method to spatially distribute antenna elements of a multiple antenna wireless system to render spatial diversity ?
- How is the error rate performance of a multiple antenna wireless system affected by the use of power line communication for antenna element spatial distribution ?

1.3 RESEARCH OBJECTIVES

The objectives of the research work are outlined as follows

- To study the channel transfer characteristics of indoor low-voltage powerline channels and multiple antenna wireless systems, thereby determining the influence of each propagation environment in a hybrid channel established by the concatenation of a powerline channel and a wireless channel.
- To characterise and analyse the channel transfer characteristics of a hybrid powerline-wireless channel, thereby determining the suitable channel access method for data transfer and communication applications.
- To implement a suitable physical layer structure for the hybrid powerline-wireless channel for data transfer and communication applications, thereby attaining error rate performance for such a hybrid system.

1.4 HYPOTHESIS

Spatial diversity in multiple antenna wireless systems renders improved system performance through diversity gain. The system performance in terms of error rate for a given SNR can be effectively improved. Spatial diversity requires that the receive antenna elements be sufficiently distributed by at least 10λ in order to achieve independent signal propagation paths [1,4,9]. PLC techniques provide an economical solution to achieve sufficient antenna element separation to attain signal propagation path independence. It is hypothesised that if PLC techniques are used to distribute antenna elements by at least 10λ, then error rate performance of a multiple antenna wireless system will be improved.

1.5 METHODOLOGY

In order to address the posed research questions and test the hypothesis, the research methodology to be conducted is first outlined.

A literature study is conducted to review the body of literature in the topics of multiple antenna wireless systems, power line communication and diversity techniques. Through this review process, a research gap is identified. The review process also serves to establish theoretical bases for the work to be done. Furthermore, it establishes contributions from previous works in order to show the significance of the work done. A quantitative analysis of the reviewed information is performed to establish tangible conclusions about the existing body of literature.

A characterisation of the hybrid powerline-wireless channel is performed using suitable measurement methods. Analysis of the attained channel measurements is performed to extract key channel performance parameters. Based on the analysis of the channel performance parameters, a physical layer structure is then designed and implemented for information transfer and communication in the hybrid channel.

The problem of spatial diversity in multiple antenna wireless systems is addressed by using power line communication as a method to spatially distribute antenna elements by at least 10λ. Software-defined radio is used to physically realise the proposed solution. Error rate and throughput are the performance metrics used to analyse the performance of the proposed solution.

1.6 CONTRIBUTIONS

The contributions of the dissertation are summarised as follows.

1. Investigation of the cooperative use of a powerline channel and wireless channel.

2. Characterisation of a hybrid powerline-wireless channel for data transfer and communication applications.
3. Use of power line communication as a technique to spatially distribute antenna elements in a multiple antenna wireless system for enhanced signal diversity.
4. Design and Implementation of a physical layer structure for information transfer and communication applications in a multiple antenna hybrid powerline-wireless system.
5. Investigation of the effects of powerline channel path length on diversity gain in a multiple antenna hybrid powerline-wireless system.

1.7 RESEARCH OUTPUTS

Research papers produced from work done in this dissertation are listed as follows

1. K. L. Mokise and H. C. Myburgh, "The Characterisation of Hybrid Powerline-Wireless Communication Channels," in *Proceedings of SATNAC*, Kwa-Zulu Natal, South Africa, 4-7 September, 2019.
2. K. L. Mokise and H. C. Myburgh, "Spatial Diversity In A SIMO-OFDM Hybrid Powerline-Wireless System," *EURASIP Journal on Advances in Signal Processing*, Submitted.

1.8 OVERVIEW

The rest of the dissertation is organised in six chapters outlined as follows.

Chapter 2 presents a literature review that aims to provide a general overview of power line communication, including the history and current advancements of the technology at large. Insight is given into powerline channel impairments such as noise interferences and powerline cable losses. Powerline channel modelling techniques aimed at describing the channel transfer characteristics are presented. Review of cooperative use of PLC and other access technologies is presented. Cooperative use of PLC and wireless access technologies for achieving signal diversity is presented in more detail. The current challenges of parallel and serial configurations of powerline and wireless channels, and the benefits thereof are presented in detail. Lastly, the chapter addresses signal diversity in multiple antenna communication systems and how a hybrid powerline-wireless channel can be used in multiple antenna wireless systems for enhanced signal diversity for indoor applications.

Chapter 3 presents quantitative analysis and simulations of power line communication and diversity techniques with the aim of determining the influence of powerline and wireless propagation environments in a hybrid channel. An investigation between single-carrier modulation and multi-carrier modulation for indoor low-voltage powerline channels under impulsive noise is conducted in simulation. Bit-error-rate performance is used to determine the influence of powerline channel noise interferences on single-carrier modulation and multi-carrier modulation for digital communications. The concept of signal diversity is further explored in this chapter through a quantitative analysis of diversity techniques. Signal combining techniques are essential for demodulation in multiple antenna wireless systems. Therefore bit-error-rate analysis of selection combining, equal gain combining and maximal ratio combining is presented in this chapter. Lastly, the effects of signal envelope correlation and mutual coupling in multiple antenna wireless systems are quantitatively presented in terms of bit-error-rate performance. The first objective of the research is achieved in this chapter.

Chapter 4 presents a channel sounding method used to characterise the hybrid powerline-wireless channel. A sequence-based channel sounding method using maximum length sequences and software-defined radio is used to attain channel transfer characteristics. Key channel parameters such as coherence bandwidth, average channel attenuation and power delay profile time parameters are extracted from the measurements. These key channel parameters highlight the potential and inherent limitations of such a hybrid channel. This chapter aims to achieve the second objective of the research work.

Chapter 5 presents the design of a physical layer structure to achieve communication and information transfer through the powerline-wireless hybrid channel. It is designed for a single-input multiple-output hybrid powerline-wireless system. The design of the physical layer structure aims to achieve robust error detection and correction against the impairments of the hybrid channel. Signal combining methods are designed and implemented. The realisation of the hybrid powerline-wireless system using software and hardware components is presented. Error rate and throughput estimation methods for the hybrid powerline-wireless system are designed and implemented. Signal coupling for information-carrying signals between the powerline and wireless channel to achieve link continuity in the hybrid powerline-wireless system is also presented. The third objective of the research is achieved in this chapter.

Chapter 6 presents the error rate performance of the physical layer structure with varying spatial distribution of receive antenna elements of the hybrid powerline-wireless system. Error rate performance is presented for selection combining, equal gain combining and maximal ratio combining techniques with varying spatial distributions. The results presented in this chapter aim to address the research question posed and to test the hypothesis.

Chapter 7 concludes the work done in this dissertation and provide avenues for further research.

CHAPTER 2 LITERATURE STUDY

2.1 CHAPTER OVERVIEW

This chapter aims to provide a general overview of power line communication, signal diversity, diversity techniques and an in-depth discussion of the research problem. Section 2.2 addresses PLC history and current advancements of the technology at large. Insight is given into impairments of powerline channels such as noise interferences, multipath signal propagation and powerline cable losses. Powerline channel modelling techniques aimed at describing the channel transfer characteristics are discussed. Section 2.3 presents signal diversity in wireless environments and diversity techniques in multiple antenna wireless systems. Section 2.4 addresses the cooperative use of powerline and wireless channels for achieving signal diversity. The prevailing challenges of parallel and serial configurations of the two channels and the benefits thereof are outlined. Signal diversity in multiple antenna communication systems and how a hybrid powerline-wireless channel can be used in multiple antenna wireless systems for enhanced signal diversity for indoor applications is discussed in-depth.

2.2 POWER LINE COMMUNICATION

Power line communication (PLC) can be described as a method of providing broadband services to residential homes and commercial buildings using existing power distribution networks. Since the 1990s, it has been emerging as a prominent alternative to provide broadband services to residential homes and commercial buildings with the advantage of meagre deployment costs due to the existence of powerline networks all over the world [22]. The ubiquity of power grids makes powerline communication a potential competitor of wireless communications because of low deployment cost [22]. However, the development of PLC technologies is not as progressive as that of wireless systems due to challenges of channel characterisation. The history of PLC dates back to as early as the 1800s, the first known patents for the first known PLC systems were registered in 1897 and 1901 in Britain and Germany, respectively [23]. PLC has been practiced for over a century but has only intensified since the 1990s by attracting researchers and engineering practitioners into the field. PLC was particularly attractive because the powerline infrastructure was widespread and penetrated into remote rural areas. In the 1920s the transmission of voice over high-voltage (HV) powerline cables was very popular. In the 1930s there was widespread use of powerline cables for information transfer using a technique called ripple control or ripple carrier signalling. This technique was used by utility companies for monitoring and load control purposes. However, ripple control operated below 3 kHz and required high transmission power. PLC is a more refined and sophisticated method to achieve monitoring and load control by utility companies, which can be extended to broadband internet access, multimedia and smart grid applications. Another advancement in the field of PLC was due to radio amateurs who experimented on powerline cables to have an alternative means of communication because, during World War II, governments had put in place strict restrictions on amateur radio broadcasting [23, 24].

PLC is categorised into broadband PLC and narrowband PLC. The latter is the earliest use of PLC technology, which achieves low data rates and longer range, while the former is the latest use of the PLC technology which achieves high data rates and shorter range. The use of PLC has an inverse relationship between data rates and communication range. Therefore it is the mission of the design engineer to perform trade-off analysis and attain data rates and communication range suitable for the particular application. Powerline networks were originally designed to carry low-frequency high-voltage waveforms and not high-frequency low-voltage signals. Therefore there are inherent hindrances present in powerline channels. Powerline channel inherited hindrances include powerline cables losses, multipath signal propagation and noise interferences.

Noise interferences can be classified into background noise and impulsive noise. The channel exhibits multipath signal propagation behaviour which is caused by reflections and transmissions resulting from impedance mismatches at discontinuities. The resulting fading characteristics due to multipath signal propagation causes the channel to be frequency selective [21]. Powerline cable losses cause high attenuations and low-pass transfer characteristics which limit both coverage of the network and usable bandwidth for information-carrying signals [22]. All these parameters are time, frequency and location-dependent, which makes PLC channel modelling a non-trivial and complicated task [25]. These inherent hindrances can be overcome by employing some system intelligence in the implementation of PLC systems. PLC technology has been standardised by various organisations, with the most popular and well-known standards being the HomePlug consortium, such as Homeplug 1.0, Homeplug AV2, Homeplug Green PHY and Homeplug Access BPL, each of which has its various benefits and shortcomings [23, 24].

A power grid is typically characterised into four layers, the high-voltage (HV) transmission network, the medium-voltage (MV) network, the low-voltage (LV) network and the indoor electrical distribution network found in residential homes and commercial buildings. Much of the research work in literature for broadband-PLC and powerline channel modelling is focused on the last two layers. There are two kinds of powerline channel modelling approaches that can be found in literature, the top-down approach [21, 26–28] and the bottom-up approach [29, 30]. The top-down approach is based on the multipath signal propagation behaviour of the powerline channel, it uses data fitting to find the best-fitted model from time-domain or frequency-domain measurements. The bottom-up approach is based on transmission line theory whereby the powerline network parameters are derived from first principles and are used to characterise the channel. The advantages of the top-down approach include easy adaption and allow for rapid channel generation. The approach is suitable for running Monte Carlo simulations for a large number of channel realisations. Top-down modelling allows for some channel statistics to be derived from measurements in order to study channel transfer characteristics analytically. This approach, however, has a limited degree of flexibility because the derived model and parameters are for specific powerline networks and frequency bands, and it is difficult to be applied to another powerline network. Another setback of this approach is the difficulty in describing spatial correlation in powerline networks, as such, it may not be applied in network system modelling [27]. The advantage of using the bottom-up modelling approach is that it can be flexibly applied to different situations as long as the powerline network information is perfectly known. The approach can also be used for network-related systems modelling such as multi-user and relay systems. The drawbacks of this approach include the computational complexity that grows with the network complexity, and it may not be practical since only key elements of the network are considered. The collection of the required information about network elements is a challenging task due to different powerline channel realisations overtime.

Different types of powerline channel noise sources are distinguished over powerline channels [31]. Noise interferences in the powerline channel can be classified into impulsive noise and background noise [32]. Noise interferences in powerline channels are a result of the corona effect, switching of loads that cause voltage spikes and electric arc or crosstalk between powerline cables [10]. The nature of background noise is found to have properties similar to white-noise, it is wideband with low power spectral density (PSD). Impulsive noise is the most detrimental noise type to PLC systems, it occurs in bursts and exhibits the highest PSD, which causes burst errors in information transmission. Impulsive noise can reach values of 50 dB above the background noise level and impulse widths can last a few microseconds to a few milliseconds [31]. Bit error rate (BER) performance of a wireless local area network (WLAN) channel in the presence of impulsive noise was investigated in [33]. The results show that impulsive noise deteriorates the BER performance of such a system more compared to background noise modelled as additive white Gaussian noise (AWGN). Therefore, powerline channel noise is a combination of white background noise and impulsive noise, which means that communication systems optimised for Gaussian channels may not necessarily perform well in powerline channels [34].

2.2.1 Powerline channel impairments

A typical link between the substation and the consumer does not have a point-to-point connection but instead consists of a series of powerline distribution cables and branching cables. Each of the branching cables represents a destination end node, these connections end at house connection boxes and are followed by indoor wiring. The indoor wiring represents a complex termination impedance from the point of view of the powerline network [21]. The indoor wiring consists of many branches, thus the impedance seen by the network is usually low. Due to the numerous connections, the impedance appears to be stationary as the impedance variations are minimal. The indoor wiring consists of many joints and terminal nodes that may be open-circuited or connected to different loads of different characteristic impedances, which in effect causes numerous signal reflections with different delays and amplitudes due to the impedance mismatches. In general, such a channel has similar features to that of the wireless fading channel in urban areas.

2.2.1.1 Multipath signal propagation

Consider a simple powerline T-network shown by Fig. 2.1. The network consists of a single branch between point D and B and a direct path from A to B to C. The line segments have lengths l_1, l_2 and l_3 with characteristic impedances Z_{l1}, Z_{l2} and Z_{l3} respectively. When a signal propagates in the network, it does not only propagate along the direct path from A to B to C, but reflections of the transmitted signal are also present, which causes multipath propagation behaviour that results in frequency selective behaviour of the channel. The terminals A and C are assumed to be matched, therefore the only points for reflections to occur are B and D, with the reflection factors denoted by r_{1B}, r_{3B} and r_{3D}, and the transmission factors denoted by t_{1B} and t_{3B}.

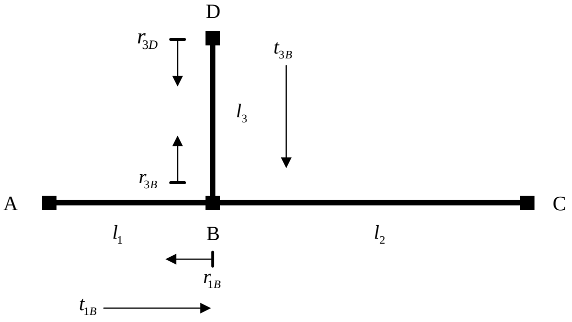

Figure 2.1. Multipath behaviour in a simple T-network.

An infinite number of signal propagation paths are possible due to reflections. Each propagation path has a gain factor g_i, which is a product of the transmission factors and the reflection factors [21]. The transmission and reflection factors are usually less than unity because perfect matching is rarely achieved in indoor powerline networks, therefore $|g_i| \leq 1$. Transmission only occurs at joints, meaning the characteristic impedance at a parallel connection is less than the impedance of the line feeding the joint of connections. The longer the path, the more transmissions and reflections occur along the path, hence g_i will be much lower. Therefore, longer paths contribute less to the overall strength of the received signal. Hence it is reasonable that the infinite number of possible paths be only approximated by a number of N dominant paths. The goal is to make the parameter N as small as possible [21, 35, 36]. The conducting cables also present losses that can be characterised by an attenuation component that is a function of frequency and cable length [21]. The individual paths are superimposed to give the received signal.

2.2.1.2 Powerline cable losses

The frequency response $H(f)$ of a matched transmission line of length l is given by the complex propagation constant [37, 38]

$$\gamma = \sqrt{(R' + j\omega L')(G' + j\omega C')} = \alpha + j\beta, \tag{2.1}$$

where $R^{'}$, $L^{'}$, $G^{'}$ and $C^{'}$ are the per-unit-length resistance (in Ω/m), inductance (in H/m), conductance (in S/m) and capacitance (in F/m) respectively. Broadband-PLC generally operates in the megahertz frequency range, at such high frequencies, the resistance $R^{'}$ is dominated by the conductor skin-effect. The skin-effect characterises how deep an electromagnetic (EM) wave can penetrate a conducting material and is proportional to $\sqrt{f}$ [21, 38]. The conductance $G^{'}$ is generally determined by the dissipation factor of the dielectric material, which is usually poly vynil chloride (PVC) and it is proportional to f. Given typical cable geometry and material properties, in practice, $R^{'} \leq \omega L^{'}$ and $G^{'} \leq \omega C^{'}$ in the frequency range of interest for broadband-PLC.

2.2.1.3 Powerline channel noise interferences

Noise interferences in a powerline channel are brought about by changing conditions in the powerline network. Studies conducted on powerline channel noise interferences classify the various noise interferences as follows [11, 31, 39]

1. Coloured background noise with comparatively low PSD that varies with frequency. A summation of different low power consumption noise sources is the primarily cause this type of noise. The PSD in this respect changes by periods of minutes or hours.
2. Narrowband noise. This noise type occupies several frequency bands, which are small and continuous over the frequency spectrum. Sinusoidal signals with a modulated amplitude that are a result of ingress broadcast stations cause this noise type. This noise type often changes through daytime due to changing levels amplitude modulated signals and becomes higher at night when the reflection properties of the atmosphere are stronger.
3. Periodic asynchronous impulsive noise. This noise type is asynchronous with the mains frequency with a repetition rate between 50 Hz to 200 kHz. It has a spectrum with discrete lines located in accordance with the impulse repetition rate. Switched power supplies are often the cause of this noise type. Because of the high repetition rate, it

occupies frequencies that are too close to each other and therefore builds frequency bundles that are usually approximated by narrow bands.

4. Periodic synchronous impulsive noise that is synchronous with the mains frequency with a repetition rate of 50 Hz to 100 Hz. The impulses have a short life span lasting in the range of milliseconds, and their PSD declines with frequency. Switching of rectifier diodes in switched power supplies causes this type of noise which is synchronised with the mains cycle.
5. Asynchronous impulsive noise is caused by changing loads in the powerline network, which causes transients. The impulses can last from a few milliseconds to a few microseconds, and they occur randomly as loads are switched. The PSD of this noise type can reach values of 50 dB above the background noise, making it the principal cause of errors in digital communications over powerline channels. Much of the impulsive noise research and modelling in literature focuses on this noise type.

The results of measurements in the conducted studies reveal that the first two noise types are generally stationary over long periods lasting seconds, minutes and even hours on some occasions. The two first noise types can be classified into one group, generally referred to as background noise. The last three noise types have root-mean-square (RMS) amplitudes that vary rapidly over periods of milliseconds and microseconds. These noise types are classified as impulsive noise. Therefore, noise interference in powerline channels can be considered as a summation of background noise and impulse noise. Background noise can be conveniently modelled as additive white Gaussian noise (AWGN) since it is observed to satisfy the same statistical properties as AWGN in wireless channels. Middleton's Class A noise model is a famous model used to describe the impulsive noise since it satisfies all the fundamentals of powerline channel noise and is not limited to signal modulation or channel type. The advantage of this model is that it can be used to model both background and impulsive noise since it generates both Gaussian and impulsive random variables. The impulsive index parameter of the model can be adjusted to make the model be more impulsive noise representative than Gaussian. However, Middleton's Class A model fails to capture the periodic nature of powerline channel impulsive noise.

2.3 DIVERSITY TECHNIQUES

The rich scattering nature of the wireless propagation environment can be exploited by employing multiple antenna elements at the transmitter and receiver to achieve signal diversity. The use of multiple antenna elements allows for implementation of different antenna element configurations for realising transmit diversity and receive diversity. Transmit diversity can be realised in multiple-input single-output (MISO) and multiple-input multiple-output (MIMO) wireless system configurations, while receive diversity can be realised in single-input multiple-output (SIMO) and also MIMO wireless system configurations. Meaning multiple replicas of the same information-carrying signal can be transmitted and received through multiple antenna elements, meaning there is always a chance of recovering the transmitted information through one or more of the signal replicas. This facilitates improved reception reliability in the communication system [4]. Performance improvement in multiple antenna systems communication is in the form of diversity gain and array gain. Array gain refers to the average increase in the SNR at the receiver that arises from the coherent combining effect of multiple signal replicas at the receiver. Array gain is realised when signal combining methods such as maximal ratio combining (MRC) and equal gain combining (EGC) are used for demodulation at the receiver. Diversity gain refers to the considerable reduction in signal amplitude variations of the combined signal compared to any signal at any one receive antenna element [40]. Diversity techniques effectively mitigate fading effects based on the analysis that the probability that multiple signal replicas in multiple independent propagation paths with different fading properties will simultaneously experience deep fading is very low [1,3,40]. Fig. 2.2 shows that in the absence of diversity ($M_R M_T = 1$), the signal suffers deep fades, but with an increase in the number of transmitter and receiver antenna elements $M_R M_T$, the depth of fades reduces considerably and the effective channel tightens. Meaning that the mean signal level improves with $M_R M_T$, due to diversity gain. In the ideal case of $M_R M_T \rightarrow \infty$ the channel is stabilised and approaches an ideal AWGN channel [1,40].

Signal diversity can be achieved in the form of frequency diversity, time diversity, spatial diversity, polarisation diversity and angle diversity. Time diversity is shown in Fig. 2.3(a), it allows for the same radio signal to be transmitted repeatedly at sufficiently separated time instances that are longer than multipath channel dispersion time. Similarly, in frequency diversity, as shown in Fig. 2.3(b), the same information-carrying signal is repeatedly transmitted at sufficiently separated frequency bands that are larger than the coherence bandwidth

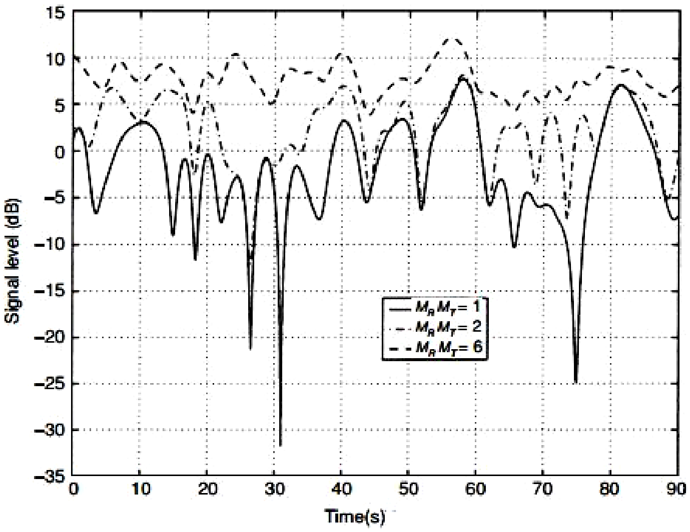

Figure 2.2. Communication link hardening through signal diversity.

of the channel, which is the reciprocal of the coherence time. Time diversity and frequency diversity methods are unattractive because they incur excess time and frequency resources. Spatial diversity requires that receive antenna elements be sufficiently separated by at least ten times the signal wavelength, 10λ, in order to achieve independent signal propagation paths. Polarisation diversity uses the fact that vertically and horizontally positioned antenna elements can be used to achieve independent signal propagation paths. Angle diversity uses angle variations in spatial dimensions of the receive antenna elements to receive the same radio signal from different angles.

The concepts of space-frequency diversity and space-time (spatial) diversity are illustrated by Fig. 2.3(c) and Fig. 2.3(d). These methods are the most viable and pragmatic solutions for multiple antenna wireless systems because they do not consume excess time or spectral resources [4, 41]. Spatial diversity allows for the transmitted radio signals to experience independent propagation paths in the wireless channel, which allows for the same degree of signal diversity as in time or frequency diversity. In [9], the effect of finite receive antenna elements separation was evaluated for output SNR performance of the receiver. Receive antenna elements separation was varied between 5λ, $\lambda/2$ and $\lambda/10$. The results show excellent output SNR for large separations, 5λ, due independent signal propagation, for smaller separations, the SNR performance was deteriorated due to EM coupling of received signals which results

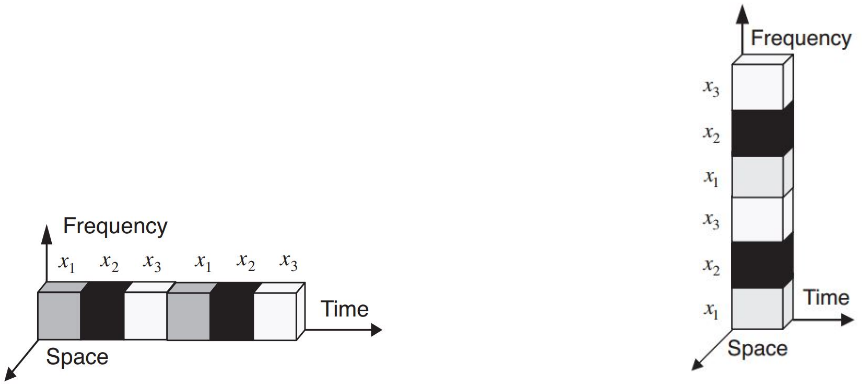

(a) Time diversity **(b)** Frequency diversity

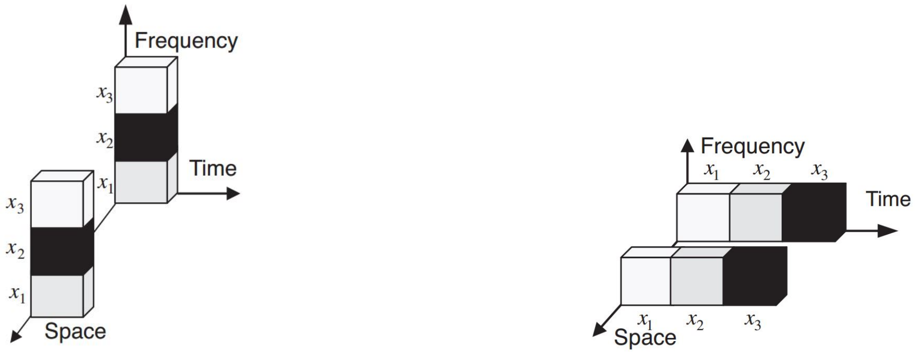

(c) Space-Frequency diversity **(d)** Space-Time diversity

Figure 2.3. Illustration of time, space and frequency diversity techniques

in high signal envelope correlation. A computational burden is placed on the receiver because diversity combining techniques need to be used for demodulation, which in turn increases the receiver complexity and could incur higher power consumption in practical multiple antenna systems.

The single-input single-output (SISO) communication model provides the simplest communication link between one transmit antenna and one receive antenna, as shown in Fig. 2.4(a). Diversity techniques cannot be applied to SISO systems. However, this case is included to highlight the significance of multiple antenna wireless systems. The SIMO communication system utilises one transmit antenna element and multiple receive antenna elements. Fig. 2.4(b) shows a simplified case for two receive antenna elements. Replicas of the transmitted signal will arrive at all the receive antenna elements through different propagation paths. It is assumed that each propagation path is completely decorrelated. Therefore the received signal at each diversity branch is independent. SIMO systems utilise receive diversity, meaning diversity combining techniques are needed. In a MISO system, the transmitter uses multiple transmit antenna elements and only one antenna element is used for reception. Fig. 2.4(c) shows a simplified case of two transmit antenna elements and one receive antenna element. Signal diversity is achieved by transmitting the same information-carrying signal from multiple antenna elements, thereby experiencing different propagation paths.

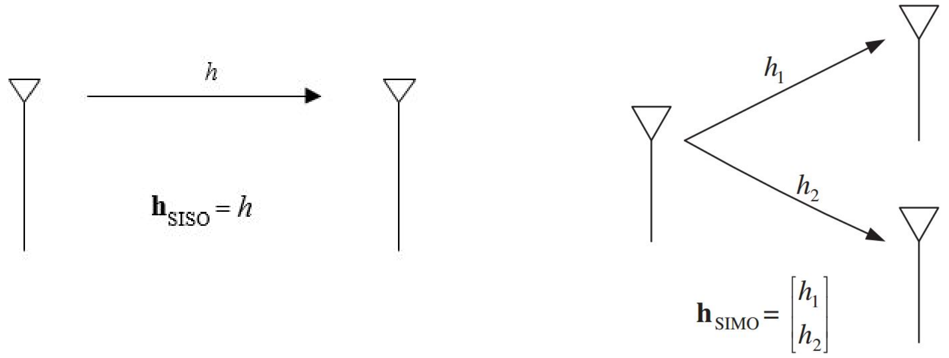

(a) SISO communication system configuration. **(b)** SIMO communication system configuration.

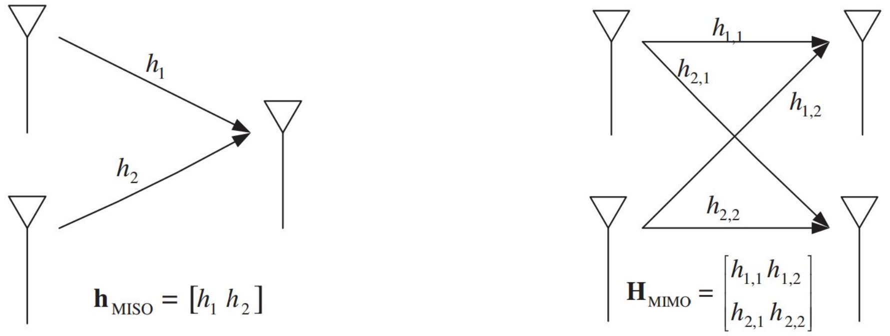

(c) MISO communication system configuration. **(d)** MIMO communication system configuration.

Figure 2.4. Configuration of multiple antenna wireless systems

The received signals are averaged at the single receive antenna element. Due to multiple transmit antenna elements, transmit diversity can be applied in MISO systems. Beamforming is the most effective form of transmit diversity for MISO systems. It refers to signal energy being directed to the receiver in specific dimensions, thereby increasing the received signal power and, consequently, the output SNR [40,42]. The signal quality improves with an increase of transmit antenna elements N_t. A MIMO system is a general multiple antenna wireless system whereby multiple antenna elements are used at both the transmitter and receiver. Fig. 2.4(d) shows a simplification of two transmit and two receive antenna elements. The highest degree of diversity can be achieved in MIMO systems due to the applicability of both transmit and receive diversity, leading to significant system performance improvement through both diversity gain and array gain. The same information-carrying signal is transmitted from multiple antenna elements, and each antenna element receives each signal through different propagation paths. For example, the signal from transmit antenna 1 reaches both receive antenna elements through propagation paths $h_{1,1}$ and $h_{2,1}$. In MIMO systems, transmit diversity can be achieved by using space-time coding (STC), more specifically space-time block coding (STBC). The Alamouti scheme is an optimal orthogonal STBC for a 2×2 $(N_r = 2, N_t = 2)$ MIMO system [5]. Due to the orthogonal property of the code, only linear processing is required at the receiver for decoding. This means linear diversity combining techniques such as MRC, SC and EGC can be used at the receiver.

2.4 HYBRID POWERLINE-WIRELESS CHANNEL

The convergence of communication technologies in next-generation networks will address the demands for high speed and reliable communication links by consumers. A single solution cannot address the growing demand, which inspires and motivates the cooperative use of multiple communication technologies. Power line communication leverages the existing powerline wiring infrastructure as a medium for data transfer and communication application. PLC requires minimal to no new infrastructure, and in this way, it shares many similarities as its wireless counterpart. One of the fundamental similarities between powerline and wireless communications is the broadcasting nature in the channels. It is evident from prevailing channel models, networking models and signal processing techniques of both powerline and wireless communications that both channels exhibit multipath signal propagation behaviour. Channel transfer characteristics of both PLC and wireless channels show commonalities in the fading characteristics. Fading refers to the variation of the signal amplitude over time and frequency, and it is categorised into fast fading and slow fading. The former is due to path loss of the signal as a function of the distance between transmitter and receiver, and the latter is due to the rapid variations in the transmitted signal. Multipath signal propagation behaviour in powerline channels is due to topology variations over time due to different loads and switching of loads, causing impedance mismatches and signal reflections. Powerline channel impairments can be overcome by employing hybridism with one or more viable access technologies.

Cooperative use of PLC and wireless, and PLC and visible light communication (VLC) are two methods that have gained traction in the research community over the past decade. Hybrid PLC-VLC communication systems have been a significant technological transition for the lighting industry in the past decade to become light-as-service providers. VLC technology uses the visible light spectrum to transmit data by modulating the intensity of the light-emitting diode (LED) illumination. VLC has become a potential contender of wireless communications due to the apparent reuse of existing LED fixtures common for indoor environments. It was found to outperform wireless communications in terms of the abundant available visible light spectrum and spatial reuse [43]. A pragmatic solution for VLC network deployment is the hybridism of PLC and VLC because existing powerline cables can be leveraged at each LED fixture. In a hybrid PLC-VLC system, PLC is used as a backbone of the communication infrastructure and VLC is used for broadcasting and connectivity. The focus of most studies [44–47] on hybrid PLC-VLC is on channel characterisation to solve VLC system impairments such as inability to penetrate opaque walls, signal interference due to the close proximity of LED fixtures in indoor environments and lack of mobility of VLC systems. Coordination methods have been proposed to address these issues, but with little to no improvement. Channel transfer characteristics also show that PLC systems outperform hybrid PLC-VLC system by several orders of magnitude [46]. Moreover, little to no attention has been given to signal diversity in hybrid PLC-VLC systems, and this is mainly due to a lack of heterogeneity of the information-carrying signal, thereby compromising the integrity of the data transfer or communication link.

The first discussion about powerline-wireless hybridism was held in 2005 [48], at the time hybridism was considered to be joining the two access technologies to work together. Both PLC and wireless systems have inherent hindrances and different environmental influences that can be overcome by a hybrid system. The environment in which a wireless system is immersed has a direct influence through interaction with the radio signals. Interaction of radio signals with objects in the environment causes reflection, refraction, diffraction, absorption and scattering of radio signals. Changes in the powerline network topology cause PLC impairments such as multipath signal propagation and noise interferences [11, 21]. The goal of hybrid systems is to improve communication link reliability by complementing the individual channel hindrances.

The configuration of a hybrid system can either be in serial or in parallel form, both system configurations have received some attention in literature [12–14, 18, 19]. In a parallel hybrid powerline-wireless system, two distinct paths are used simultaneously to establish a link from the transmitter to the receiver. Simultaneous use of two distinct paths enables the hybrid system to overcome the environmental limitations and enhance reliability than each of the paths used individually. This cooperative use of powerline and wireless channels from a transmitter to receiver now shifts the original discussion from just link reliability in interconnected access technologies to also include improved signal quality. The invoked signal diversity improves signal quality in the hybrid system. In a parallel system, diversity combining techniques are employed at the receiver to improve the output signal SNR. Significant research contributions have been made towards diversity combining of signals in a parallel powerline-wireless hybrid system [15–17]. It is shown that the parallel channel can have an additional benefit of multiplexing. In [17], coherent OFDM multi-carrier modulation was used for both PLC and wireless communication. Analytical solutions are derived and given for optimum combining (OC), saturated metric combining (SMC) and maximal ratio combining (MRC) diversity combining techniques. BER analysis and indoor measurements analysis shows that using a powerline-wireless channel for signal diversity improves the throughput of communication links. The work in [17] is extended by using differential modulation techniques and uses the unlicensed $902 - 928$ MHz band for wireless communication. The combining techniques were found to rely more on the PSD of the received signal, which alleviated the need for channel knowledge and reduced the complexity of a hybrid powerline-wireless system receiver considerably [15]. A comparison between modulation diversity and coding diversity for a parallel powerline-wireless system was presented in [49]. Modulation diversity refers to simultaneous transmission of the same coded information bits over both links. In coding diversity, half of the coded information bits are transmitted over one link and the half over another. A high link throughput was achieved by coding diversity than modulation diversity. However, keeping the data rate the same, a high degree of signal diversity was achieved with modulation diversity than coding diversity.

A serial hybrid powerline-wireless channel is established by concatenating a powerline channel and a wireless channel to form a unified channel. The channel transfer characteristics of the hybrid channel represents the concatenation of the powerline and wireless transfer characteristics. A measurement campaign was carried out in [19] using an OFDM modulation based channel sounding method to investigate and characterise the channel transfer characteristics of a hybrid powerline-wireless in the frequency range of 1.7 - 100 MHz. The attained results show that this type of channel is a challenging one and makes it an exciting research avenue. Firstly, the additive noise components in a powerline and a wireless channel cannot be modelled as the same random process due to varying statistics of the noise components and noise sources in each channel. Though both channels exhibit commonalities of multipath signal propagation and slow fading characteristics, the seen input impedance in powerline networks and wireless channels varies considerably. Therefore the coupling devices for powerline and wireless transceivers also vary considerably. In [20], a unified hybrid powerline-wireless system is investigated where a signal is injected into the powerline and using the fact that powerline cables are unshielded, the signal is radiated from a powerline cable and received through a mobile device. In the opposite direction, a mobile device radiates a signal which is received by the unshielded powerline cable and decoupled to a receiving device on the powerline network. The attained coherence bandwidth, average channel attenuation and RMS delay spread channel statistics in the study show that powerline to wireless transmission direction outperforms wireless to powerline transmission direction. The asymmetry of transmission directions is unfavourable for full-duplex systems. Channel relaying has been proposed to tackle the channel asymmetry issue of the hybrid channel. Amplify-and-forward (AF) and decode-and-forward are the prevailing relaying systems [50, 51]. An assumption made with relaying systems is that relay points are available in the network, which is not always the case for powerline networks and would require new infrastructure to achieve.

The serial hybrid powerline-wireless channel has advantages of mobility and larger coverage over the parallel hybrid channel. Parallel hybrid channel achieves high diversity gain due to the invoked signal diversity and use of diversity combining technique. It is also more reliable as the probability of link failure is less compared to that of the serial hybrid channel. The benefits of both signal diversity and link reliability can be attained in a multiple antenna wireless system by using spatial diversity. Spatial diversity is a pragmatic solution because it does not incur excess time and frequency resources. In most consumer electronic devices, antenna elements spatial distribution is limited by form size thus limited spatial diversity is achieved. PLC can be used as a technique to improve spatial diversity by distributing the antenna elements of a multiple antenna wireless system several wavelengths apart. A serial hybrid channel is more favourable due to the advantage of longer link rage, and it would allow antenna elements of a wireless transceiver to be spatially distributed several wavelengths apart. In a MIMO channel, signal replicas can be received through multiple diversity branches spatially distributed by a powerline channel. The PLC method also allows for varying antenna element spatial distribution depending on the powerline channel transfer characteristics. Assuming sufficient spatial distribution, independent and uncorrelated received signal replicas are then combined using linear diversity combining techniques such as MRC, SC and EGC at the receiver for demodulation. From this point forth, the hybrid channel refers to the serial powerline-wireless hybrid channel. To the best of the author's knowledge, the use of PLC methods in multiple antenna wireless systems to improve the invoked signal diversity has not been attempted before in literature.

CHAPTER 3 PERFORMANCE ANALYSIS OF POWER LINE COMMUNICATION AND DIVERSITY TECHNIQUES

3.1 CHAPTER OVERVIEW

Error rate performance of PLC systems is affected by powerline channel impairments such as multipath signal propagation behaviour and inherent noise interferences. Noise interference in a multipath PLC environment can be considered as a combination of impulsive noise and white background noise. Section 3.2 presents BER analysis of a PLC system using single-carrier and multi-carrier modulation in a multipath PLC environment with impulsive noise and white noise. BPSK and general QAM modulation are used for single-carrier, and OFDM using BPSK and general QAM modulation is used as the multi-carrier technique. Background noise is modelled as AWGN and impulsive noise is modelled using Middleton's Class A noise model. Monte Carlo simulations are performed to produce BER curves of the PLC system for single-carrier and multi-carrier modulation. Section 3.4 presents the use of diversity techniques in multiple antenna wireless systems. Diversity techniques are classified as transmit diversity and receive diversity. Receive diversity is achieved in multiple antenna wireless systems through the use of diversity combining techniques. Analytical BER performance solutions for diversity combining techniques are presented under a Rayleigh fading environment. Transmit diversity in multiple antenna wireless systems is achieved through space-time block coding. Monte Carlo simulations are performed to produce BER curves of receive diversity and transmit diversity techniques. Diversity gain achieved in multiple antenna wireless systems is affected by mutual coupling and signal envelope correlation. Section 3.5 presents an analysis of the effects of both mutual coupling and spatial correlation for a MIMO system under a Rayleigh fading environment. Monte Carlo simulations are performed to produce BER curves to investigate the effects of mutual coupling and signal envelope correlation.

3.2 POWERLINE CHANNEL NOISE INTERFERENCE

Powerline noise interferences are broadly classified into background noise and impulsive noise [11, 31, 39]. Background noise is generally stationary over long periods lasting seconds, minutes and even hours on some occasions, while impulsive noise interferences have RMS amplitudes that vary rapidly over periods of milliseconds or microseconds. Background noise can be conveniently modelled as AWGN since it is observed to satisfy the same statistical properties. The Middleton's Class A noise model is used to model the impulsive noise since it satisfies all the fundamentals of powerline channel noise and it is not limited to modulation or channel type. The model can be used to represent both background and impulsive noise since it generates both Gaussian and impulsive random variables. Impulsive noise is the most detrimental to the performance of PLC systems. To investigate the effects of impulsive noise, the impulsive index parameter of the model will be adjusted to generate more impulsive random variables than Gaussian random variables.

3.2.1 Middleton's Class A noise model

Middleton's Class A noise model refers to impulsive noise with a spectrum that is narrow compared to the receiver bandwidth and includes all pulses that do not produce transients in the receiver front-end [52]. According to the model, the PDF of the noise with amplitude v is given as

$$p(v) = \sum_{k=0}^{\infty} \frac{e^{-A} \cdot A^k}{k!} \cdot \frac{1}{\sqrt{2\pi}\sigma_k} \cdot \exp\left(\frac{-v^2}{2 \cdot {\sigma_k}^2}\right), \tag{3.1}$$

where ${\sigma_k}^2 = P \cdot \frac{(k/A)+\Gamma}{1+\Gamma}$, $P = {\sigma_G}^2 + {\sigma_I}^2$ and $\Gamma = \frac{{\sigma_G}^2}{{\sigma_I}^2}$. k represents the number of impulsive noise samples and P denotes the total noise power of Gaussian and impulsive random variables. ${\sigma_G}^2$ and ${\sigma_I}^2$ represent the Gaussian and impulsive noise powers, respectively. Γ and A represent the Gaussian-to-impulsive noise power ratio (GIR) and the impulsive index, respectively. The impulse index is given as $A = \lambda T_s$, where λ is the impulse rate and T_s is the impulse duration. By increasing A the impulses become low in amplitude and frequent in occurrences, meaning the noise becomes more Gaussian than impulsive. By decreasing A the impulses become high in amplitude and less frequent in occurrences, meaning the noise is more impulsive [53]. The noise closely follows a Poisson process in the case of decreased A. The model assumes that the individual samples are Poisson distributed in time. The noise model in (3.1) is intended to be more impulsive noise representative. As such, it can be assumed that the impulsive noise follows a Poisson process. Noise samples are given as

$$n_k = w_k + b_k g_k, \tag{3.2}$$

where n_k is the total noise samples, w_k represents a white Gaussian background noise sequence with zero mean and variance ${\sigma_G}^2$ and g_k represents a white Gaussian sequence with zero mean and variance ${\sigma_I}^2/A$. Lastly, b_k represents a Poisson distributed sequence whose PDF is characterised by the impulsive index A. In (3.2), the impulsive noise contributes to the overall noise sample according to a Poisson distributed random sequence.

3.3 SINGLE-CARRIER AND MULTI-CARRIER MODULATION BER ANALYSIS

The effect of impulsive noise in wireless systems is different from that in PLC systems. In [54], the effects of impulsive noise on the BER performance of OFDM in wireless systems were studied. The results obtained do not apply to PLC system as the impulsive noise interferences are different. As previously mentioned, powerline channel noise is a combination of background noise and impulsive noise. In order to analyse the BER performance different modulation techniques in powerline channels, background noise is modelled as AGWN with zero mean and variance ${\sigma_G}^2$, and the impulsive noise is given as

$$i_k = b_k g_k, \tag{3.3}$$

where b_k is a Poisson process which represents the arrival of the impulsive noise pulses and g_k is a white Gaussian process with zero mean and variance ${\sigma_I}^2$. Equation 3.3 can be physically interpreted as each transmitted data symbol being corrupted independently with an impulsive noise with probability b_k and random amplitude g_k [54]. Let s_k be the transmitted signal, and then the received signal is expressed as

$$r_k = s_k + n_k, \tag{3.4}$$

where n_k is the noise given by (3.2). The noise PDF can be expressed as

$$p_{n_k} = (1-\psi)G(n_k, 0, {\sigma_w}^2) + \psi G(n_k, 0, {\sigma_w}^2 + {\sigma_i}^2), \tag{3.5}$$

where n_k includes both real and imaginary parts on the noise, ψ represents the probability of occurrence of the impulses, of which is the impulse index A, and $G(x)$ is the Gaussian density function defined as

$$G(x, m_x, {\sigma_x}^2) = \frac{1}{\sigma_x\sqrt{2\pi}} \exp\left(-\frac{(x-m_x)^2}{2{\sigma_x}^2}\right). \tag{3.6}$$

The probability of occurrence of impulsive noise closely follows a Poisson distribution, which means that the arrival of impulsive noise follows the Poisson process with an arrival rate of λ units-per-second. The event of k arrivals in t seconds has the probability distribution

$$p_k(t) = \frac{e^{-\lambda t}(\lambda t)^k}{k!}, \quad k = 0, 1, 2, ... \tag{3.7}$$

Let the average duration of the impulsive noise be donated by T_{niose}, and the duration of the symbol be denoted as T. In the time period T, there can be more than one occurrence of the impulsive noise. Let P_i represent the average occurrence of impulsive noise in time T, and $P_0 = 1 - P_i$ denote the average probability in which only AWGN is present in time T. According to (3.7)

$$\begin{aligned} P_i &= \left[\sum_{k=0}^{\infty} e^{-\lambda T}\frac{(\lambda T)^k}{k!}(kT_{noise})\right] \Big/ T \\ &= \lambda T_{noise}\left[\sum_{k=1}^{\infty} e^{-\lambda T}\frac{(\lambda T)^{k-1}}{(k-1)!}\right] \\ &= \lambda T_{noise}\left[\sum_{k=0}^{\infty} e^{-\lambda T}\frac{(\lambda T)^k}{k!}\right] = \lambda T_{noise}, \end{aligned} \tag{3.8}$$

which results in the impulse index A as the probability of occurrence of impulsive noise.

3.3.1 BER performance of single-carrier in a powerline channel

3.3.1.1 BPSK BER performance

The BER performance of single-carrier BPSK under a combination of impulsive noise and AWGN is expressed as

$$P_b = P_b P_{bi} + P_0 P_{bw} = \lambda T_{noise} P_{bi} + (1 - \lambda T_{noise}) P_{bw}, \tag{3.9}$$

where P_{bi} and P_{bw} are the BER under impulsive and AWGN, respectively. According to the BER formula for BPSK [2, 55], P_{bi} and P_{bw} can be expressed as

$$\begin{aligned} P_{bi} &= Q\left(\sqrt{\frac{2E_b}{N_i + N_0}}\right), & (3.10)\\ P_{bw} &= Q\left(\sqrt{\frac{2E_b}{N_0}}\right), & (3.11) \end{aligned}$$

where E_b is the signal energy-per-bit, N_i and N_0 are the power spectral densities of the impulsive noise and AWGN receptively, and $Q(x)$ is the error function. Substituting (3.10) and (3.11) into (3.9) BER performance of BPSK under powerline channel noise is

$$\begin{aligned} P_{b_{BPSK}} &= \lambda T_{noise} P_{bi} + (1 - \lambda T_{noise}) P_{bw} & (3.12)\\ &= \lambda T_{noise} \cdot Q\left(\sqrt{\frac{2E_b}{N_i + N_0}}\right) + (1 - \lambda T_{noise}) \cdot Q\left(\sqrt{\frac{2E_b}{N_0}}\right). \end{aligned}$$

3.3.1.2 QAM BER performance

For a single-carrier QAM modulation scheme, (3.9) still holds and P_{bi} and P_{bw} still represent the BER under impulsive and AWGN, respectively. P_{bi} and P_{bw} are the BER for QAM under impulsive noise and AWGN expressed as [2, 55]

$$\begin{aligned} P_{bi} &= \frac{4}{k}\left(1 - \frac{1}{\sqrt{M}}\right) Q\left(\sqrt{\frac{3k}{M-1} \cdot \frac{E_b}{N_i + N_0}}\right), & (3.13)\\ P_{bw} &= \frac{4}{k}\left(1 - \frac{1}{\sqrt{M}}\right) Q\left(\sqrt{\frac{3k}{M-1} \cdot \frac{E_b}{N_0}}\right), & (3.14) \end{aligned}$$

where k is the even number of bits-per-symbol, M is the number of symbols which equals to 2^k. E_b, N_i and N_0 remain the signal energy-per-bit, the PSDs of the impulsive noise and of the AWGN, respectively. Substituting (3.13) and (3.14) into (3.9) BER performance of single-carrier QAM under powerline channel noise is expressed as

$$\begin{aligned} P_{b_{QAM}} &= \lambda T_{noise} P_{bi} + \left(1 - \lambda T_{noise}\right) P_{bw} \\ &= \lambda T_{noise} \cdot \frac{4}{k}\left(1 - \frac{1}{\sqrt{M}}\right) Q\left(\sqrt{\frac{3k}{M-1} \cdot \frac{E_b}{N_i + N_0}}\right) \\ &+ \left(1 - \lambda T_{noise}\right) \cdot \frac{4}{k}\left(1 - \frac{1}{\sqrt{M}}\right) Q\left(\sqrt{\frac{3k}{M-1} \cdot \frac{E_b}{N_0}}\right). \end{aligned} \tag{3.15}$$

3.3.2 BER performance of multi-carrier in a powerline channel

OFDM is the most suitable candidate for multi-carrier modulation in powerline channels. OFDM is robust against channel frequency selectivity and the fading effects of the hostile powerline channel. Let s_n denote the transmitted signal, which is an OFDM symbol transmitted through the powerline channel. Let r_k denote the received signal, after front-end filtering and sampling, assuming perfect synchronization and symbol timing, r_k is given by

$$r_k = \frac{1}{\sqrt{N}} \sum_{n=0}^{N-1} s_n e^{\frac{j2\pi nk}{N}} + w_k + i_k, \quad k = 0, 1, 2, ..., N-1, \tag{3.16}$$

where s_n is the transmitted OFDM symbol, either BPSK or QAM modulated, N is the number of carriers in the OFDM symbol, i_k and w_k are the impulsive noise and AWGN components, respectively. The transmitted symbols $\{s_k\}_{k=0}^{N-1}$ are recovered from the received symbols $\{r_k\}_{k=0}^{N-1}$ by performing an N point DFT as

$$R_k = \frac{1}{\sqrt{N}} \sum_{n=0}^{N-1} s_n e^{\frac{j2\pi nk}{N}} + W_k + I_k, \quad k = 0, 1, 2, ..., N-1, \tag{3.17}$$

where W_k is the AWGN after the DFT process. DFT of the impulsive noise I_k is expressed as [54]

$$I_k = \frac{1}{\sqrt{N}} \sum_{n=0}^{N-1} i_n e^{\frac{j2\pi nk}{N}}, \quad k = 0, 1, 2, ..., N-1. \tag{3.18}$$

The effect of the impulsive noise is spread over N data symbols due to the DFT process, which is different from that of single-carrier in which the impulsive noise affects the entire symbol.

The total noise PSD is given as

$$N_n = N_0 + P_i N_i = N_0 + \lambda T_{noise} N_i, \tag{3.19}$$

where N_n is the overall PSD of the noise, which includes AWGN and impulsive noise. Let μ be the ratio of impulsive noise power to AWGN power defined as

$$\mu = \frac{N_i}{N_0}. \tag{3.20}$$

3.3.2.1 BPSK BER performance

BER performance of OFDM using BPSK modulation is expressed as [2, 55]

$$P_b = Q\left(\sqrt{\frac{2E_b}{\eta}}\right), \tag{3.21}$$

where η is the noise power. In a powerline channel, substituting (3.20) and (3.19) into (3.21), BER performance for OFDM using BPSK under powerline channel noise is given by

$$\begin{aligned} P_{b_{BPSK}} &= Q\left(\sqrt{\frac{2E_b}{N_n}}\right) \\ &= Q\left(\sqrt{\frac{2\left(E_b/N_0\right)}{1+\mu\lambda T_{noise} N_i}}\right). \end{aligned} \tag{3.22}$$

3.3.2.2 QAM BER performance

The BER performance of OFDM using QAM modulation is expressed as [2, 55]

$$P_{b_{QAM}} = \frac{4}{k}\left(1-\frac{1}{\sqrt{M}}\right) Q\left(\sqrt{\frac{3k}{M-1}\cdot\frac{E_b}{\eta}}\right), \tag{3.23}$$

where k is the even number of bits-per-symbol, M is the number of symbols which equals to 2^k and η is the noise power. Under powerline channel noise, substituting (3.20) and (3.19) into (3.23), BER performance for OFDM using QAM modulation is given by

$$\begin{aligned} P_{b_{QAM}} &= \frac{4}{k}\left(1-\frac{1}{\sqrt{M}}\right)Q\left(\sqrt{\frac{3k}{M-1}\cdot\frac{E_b}{N_n}}\right) \qquad (3.24)\\ &= \frac{4}{k}\left(1-\frac{1}{\sqrt{M}}\right)Q\left(\sqrt{\frac{3k}{M-1}\cdot\frac{1}{1+\mu\lambda T_{noise}}\cdot\frac{E_b}{N_0}}\right). \end{aligned}$$

When considering the effect of impulsive noise on BER performance of an OFDM system, the signal-to-noise ratio $\frac{E_b}{N_0}$ should be replaced with $\frac{E_b}{N_n}$.

3.3.3 Simulations

Background noise was modelled as AWGN with zero mean and unit variance, and impulsive noise was modelled as Middleton's Class A noise model. In [31], impulsive noise was measured and characterised into three scenarios, namely "heavily disturbed" scenario, "medium disturbed" scenario and "weakly disturbed" scenario. The three scenarios are given in Table. 3.1. The noise scenarios are characterised by their impulse arrival rate (λ) and the impulsive width T_{noise}. The parameter A is a product of λ and T_{noise}. A represents the probability of occurrence for the respective noise scenarios. Middleton's Class A impulsive noise amplitude responses for heavily disturbed, medium disturbed and weakly disturbed powerline channels are given by Fig. 3.1, Fig. 3.2 and Fig. 3.3 respectively.

Table 3.1. Parameters of impulsive noise scenarios [31].

Impulsive noise scenario	λ	T_{noise}	A
I: Heavily disturbed	1/0.0196 s^{-1}	0.0641 ms	0.00327
II: Medium disturbed	1/0.9600 s^{-1}	0.0607 ms	0.000632
III: Weakly disturbed	1/8.1967 s^{-1}	0.1107 ms	0.0000135

For a heavily disturbed powerline channel, Fig. 3.1 shows that there is a high density of impulses, this is due to a high λ given by 1/0.0196 s^{-1} = 51 Hz, which translates into a higher probability of occurrence of impulsive noise A. A high value of A also means low amplitude impulses. However, due to the high density of impulses, this scenario causes more transmission errors and adversely degrades the powerline channel BER performance. A powerline channel with the medium disturbed scenario is shown in Fig. 3.2, it has a lower density of impulses

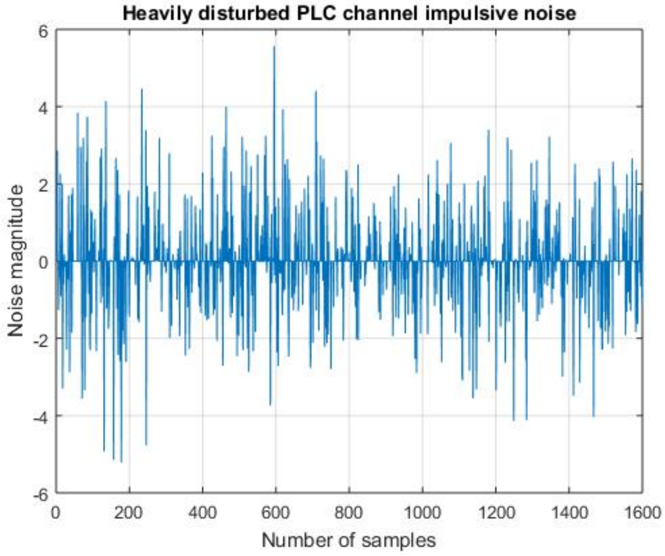

Figure 3.1. Middleton’s Class A heavily disturbed impulsive noise.

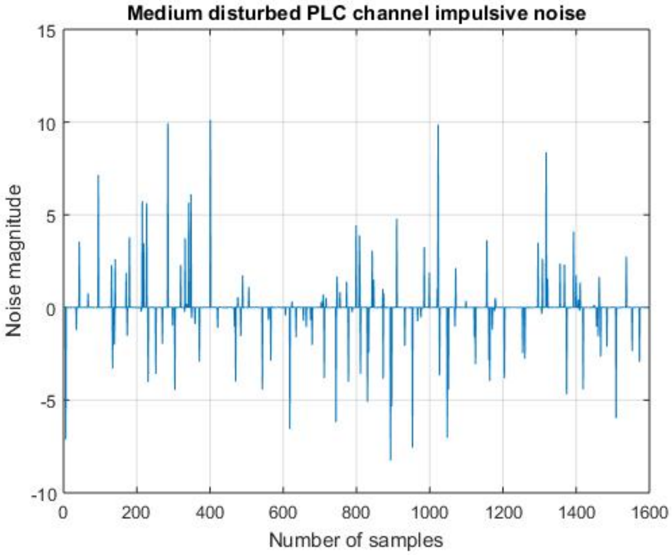

Figure 3.2. Middleton’s Class A medium disturbed impulsive noise.

due to a lower value of λ. A lower value of A for Fig. 3.2 translates into higher impulse amplitudes. This scenario causes fewer burst errors. A powerline channel with the weakly disturbed scenario has the lowest impulse rate and lowest probability of occurrence. Fig. 3.3 shows that in this scenario, there is a minimal number of impulses, sometimes even one within hours, but with the highest impulse amplitude. This scenario causes a few or one burst error in the transmitted information.

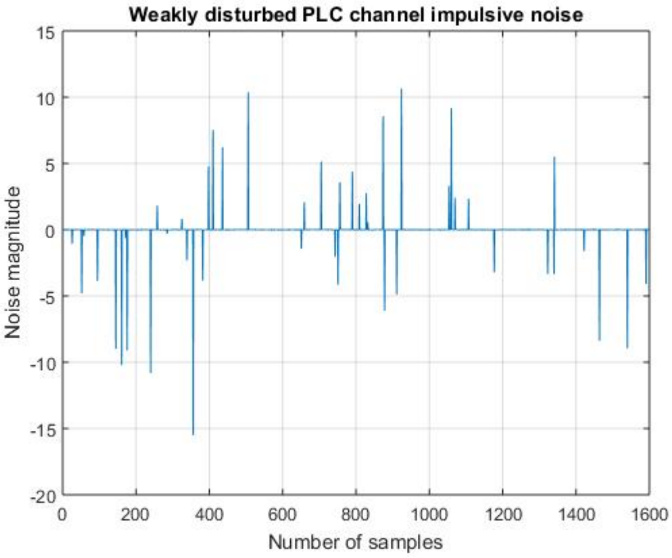

Figure 3.3. Middleton's Class A weakly disturbed impulsive noise.

Monte Carlo simulations were performed for single-carrier and OFDM multi-carrier modulation in a multipath powerline channel under the three noise scenarios. Fig. 3.5 shows the simulation model for single-carrier modulation and Fig. 3.4 shows the simulation model for OFDM. The parameters used for the simulations are summarised in Table. 3.2. The four path Zimmerman-Dostert powerline channel model was used in the simulations [21]. The noise source is the different noise scenarios described previously using Middleton's Class A noise model.

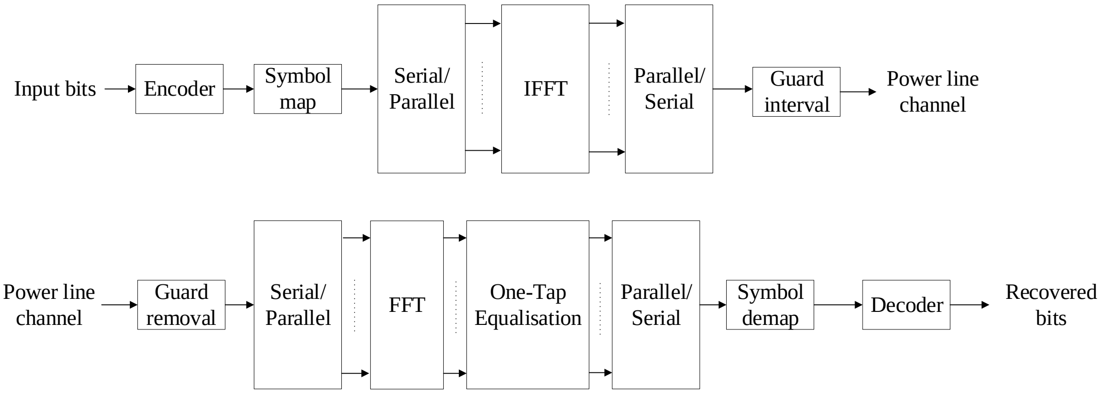

Figure 3.4. OFDM multi-carrier modulation model for power line channel.

The Γ parameter was set to 0.01, meaning the impulsive noise is one hundred times as large as background noise. Under heavily disturbed impulsive noise conditions, a high error rate is experienced by both single-carrier and OFDM. High error rates are caused by the high density of impulses in the heavily disturbed scenario, and it causes continuous burst errors

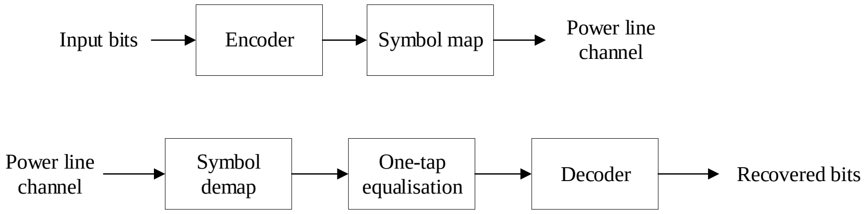

Figure 3.5. Single-carrier modulation model for power line channel.

Table 3.2. Simulation parameters

Channel type	Four path Zimmerman-Dostert powerline model
Noise type	Middleton's Class A noise model
$\frac{E_b}{N_0}$	[0,1,2,...,35] dB
OFDM	
FFT size	64
Modulation	BPSK/QPSK/16-QAM/64-QAM
Encoding	1/2 Convolutional encoder
Decoding	Viterbi decoder
Guard interval size	16
Equalisation	Zero-forcing
Single-carrier	
Modulation	BPSK/QPSK/16-QAM/64-QAM
Encoding	1/2 Convolutional encoder
Decoding	Viterbi decoder
Equalisation	Zero-forcing

in single-carrier systems. In OFDM, it causes burst errors in numerous OFDM symbols. These conditions are highly unfavourable for data transfer and higher error rates could be experienced in practical systems. For medium and weakly disturbed noise conditions, the lower density of impulses causes isolated bursts errors in single-carrier and only a few OFDM symbols experience burst errors. Therefore the BER performance is improved for the same signal power.

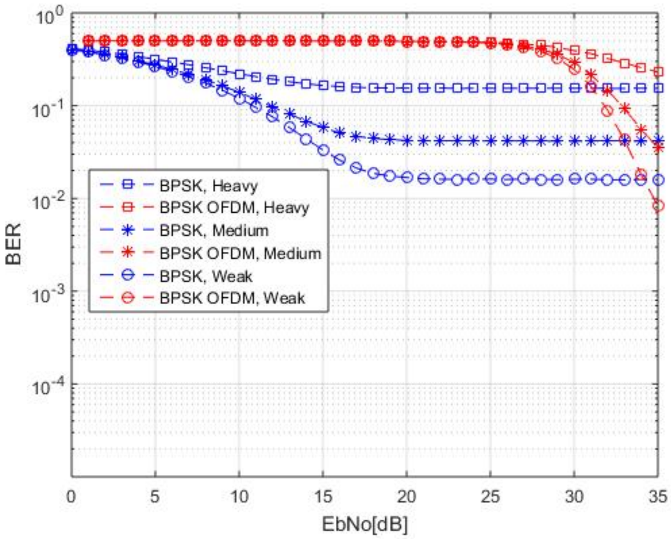

Figure 3.6. Simulated single-carrier and BPSK-OFDM under three impulsive noise scenarios.

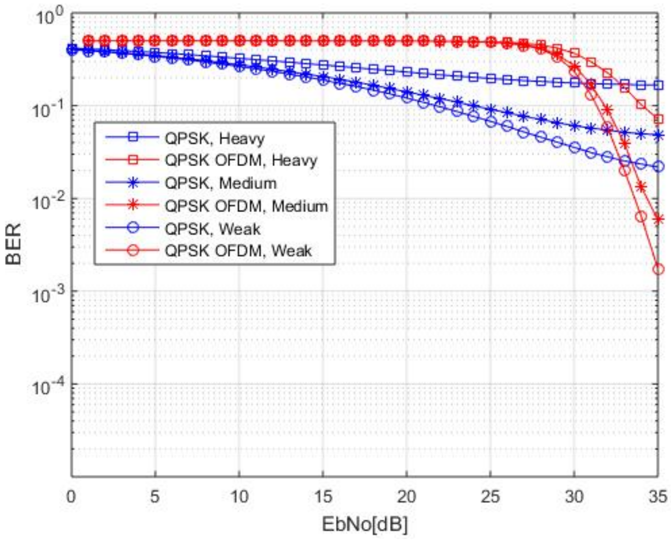

Figure 3.7. Simulated single-carrier and QPSK-OFDM under three impulsive noise scenarios.

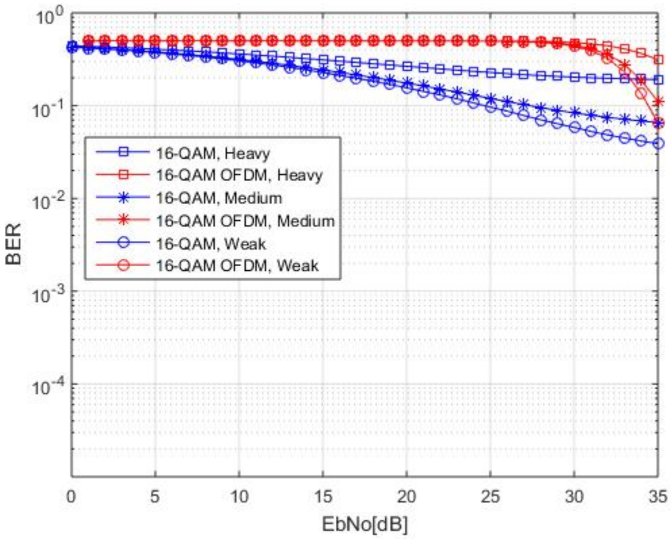

Figure 3.8. Simulated single-carrier and 16-QAM OFDM under three impulsive noise scenarios.

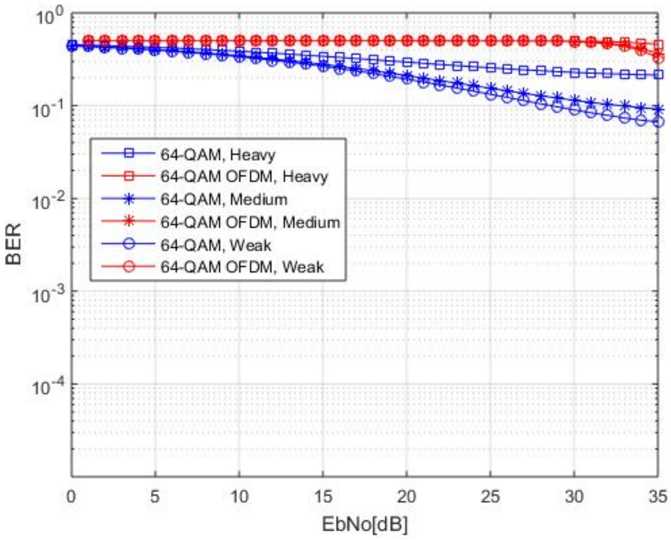

Figure 3.9. Simulated single-carrier and 64-QAM OFDM under three impulsive noise scenarios.

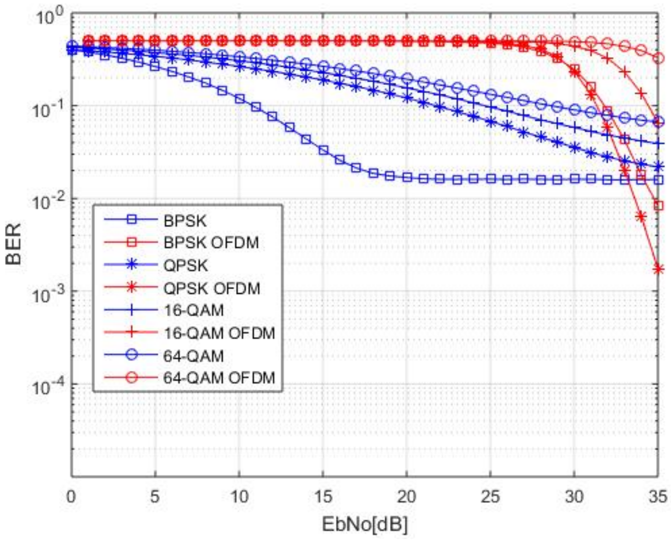

Figure 3.10. Simulated single-carrier and OFDM systems under weak impulsive noise.

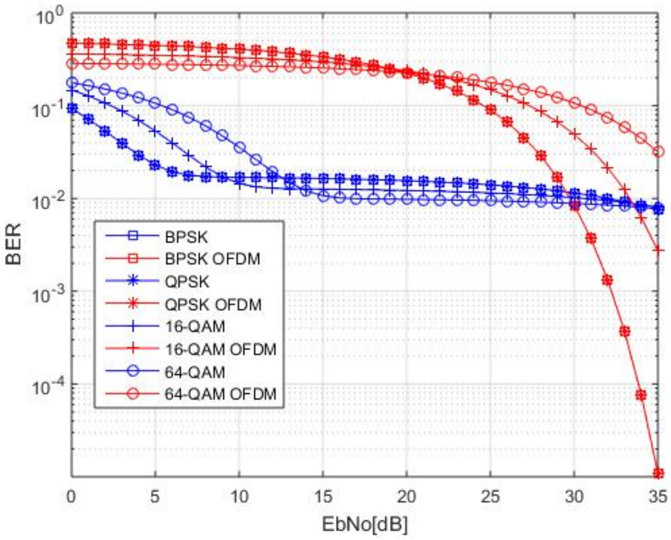

Figure 3.11. Analytical single-carrier and OFDM systems under weak impulsive noise.

In Fig. 3.6, an error floor experienced by the single-carrier system is clearly shown, which is also present in Fig. 3.7 to Fig. 3.9. This is because impulsive noise leads to continuous burst errors in a single-carrier system, and increasing the signal power will not improve the performance effectively. In the OFDM system, the effect of impulsive noise is spread over N symbols due to the DFT operation described in (3.18). BER performance of OFDM can be effectively improved with an increase in the signal power E_b/N_0. From this point of view, OFDM outperforms single-carrier in a powerline channel with impulsive noise. BER curves for 16-QAM and 64-QAM show a higher error rate because the probability of erroneous symbol detection increases with the mapping constellation size. Under weak impulsive noise conditions, an improvement in the error floor is observed for single-carrier modulation with an increase in E_b/N_0.

Analytical BER solutions for single-carrier and OFDM under weak impulsive noise conditions are plotted in Fig. 3.11. Compared with the Monte Carlo BER simulations for single-carrier under the same weak impulsive noise conditions in Fig. 3.10, theoretical BER outperforms the simulations in the high E_b/N_0 region. However, an error flow is reached in lower E_b/N_0 region compared to the simulations. In the high E_b/N_0 region, OFDM attains error rate of 10^{-3} for $E_b/N_0 = 32\ dB$, which is $3\ dB$ less compared to OFDM simulation at $BER = 10^{-3}$. The fallback of Middleton's Class A impulsive noise model lies in its inability to capture periodic nature on the impulsive noise in PLC channels. The resultant BER can be improved by making use of other models such as the Bernoulli-Gaussian and Symmetric alpha-stable models. Given some differences in model parameters and type of model, it is worth noting that the obtained simulation results are consistent with other works in literature investigating multi-carrier systems in a powerline channel environment with impulsive noise [11, 33, 56, 57].

3.4 TRANSMIT AND RECEIVE DIVERSITY

3.4.1 Receive diversity

The Rayleigh distribution is commonly used to model the fading envelope statistics imparted on a radio signal transmitted in an environment where there is no line-of-sight (LOS) component between the transmitter and receiver. These conditions are experienced in urban areas and cities where there are natural and human-made obstructions. An ideal model would be a spatial channel model that takes into account the relative positions of antenna elements and their spatial correlation. The study in [9] investigates practical spatial scattering and correlation between diversity branches for diversity combining techniques in a SIMO wireless system. The results show that the developed spatial model falls short of the ideal Rayleigh fading model unless a large number of receive antenna elements are used. This makes the model not useful for practical systems. In [58], Turkmani *et al.* investigate the effect of spatial correlation ρ and power imbalance D_M for diversity combining techniques for a SIMO wireless system. The results of the study show that a practical correlation coefficient of $\rho < 0.7$ is sufficient to assume independence amongst diversity branches and assume independent signal propagation paths. Therefore the Rayleigh fading can still be used without loss of generality. The Rayleigh distribution PDF is given by as

$$p(\alpha) = \frac{2\alpha}{\Omega} \exp\left(-\frac{\alpha^2}{\Omega}\right), \tag{3.25}$$

where α is a random variable representing the amplitude of the signal and $\mathit{\Omega}$ denotes the power of the random variable. The instantaneous SNR, γ, defined as the ratio of the energy per-bit E_b to the spectral noise power N_0 is given by the distribution function

$$p(\gamma) = \frac{1}{E_b/N_0} \exp\left(-\frac{\gamma}{E_b/N_0}\right), \tag{3.26}$$

where the noise is considered to be AWGN with zero mean and variance $N_0/2$. The probability of error for a given combining scheme is generally expressed by

$$P_e = \int\limits_0^\infty \frac{1}{2}\mathrm{erfc}\left(\sqrt{\gamma}\right) \cdot p\left(\gamma\right)\ d\gamma. \tag{3.27}$$

Assuming a slow fading channel, that is the symbol time is smaller than the maximum channel dispersion time, the equivalent received signal r_i at the i^{th} diversity branch, that is the N^{th} antenna element, can be expressed as

$$r_i\left(t\right) = A_i e^{j\theta_i} \cdot s\left(t\right) + n_i\left(t\right), \quad i = 1, 2, 3, ..., N-1, \tag{3.28}$$

where $s(t)$ is the transmitted signal, n_i is the AWGN and $A_i e^{j\theta_i}$ represents the fading effects, including attenuation and phase-shifting. In multiple antenna wireless systems N replicas of the same information carrying signal are received at N antenna elements such that $r = [r_1(t), r_2(t), ..., r_{N-1}(t)]$.

3.4.1.1 Selection combining

Selection combining is the simplest combining method in a SIMO or MIMO system whereby the diversity branch with the most favourable SNR is selected for demodulation. The combined signal $y(t)$ and the output SNR Γ are expressed by (3.29) and (3.30), respectively.

$$y\left(t\right)=Ae^{j\theta_i}\cdot s\left(t\right)+n_i\left(t\right),\quad \text{with } \mathrm{A}=\max\left[\mathrm{A}_0,\mathrm{A}_1,\mathrm{A}_2,...,\mathrm{A}_{\mathrm{M}-1}\right]. \tag{3.29}$$

$$\Gamma=A^2\frac{E_b}{N_0}=\max\left[\Gamma_1,\Gamma_2,\Gamma_3,...,\Gamma_{M-1}\right]. \tag{3.30}$$

In order to analyse the probability of bit error, the probability of failure $p(\gamma)$ for a diversity branch needs to be obtained [7]. The probability of failure refers to the probability that E_b/N_0 drops below a certain threshold γ_s. For N receive antenna elements the probability of failure for anyone one of the diversity branches is given by

$$p\left(\gamma\right)=\frac{dP_{out}}{d\gamma}=\frac{N}{E_b/N_0}\cdot e^{\frac{-\gamma}{E_b/N_0}\left[1-e^{\frac{-\gamma}{E_b/N_0}}\right]^{N-1}}. \tag{3.31}$$

BER performance of BPSK in an AWGN environment is defined as [2,55]

$$P_b=\frac{1}{2}erfc\left(\sqrt{\frac{E_b}{N_0}}\right), \tag{3.32}$$

where the effective E_b/N_0 is denoted by γ. Substituting (3.31) into (3.27), the total BER is given as the integral of the conditional BER over all possible values of γ, which is expressed as

$$P_e=\int_0^\infty\frac{1}{2}erfc\left(\sqrt{\gamma}\right)\cdot p\left(\gamma\right)d\gamma=\int_0^\infty\frac{1}{2}erfc\left(\sqrt{\gamma}\right)\cdot\frac{N}{E_b/N_0}\cdot e^{\frac{-\gamma_i}{E_b/N_0}\left[1-e^{\frac{-\gamma_i}{E_b/N_0}}\right]^{N-1}}d\gamma, \tag{3.33}$$

which then reduces to

$$P_e=\frac{1}{2}\sum_{k=0}^{N-1}\left(-1\right)^k\left(\begin{array}{c}N\\k\end{array}\right)\left(1+\frac{k}{E_b/N_0}\right)^{1/2}, \tag{3.34}$$

which is Equation 11.24 in Section 11.3.2 [3]. With SC, the effective SNR is not improved linearly with the increase in the number of receive antenna elements N, and the effective SNR is actually is deteriorated with the increase in N [7].

3.4.1.2 Maximal ratio combining

Maximal ratio combining (MRC) is an optimal linear signal combining method offering the best results in mitigating fading effects. In MRC, all the signals received at each diversity branch are co-phased to ensure coherent combination and multiplied by weighting factors w_i $(i = 1, 2, 3, ..., N)$ before combining. The weighting factors are derived from the estimation of the instantaneous SNR at each diversity branch. The diversity branch with the most favourable SNR is taken with a greater contribution, which is a larger weighting factor. This ensures that the received signal with more power has a greater contribution to the combined signal [1, 7]. Estimation of instantaneous SNR and correcting phase-offsets increases the complexity of MRC and make it expensive for practical implementations.

The combined signal $y(t)$ is given by (3.35) where the weighting factors are chosen such that they are channel gain conjugates.

$$y\left(t\right) = \sum_{i=0}^{N-1} w_i \cdot r_i = \left(\sum_{i=0}^{N-1} {A_i}^2\right) \cdot s\left(t\right) + \sum_{i=0}^{N-1} A_i e^{-j\theta_i} \cdot n\left(t\right). \tag{3.35}$$

The combined signal output SNR is given as

$$\Gamma = \frac{\sum\limits_{i=0}^{N-1} {A_i}^2 \cdot E_b}{N_0} = \sum_{i=0}^{N-1} \Gamma_i. \tag{3.36}$$

The probability of failure for any of the N diversity branches using MRC is given by

$$p\left(\gamma\right) = \frac{1}{\left(N-1\right)!\left(E_b/N_0\right)} \cdot \gamma^{N-1} \cdot e^{\frac{\gamma}{\left(E_b/N_0\right)}}. \tag{3.37}$$

In an AWGN environment, BER performance of BPSK is defined by (3.32), denoting E_b/N_0 as the effective SNR γ and substituting (3.37) into (3.27), the total BER is given as the integral of (3.37) over all possible values of γ, which is given as

$$\begin{aligned} P_e &= \int_0^\infty \frac{1}{2} erfc\left(\sqrt{\gamma}\right) \cdot p\left(\gamma\right)\ d\gamma \qquad (3.38) \\ &= \int_0^\infty \frac{1}{2} erfc\left(\sqrt{\gamma}\right) \cdot \frac{1}{\left(N-1\right)!\left(E_b/N_0\right)} \cdot \gamma^{N-1} \cdot e^{\frac{-\gamma}{\left(E_b/N_0\right)}}\ d\gamma, \end{aligned}$$

which reduces to

$$P_e = p^N \sum_{k=0}^{N-1} \begin{pmatrix} N-1+k \\ k \end{pmatrix} \cdot (1-p)^k, \tag{3.39}$$

where

$$p = \frac{1}{2} + \frac{1}{2}\left(1 + \frac{1}{E_b/N_0}\right)^{-\frac{1}{2}}. \tag{3.40}$$

3.4.1.3 Equal gain combining

Equal gain combining compensates for phase-offsets by also performing co-phasing of the diversity branches, but the same factor weights the signals before linear combination. Unlike MRC, estimation of instantaneous SNR at diversity branches is not required, the weighting factor is usually simplified to unity which makes EGC simpler and cheaper to implement in practical systems. A slight deterioration in BER performance is experienced in EGC due to the non-optimal contribution of signals with favourable SNRs to the combined signal [3, 7].

The combined signal $y(t)$ after co-phasing and equal weighting is given by

$$y\left(t\right) = \sum_{i=0}^{N-1} e^{-j\theta_i} \cdot r_i = \left(\sum_{i=0}^{N-1} A_i\right) \cdot s\left(t\right) + \sum_{i=0}^{N-1} e^{-j\theta_i} \cdot n\left(t\right).$$

The combined signal output SNR from N diversity branches is given by

$$\gamma = \frac{E_b}{N_0} \cdot \frac{1}{N}\left(N \cdot (N-1) \cdot \sqrt{\frac{\pi}{4}}\right) = \frac{E_b}{N_0}\left(1 + (N-1) \cdot \sqrt{\frac{\pi}{4}}\right). \tag{3.41}$$

To date, there is no closed-form solution for the BER performance of EGC for a general number of N diversity branches under Rayleigh fading conditions. There are two difficulties owing to this. Firstly, there is a lack of the PDF solution of $p(\gamma)$ for EGC, which is the probability of failure of diversity branches. Secondly, the classical $Q(\cdot)$ function argument appears on the lower limit of the integral, which is undesirable when trying to perform the averaging as expressed by (3.27) [1]. In [59], Zhang finds the closed-form solutions for EGC under Rayleigh fading conditions for $N = 2$ and $N = 3$ based on the characteristic function method, the detailed derivations are given in [59] and references there within. The solutions for $N = 2$ and $N = 3$ are given by (3.42) and (3.43), respectively, where γ is the effective SNR and ${}_2F_1$ is a hypergeometric function.

$$P_e = \frac{1}{2}\left[1 - \frac{\sqrt{\gamma\left(\gamma+2\right)}}{\gamma+1}\right], \; N = 2. \tag{3.42}$$

$$P_e = \frac{1}{2} + \frac{1}{2}\sqrt{\frac{\gamma(2\gamma+3)^2}{3(\gamma+1)^3}}\cdot {}_2F_1\left(-\frac{1}{2};\frac{1}{2};\frac{1}{2};\frac{\gamma^2}{(3\gamma+3)^2}\right) + \frac{\pi}{4}\sqrt{\frac{\gamma^3}{27(\gamma+1)^3}},\ N=3. \tag{3.43}$$

3.4.2 Transmit diversity

The highest degree of diversity can be achieved in MIMO wireless systems due to the applicability of both transmit diversity and receive diversity. Significant system performance improvements are achieved through both diversity gain and array gain. In a MIMO system, the same information-carrying signal is transmitted from multiple antenna elements, and each antenna element receives each signal through different propagation paths. Space-time block codes (STBC) are used in MIMO wireless systems to achieve diversity by introducing redundancy in both time and space dimensions. MIMO systems generally use the Alamouti transmit diversity scheme. The Alamouti scheme is an STBC described in a simple block structure and is an optimised STC for two transmit antenna elements and an arbitrary number of N receive antenna elements [60].

Let the code matrix be denoted by s. Two signals are transmitted from two branches simultaneously at a given symbol period T. At time t, symbols s_1 and s_2 are transmitted simultaneously from the first and second antenna element, respectively. Then after a time period of T, at time $t+T$, symbols $-s_2^*$ and s_1^* are transmitted from the first and second antenna element, respectively. * is the complex conjugate operation. The total energy budget is denoted by E_s, and each antenna element has a transmission power of $\frac{E_s}{2}$. The received signal matrix, channel matrix, symbol matrix with encoded symbols defined previously and the AWGN matrix are given as

$$\begin{bmatrix} r_{11} & r_{12} \\ r_{21} & r_{22} \end{bmatrix} = \begin{bmatrix} h_{11} & h_{12} \\ h_{21} & h_{22} \end{bmatrix} \cdot \begin{bmatrix} s_1 & -{s_2}^* \\ s_2 & {s_1}^* \end{bmatrix} + \begin{bmatrix} n_{11} & n_{12} \\ n_{21} & n_{22} \end{bmatrix}. \tag{3.44}$$

At time instant t the receive antenna elements R_{X1} and R_{X2} receive the signals

$$r_{11} = h_{11}\cdot s_1 + h_{12}\cdot s_2 + n_{11}, \tag{3.45}$$

$$r_{12} = h_{21}\cdot s_1 + h_{22}\cdot s_2 + n_{12}. \tag{3.46}$$

At time instant $t+T$ the receive antenna elements R_{X1} and R_{X2} receive the signals

$$r_{21} = h_{11} \cdot (-s_2{}^*) + h_{12} \cdot s_1{}^* + n_{21}, \tag{3.47}$$

$$r_{22} = h_{21} \cdot (-s_2{}^*) + h_{22} \cdot s_1{}^* + n_{22}. \tag{3.48}$$

At the decoder, the arrangement of the transmitted symbols s_1 and s_2 allows for maximum-likelihood decoding to be performed individually on each received symbol independent of other received symbols. This highlights the fact that the symbols are orthogonal to each other. Estimates of s_1 and s_2 are obtained by removing effects of the channel from the received signals, which is weighting the received signals by complex conjugates of the channel. An estimate of $\widetilde{s_1}$ at the receiver is obtained by (3.49). Channel effects are removed by multiplying with the complex conjugates of the received signals at the receiver.

$$\begin{aligned}
\widetilde{s_1} &= h_{11}{}^* \cdot r_{11} + h_{12} \cdot r_{12}{}^* + h_{21}{}^* \cdot r_{21} + h_{22} \cdot r_{22}{}^* \\
&= s_1 \cdot (h_{11}{}^* \cdot h_{11} + h_{12} \cdot h_{12}{}^* + h_{21}{}^* \cdot h_{21} + h_{22} \cdot h_{22}{}^*) \\
&+ h_{11}{}^* \cdot n_{11} + h_{12} \cdot n_{12} + h_{21}{}^* \cdot n_{21} + h_{22} \cdot n_{22} \\
&= s_1 \cdot \left(|h_{11}|^2 + |h_{12}|^2 + |h_{21}|^2 + |h_{22}|^2\right) \\
&+ h_{11}{}^* \cdot n_{11} + h_{12} \cdot n_{12} + h_{21}{}^* \cdot n_{21} + h_{22} \cdot n_{22}.
\end{aligned} \tag{3.49}$$

Similarly, the estimate $\widetilde{s_2}$ is obtained as described by (3.50).

$$\begin{aligned}
\widetilde{s_2} &= h_{12}{}^* \cdot r_{11} - h_{11} \cdot r_{12}{}^* + h_{22}{}^* \cdot r_{21} - h_{21} \cdot r_{22}{}^* \\
&= s_2 \cdot (h_{11}{}^* \cdot h_{11} + h_{12} \cdot h_{12}{}^* + h_{21}{}^* \cdot h_{21} + h_{22} \cdot h_{22}{}^*) \\
&+ h_{12}{}^* \cdot n_{11} - h_{11} \cdot n_{12} + h_{22}{}^* \cdot n_{21} - h_{21} \cdot n_{22} \\
&= s_2 \cdot \left(|h_{11}|^2 + |h_{12}|^2 + |h_{21}|^2 + |h_{22}|^2\right) \\
&+ h_{12}{}^* \cdot n_{11} - h_{11} \cdot n_{12} + h_{22}{}^* \cdot n_{21} - h_{21} \cdot n_{22}.
\end{aligned} \tag{3.50}$$

The remarkable simple arrangement of the transmitted data to introduce redundancy in time and space, and the simple linear processing of the received data ensures that diversity of order-2 is achieved, and no additional bandwidth is consumed. The Alamouti code is the only STBC that achieves a coding rate of unity. STC was generalised by Tarokh *et al.* and they derived metrics to define properties a good codes and limitations STCs. This led to the development of space-time trellis codes (STTC) in efforts to meet the criteria for good codes and achieve good coding gains. These codes, however, achieve higher data rates and coding gain at the expense of increased complexity. Based on the criteria outlined by Tarokh *et al.*, the Alamouti code is the only STBC that can be considered a good code. The pitfall of the Alamouti scheme is that half of the transmit power $\frac{E_s}{2}$ is used at each antenna element. Therefore, there is a 3 dB penalty on the Alamouti scheme compared to a similar two receive antenna elements scheme, such as a 1×2 SIMO system using MRC.

3.4.3 Simulations

Monte Carlo simulations were performed to investigate the BER performance of diversity techniques. Parameters used for both transmit diversity and receive diversity methods are summarised in Table. 3.3. A Rayleigh fading channel was used in the simulations, and the noise was considered to be AWGN.

The BER performance of the SC is shown in Fig. 3.12. SC does not need to be coherent, therefore it is observed to offer the worst BER performance but offers the fastest processing time. Wireless agents such as mobile units and wireless sensors cannot employ coherent combining techniques due to power and processing limitations, as such, they are installed with SC methods to address signal detection at the cost of error rate performance [3, 42]. Fig. 3.13 shows that MRC offers optimal output SNR performance over SC and EGC, however, with the drawback of slow processing time. These processing needs cannot be met in mobile agents. Therefore MRC is more suitable for stationary receivers in indoor environments. BER performance of EGC is given by Fig. 3.14. EGC offers in between MRC and SC. It is superior to SC because signals are combined coherently, but it is still inferior to MRC because signals are weighted equally and not proportionally to their instantaneous SNR. Turkamani *et al.* [58] conducted a study investigating the impact of signal envelope correlation and power imbalance on BER performance of MRC, SC and EGC in Rayleigh fading conditions. The results show that under significant correlation and power imbalance, SC begins to outperform EGC and closely follows MRC, this owing to its less processing time requirements of SC in practical systems.

The BER performance of the Alamouti scheme is shown in Fig. 3.15. The performance is

Table 3.3. Simulation parameters

Channel type	Rayleigh fading channel
Noise type	Additive White Gaussian Noise
$\frac{E_b}{N_0}$	[0,1,2,...,35] dB
Receive diversity	
Modulation	BPSK
Transmitters	1
Receivers	2
Combining	Selection combining Maximal ratio combining Equal Gain combining
Equalisation	Zero-forcing
Demodulation	Hard decision decoding
Transmit diversity	
Encoder	Alamouti STBC
Modulation	BPSK
Transmitters	2
Receivers	2
Equalisation	Zero-forcing
Demodulation	Hard decision decoding

compared with that of the optimal MRC scheme. BER performance curve for 1 × 2 MRC achieves the same diversity order as that of 2 × 1 Alamouti. However, a 3 dB penalty is incurred in the Alamouti BER curve due to power constraints, that means the Alamouti scheme radiates half the power from each antenna element that MRC only radiates one antenna element. If each antenna element in the Alamouti scheme were to radiate the same power as the MRC single antenna element, the performance curve of the two schemes would be identical. The Alamouti scheme is an orthogonal code for two transmit antenna elements, and an arbitrary N receive antenna elements, it extracts full diversity gain without consuming excess frequency or time resources. BER performance for the general case of a 2 × 2 MIMO system using the Alamouti scheme is shown in Fig. 3.15. Fig. 3.15 shows an increase in slope

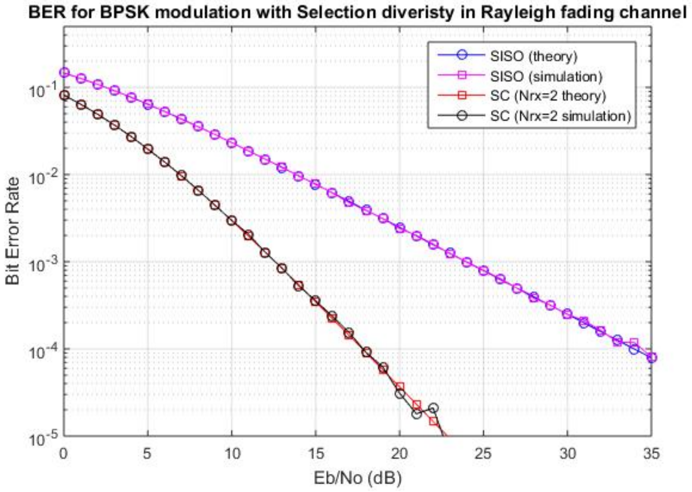

Figure 3.12. Selection combining in Rayleigh fading channel.

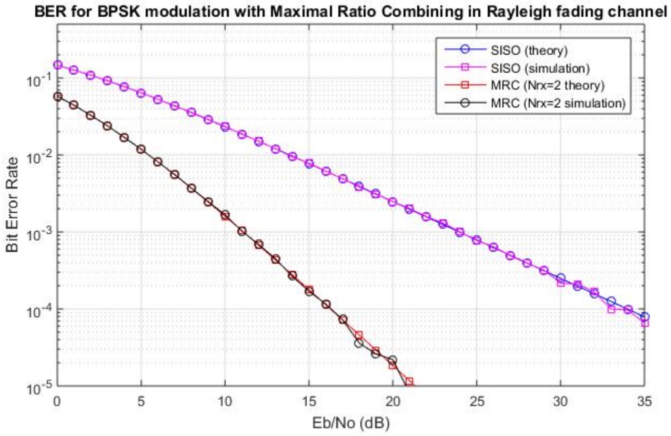

Figure 3.13. Maximal ratio combining in Rayleigh fading channel.

due to an increase in diversity order and a shift to the left, meaning it attains the same BER level for lesser E_b/N_0, due to channel coding gain. In order to achieve the same diversity order as the Alamouti scheme with arbitrary N receive antenna elements, the MRC optimal combiner requires $2N$ receive antenna elements [3, 60].

3.5 SPATIAL CORRELATION AND MUTUAL COUPLING

3.5.1 Effects of spatial correlation

A common assumption often made in MIMO wireless systems that the signal propagation paths between different transmit and receive antenna elements are independent and identically distributed [61]. However, in practice, MIMO channel paths are correlated in the spatial

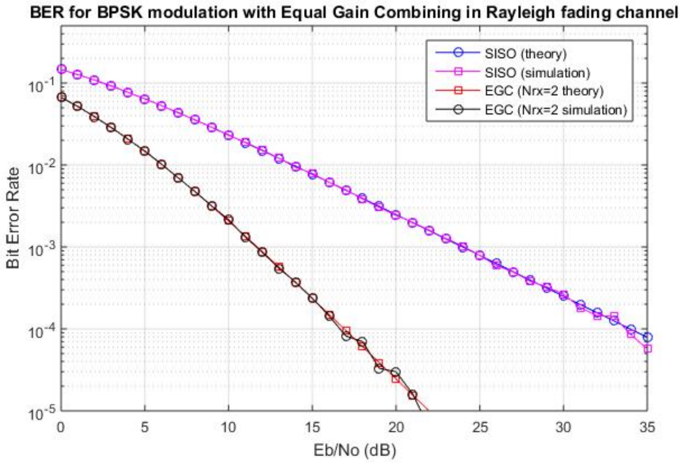

Figure 3.14. Equal gain combining in Rayleigh fading channel.

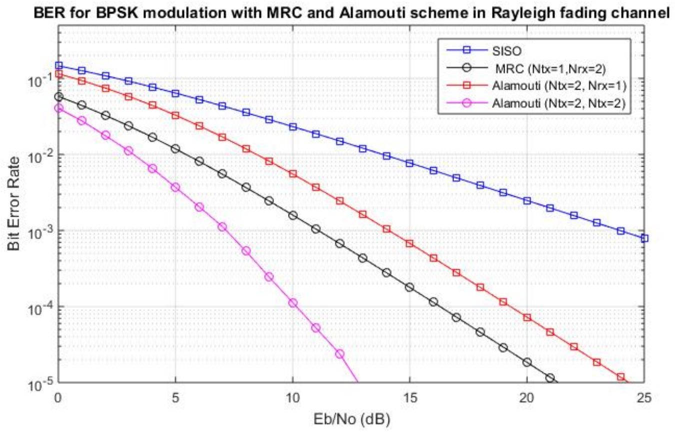

Figure 3.15. MRC and Alamouti in Rayleigh fading channel.

domain [62,63]. Spatial correlation can be modelled in the channel matrix as

$$\mathbf{H} = [\mathbf{R}_{rx}]^{1/2}\mathbf{H}_{iid}\left([\mathbf{R}_{tx}]^{1/2}\right)^{T}, \tag{3.51}$$

where $\mathbf{R}_{tx}$ and $\mathbf{R}_{rx}$ denote the transmit and receive correlation matrices, respectively. The channel matrix generated using zero-mean complex Gaussian variables is denoted by $\mathbf{H}_{iid}$ and $\mathbf{H}$ denotes the correlated channel matrix. Spatial correlation depends on the multipath propagation environment and the proximity of antenna elements. The complex-valued correlation coefficients are derived from the angle of departure (AOD) and angle of arrival (AOA) [64,65]. Multipath signals from the transmitter tend to depart in a range of angular directions rather than a single angle, and this is referred to as AOD. The same phenomenon applies to the receiver, and the signal arrives in a range of angular directions, this describes the AOA. Received signal power gain at the receiver at an AOA of θ is denoted by $\sqrt{G_i(\theta)}$. The received signal covariance matrix is expressed as

$$R_r = \begin{bmatrix} P_1 & E_{t,\theta}\left(r_1(t,\theta)\, {r_2}^*(t,\theta)\right) \\ E_{t,\theta}\left({r_1}^*(t,\theta)\, r_2(t,\theta)\right) & P_2 \end{bmatrix}, \tag{3.52}$$

where $E_{t,\theta}$ denotes the expected value of the received signal $r(t,\theta)$ taken over all t and AOA θ. P_1 and P_1 denote the received signal powers, respectively. Coefficients of spatial correlation between two receive antenna elements are given as

$$\rho_{1,2} = \frac{E_{t,\theta}\left[r_1(t,\theta)\, {r_2}^*(t,\theta)\right] - E_{t,\theta}\left[r_1(t,\theta)\right] E_{t,\theta}\left[{r_2}^*(t,\theta)\right]}{\sqrt{P_1 P_2}}.. \tag{3.53}$$

The covariance matrix can then be simplified to

$$R_r = \sqrt{P_1 P_2} \begin{bmatrix} 1 & \rho_{1,2} \\ {\rho^*}_{1,2} & 1 \end{bmatrix}. \tag{3.54}$$

3.5.2 Effects of spatial correlation and mutual coupling

Mutual coupling in antenna elements is caused by the interaction of the EM waves received at different antenna elements. Studies on mutual coupling [61, 63, 64, 66] reveal that the effects of coupling alter the effective transmission channel. Therefore the effective channel with mutual coupling can be re-written as

$$\mathbf{H} = \left[\mathbf{C}_{rx}\mathbf{R}_{rx}{\mathbf{C}_{rx}}^H\right]^{1/2} \mathbf{H}_{idd} \left(\left[\mathbf{C}_{tx}\mathbf{R}_{tx}{\mathbf{C}_{tx}}^H\right]^{1/2}\right)^T, \tag{3.55}$$

where $\mathbf{C}_{rx}$ and $\mathbf{C}_{tx}$ are the coupling matrices for the receiver and the transmitter, respectively. Spatial correlation for the transmitter and receiver are denoted by matrices $\mathbf{R}_{rx}$ and $\mathbf{C}_{rx}$, respectively. Considering the receiver of a 2 × 2 MIMO wireless system the effective channel is given as

$$\mathbf{H} = \left[\mathbf{CRC}^H\right]^{1/2} \mathbf{H}_{iid}. \tag{3.56}$$

Considering two dipole antenna elements at the receiver, the coupling matrix is given as

$$\mathbf{C} = (Z_{load} + Z_s) \begin{bmatrix} Z_{load} + Z_s & Z_m \\ Z_m & Z_{load} + Z_s \end{bmatrix}^{-1}, \tag{3.57}$$

where Z_{load} and Z_s represent the load impedance and the self-impedance of the antenna elements. Mutual impedance is denoted by Z_m, which is a function of the dipole length, the antenna spatial distribution d and the antenna placement configuration [63]. Mutual impedance can be calculated using the induced EM field method, as described in [67]. In this case, mutual impedance is assumed to be matched to the self-impedance of the antenna, meaning $Z_m = Z_s$. With the combined effects of mutual coupling and spatial correlation, the channel in (3.56) can be written as

$$\begin{aligned} \mathbf{CRC}^H &= \begin{bmatrix} C_{1,1} & C_{1,2} \\ C_{2,1} & C_{2,2} \end{bmatrix} \begin{bmatrix} 1 & \rho_{1,2} \\ \rho_{2,1} & 1 \end{bmatrix} \begin{bmatrix} {C^*}_{1,1} & {C^*}_{1,2} \\ {C^*}_{2,1} & {C^*}_{2,2} \end{bmatrix} \\ &= P \begin{bmatrix} 1 & \tilde{\rho}_{1,2} \\ \tilde{\rho}_{2,1} & 1 \end{bmatrix}. \end{aligned} \tag{3.58}$$

From (3.58), it is evident that mutual coupling has two effects. Firstly, mutual coupling reduces the correlation coefficients, which is beneficial. Secondly, the received signal power is scaled, showing that there is a power loss penalty incurred by coupling effects. Power loss becomes significant with smaller antenna element spatial distribution d. Studies show that the detrimental effects of power loss incurred by coupling effects outweigh the beneficial effect of spatial correlation reduction [63, 66]. MIMO channel capacity is severely degraded as a result. In a MIMO-OFDM system, the power loss penalty introduces an additional deterioration of carrier frequency offset (CFO) estimation resulting in poor performance due to synchronisation errors [64].

Considering a 2 × 2 MIMO system with the Alamouti scheme, the system model incorporates the effective channel in (3.56) and the received signal in the first-time instant is given as

$$y_1 = \sqrt{\frac{E_s}{2}} \underbrace{\underbrace{\begin{bmatrix} C_{1,1} & C_{1,2} \\ C_{2,1} & C_{2,2} \end{bmatrix}}_{\mathbf{C}_{rx}} \underbrace{\begin{bmatrix} 1 & \rho_{1,2} \\ \rho_{2,1} & 1 \end{bmatrix}}_{\mathbf{R}_{rx}} \underbrace{\begin{bmatrix} h_{1,1} & h_{1,2} \\ h_{2,1} & h_{2,2} \end{bmatrix}}_{\mathbf{H}_{iid}}}_{\hat{\mathbf{H}}_e} \begin{bmatrix} x_1 \\ x_2 \end{bmatrix} + \begin{bmatrix} n_1 \\ n_2 \end{bmatrix}, \tag{3.59}$$

and at the second time instant the received is given as

$$y_2 = \sqrt{\frac{E_s}{2}} \begin{bmatrix} C_{1,1} & C_{1,2} \\ C_{2,1} & C_{2,2} \end{bmatrix} \begin{bmatrix} 1 & \rho_{1,2} \\ \rho_{2,1} & 1 \end{bmatrix} \begin{bmatrix} h_{1,1} & h_{1,2} \\ h_{2,1} & h_{2,2} \end{bmatrix} \begin{bmatrix} -x^*{}_2 \\ -x_1 \end{bmatrix} + \begin{bmatrix} n_1 \\ n_2 \end{bmatrix}, \tag{3.60}$$

where $\hat{\mathbf{H}}_e$ is the effective channel incorporating the coupling and correlation effects, E_s denotes the total transmit power available at the receiver and n_1, n_2, n_3 and n_4 denote the noise components modelled as uncorrelated zero-mean Gaussian random variables with variance $E\left\{|n_i|^2\right\} = N_0,\ i = 1, 2, ..., 4$. The received signal vector constructed at the receiver can be expressed as

$$\underbrace{\begin{bmatrix} y_2 \\ y^*{}_2 \end{bmatrix}}_{y} = \sqrt{\frac{E_s}{2}} \underbrace{\mathbf{C}_{r,e}\mathbf{R}_{rx,e} \underbrace{\begin{bmatrix} h_{1,1} & h_{1,2} \\ h_{2,1} & h_{2,2} \\ h^*{}_{1,1} & h^*{}_{1,2} \\ h^*{}_{2,1} & h^*{}_{2,2} \end{bmatrix}}_{\mathbf{H}_{idd,e}}}_{\hat{\mathbf{H}}_e} \underbrace{\begin{bmatrix} x_1 \\ x_2 \end{bmatrix}}_{\mathbf{x}} + \underbrace{\begin{bmatrix} n_1 \\ n_2 \\ n^*{}_3 \\ n^*{}_4 \end{bmatrix}}_{\mathbf{n}}, \tag{3.61}$$

where $\mathbf{C}_{r,e}$ and $\mathbf{R}_{rx,e}$ are the block diagonal matrices given by (3.62) and (3.62), they represent the effective coupling and correlation effects respectively [68].

$$\mathbf{C}_{r,e} = \begin{bmatrix} C_{1,1} & C_{1,2} & 0 & 0 \\ C_{2,1} & C_{2,2} & 0 & 0 \\ 0 & 0 & C^*{}_{1,1} & C^*{}_{1,2} \\ 0 & 0 & C^*{}_{2,1} & C^*{}_{2,2} \end{bmatrix}, \tag{3.62}$$

$$\mathbf{R}_{rx,e} = \begin{bmatrix} 1 & \rho_{1,2} & 0 & 0 \\ \rho_{2,1} & 1 & 0 & 0 \\ 0 & 0 & 1 & {\rho^*}_{1,2} \\ 0 & 0 & {\rho^*}_{2,1} & 1 \end{bmatrix}. \tag{3.63}$$

The compact matrix form of the received signal vector is reduced to

$$\mathbf{y} = \sqrt{\frac{E_s}{2}}\mathbf{C}_{r,e}\mathbf{R}_{rx,e}\mathbf{H}_{iid,e}\mathbf{x} + \mathbf{n} = \sqrt{\frac{E_s}{2}}\hat{\mathbf{H}}_e\mathbf{x} + \mathbf{n}. \tag{3.64}$$

Using MRC at the receiver and assuming perfect channel state information results in

$$\mathbf{z} = \left(\hat{\mathbf{H}}_e\right)^H \mathbf{y} = \sqrt{\frac{E_s}{2}}\hat{\mathbf{H}}_e^H\hat{\mathbf{H}}_e\mathbf{x} + \hat{\mathbf{H}}_e^H\mathbf{n}, \tag{3.65}$$

where $(\cdot)^H$ denotes the Hermitian transpose of the matrix. It is worth noting that irrespective of the coupling, correlation or the MIMO Gaussian channel $\mathbf{H}_{idd}$, the effective MIMO channel matrix, including coupling and correlation effects, is orthogonal [68]. That means $\hat{\mathbf{H}}_e^H\hat{\mathbf{H}}_e = \left\|\hat{\mathbf{H}}_e\right\|_F^2 \mathbf{I}_2$, where $\mathbf{I}_2$ is an identity matrix and $\|\cdot\|_F^2$ represents the Frobenius norm. Simplifying (3.65) further, the received signal vector can be written as

$$\mathbf{z} = \sqrt{\frac{E_s}{2}}\left\|\hat{\mathbf{H}}_e\right\|_F^2\mathbf{x} + \hat{\mathbf{n}} = \sqrt{\frac{E_s}{2}}\left\|\mathbf{C}_r\mathbf{H}\right\|_F^2\mathbf{I}_2 x + \hat{\mathbf{H}}_e^H\mathbf{n}. \tag{3.66}$$

Using maximal likelihood detection at the receiver, the SNR for each antenna element is expressed as

$$\eta = \frac{E_s}{2N_0}\left\|\mathbf{C}_r\mathbf{H}\right\|_F^2 = \frac{\rho}{2}\left\|\mathbf{C}_r\mathbf{H}\right\|_F^2 = \frac{\rho}{2}\sum_{i=1}^{R(\mathbf{C}_r\mathbf{H}\mathbf{H}^*\mathbf{C}_r)}\lambda_i\left(\mathbf{C}_r\mathbf{H}\mathbf{H}^*\mathbf{C}_r\right), \tag{3.67}$$

where ρ is considered to be the equivalent SNR of a SISO system. The parameters $R\left(\mathbf{C}_r\mathbf{H}\mathbf{H}^*\mathbf{C}_r\right)$ and $\lambda_i\left(\mathbf{C}_r\mathbf{H}\mathbf{H}^*\mathbf{C}_r\right)$ denote the rank and the i^{th} eigenvalue of the channel correlation matrix incorporating the effects of coupling. As noted previously, coupling effects reduce spatial correlation and the power for the effective channel matrix is scaled down.

3.5.3 Simulations

Fig. 3.16 shows the spatial correlation with and without coupling against antenna element spatial distribution d for two $\frac{\lambda}{2}$ dipole antenna elements at 2.4 GHz carrier frequency. The simulated antenna elements have a self-impedance that is matched to the mutual impedance, meaning $Z_m = Z_s$. In this case, the power delivered to the loading network is maximised. Correlation generally holds an inverse relationship with antenna element spatial distribution d. Fig. 3.16 shows that mutual coupling reduces correlation and effectively eliminates correlation at 10λ antenna separation. This provides independence of diversity branches and consequently signal propagation paths, which in turn effectively mitigates multipath fading effects.

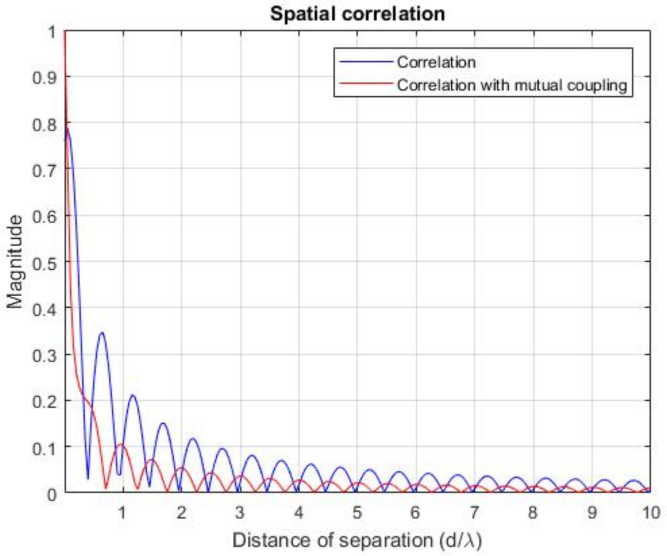

Figure 3.16. Effect of mutual coupling on spatial correlation.

Fig. 3.18 shows BER performance a MIMO wireless system for a high correlation value of 0.9 and antenna spacing of 0.1λ representing high coupling. In this scenario, it can be seen that in the presence of mutual coupling, the highly correlated environment is transformed into the less correlated scenario of Fig. 3.17. Consequently, this renders the same power gain of the MIMO system as achieved under the rich scattering environment, and the signal paths are decorrelated. Therefore, as a result of an increase in the BER curve slope, an increase in diversity gain in the MIMO system is achieved with the Alamouti scheme.

Fig. 3.20 and Fig. 3.19 shows the BER performance of the MIMO system under a rich scattering and a highly correlated environment, respectively. In these scenarios, antenna

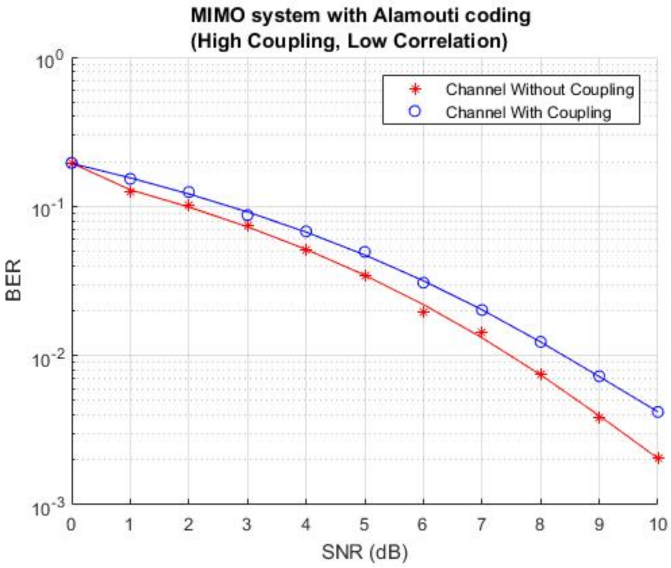

Figure 3.17. MIMO system with Alamouti coding for $\rho = 0.1$ and $d = 0.1\lambda$.

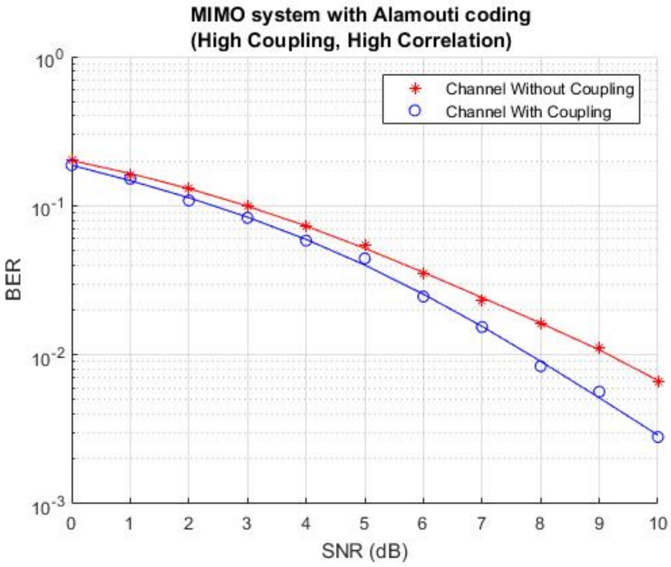

Figure 3.18. MIMO system with Alamouti coding for $\rho = 0.9$ and $d = 0.1\lambda$.

element spatial distribution d is increased to 10λ, which represents low mutual coupling effects. It is evident from Fig. 3.20 and Fig. 3.19 that the impact mutual coupling effects on BER performance under both propagation scenarios are negligible. Mutual coupling is effectively mitigated when the antenna elements are sufficiently distributed by at least 10λ, which in turn mitigates the power loss penalty that is more detrimental to BER performance than the reduced correlation. This confirms the common statement in literature that antenna element

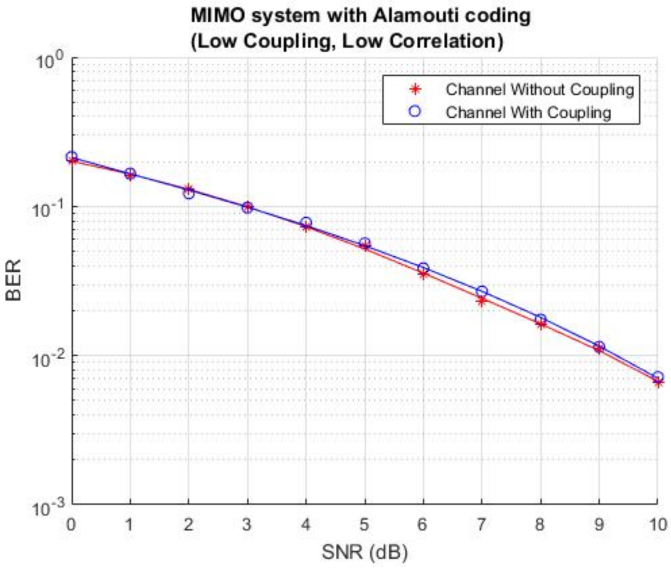

Figure 3.19. MIMO system with Alamouti coding for $\rho = 0.1$ and $d = 10\lambda$.

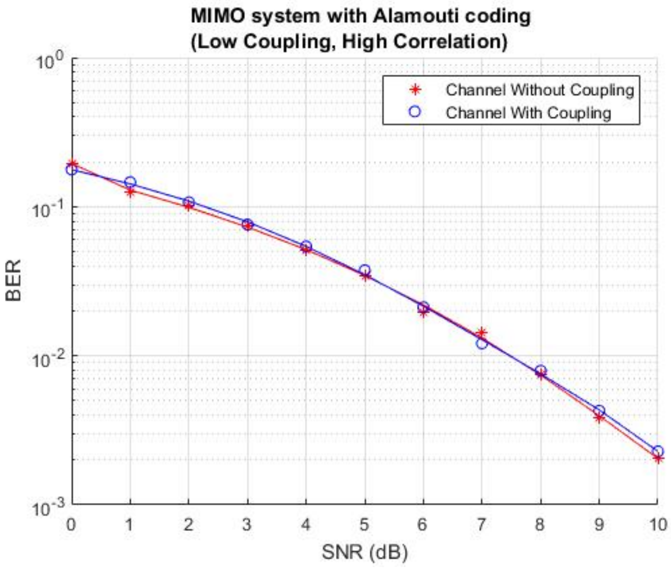

Figure 3.20. MIMO system with Alamouti coding for $\rho = 0.9$ and $d = 10\lambda$.

spatial distribution of at least 10λ is sufficient to render independence of diversity branches and decorrelated signal propagation paths.

3.6 CHAPTER SUMMARY

This chapter presented the quantitative analysis and simulations of the BER performance of PLC and diversity techniques. This chapter aimed to achieve the first objective of the research work, that is, to study the channel transfer characteristics of indoor low-voltage powerline channels and multiple antenna wireless systems, thereby determining the influence of each propagation environment in a hybrid channel established by the concatenation of a powerline channel and wireless channel. BER performance of single-carrier modulation and multi-carrier modulation was investigated in simulation to gain an understanding of the effects of the powerline multipath propagation environment. Powerline channel noise interferences are a combination of the impulsive and white background noise. Middleton's Class A noise model was used to investigate the effects of noise on single-carrier and multi-carrier modulation. OFDM was used as the multi-carrier method, and it was found to be robust against noise interferences of the powerline channel. Single-carrier modulation was found to have an error floor and, and unlike OFDM, an increase in transmit power does not effectively improve the error rate for single-carrier modulation. Therefore, OFDM is to be used as the channel access method for the powerline-wireless hybrid channel in subsequent chapters. The concept of signal diversity was further explored in this chapter through concepts of transmit diversity using the Alamouti scheme and receive diversity using diversity combining techniques. Simulation results show that the performance of multiple antenna wireless systems is effectively improved with the increase in diversity branches. Optimal performance was achieved through the Alamouti scheme due to its orthogonal code structure and addition of redundancy through both space and time dimensions. Signal combining methods still offer improved error rate performance at the penalty of the computational burden placed on the receiver. Signal combining methods will be used in subsequent chapters. Lastly, the effects of signal envelope correlation and mutual coupling in multiple antenna wireless systems are quantitatively presented in terms of BER performance. Simulation results show that the effects of mutual coupling are twofold. Under high correlation effects, mutual coupling reduces effects of correlation at a penalty of power loss incurred by coupling effects. However, the power loss penalty is reduced by increased spatial distribution between antenna elements. In practice, signal envelope correlation is often observed as a manifestation of coupling effects. Therefore, the signal enveloped correlation metric will be used in subsequent chapters.

CHAPTER 4 POWERLINE-WIRELESS HYBRID CHANNEL CHARACTERISATION

4.1 CHAPTER OVERVIEW

Characterisation of a communication channel is a crucial task performed to gain an understanding of the channel transfer characteristics. Channel characterisation allows for developing accurate models for the channel of interest and suitable communication protocols that will provide efficient coverage and reliability of the channel. Section 4.2 presents an overview of channel sounding methods. To attain channel transfer characteristics, an exciting signal is injected into the channel, this is "sounding" the channel, and then the receiver "listens" to the channel response. This concept is the so-called "channel sounding", and the practical realisation is the so-called "channel sounder". Depending on the measurement scenario and the purpose for channel sounding, the choice for the channel sounding method varies considerably, and it also depends on whether time domain or frequency domain measurements are required. Section 4.3 presents the powerline-wireless channel problem. A unified channel is established by concatenating a powerline channel and a wireless channel. The communication link is established from the wireless transmitter transmitting through a unified powerline-wireless channel and received by a PLC receiver. The direction can also be from PLC transmitter to wireless receiver. Section 4.4 presents a sequence-based channel sounding approach using maximum length sequences (MLS), otherwise known as m-sequences, and software defined radio (SDR) is used to attain channel transfer characteristics. Fast varying conditions of the powerline network can be effectively captured using the m-sequence channel sounding method. The SDR realisation of the sounding method is flexible to design alterations and allows for a high degree of scalability. Additionally, channel sounding is performed in real-time and which allows for live observation of channel transfer characteristics. Section 4.5 presents the estimation of coherence bandwidth (CB), average channel attenuation (ACA) and power delay profile timing delays from attained measurements. Section 4.6 presents the hybrid channel performance in terms of the estimated channel parameters from measurements. The effect of the powerline channel path length on the hybrid channel transfer characteristics is investigated.

4.2 CHANNEL SOUNDING METHODS

Channel sounding techniques can be broadly classified into narrowband channel sounding and wideband channel sounding. Narrowband channel sounding is the earliest of the sounding techniques, whereby an unmodulated single-tone sinusoidal continuous-wave is injected into the channel to excite channel, then variations in power and phase are observed and captured by moving a stationary receiver. The sounder transmitter transmits a series of unmodulated single-tone sinusoidal continuous-waves with various frequencies to excite the channel. The receiver, commonly implemented by a spectrum analyser, measures the received signals and displays the spectrum. This method allows for attaining the channel transfer function. The pitfall of this method is that it cannot capture the frequency correlation of the transmitted signal. Therefore multipath signal propagation behaviour that is apparent in communication channels cannot be observed with this method [69].

The pitfalls of the narrowband sounding method can be overcome by wideband channel sounding techniques. This method allows for sounding a wider bandwidth and observing small-scale effects such as the time and frequency coherence of the channel of interest. Key channel parameters such as coherence bandwidth (CB), average channel attenuation (ACA), RMS delay spread (RMS-DS) and maximum delay spread can be extracted from the observed measurements. Depending on whether the time-domain or frequency-domain characteristics are required, wideband channel sounders can be classified into time domain characterisation and frequency domain characterisation. From now henceforth, channel sounding implies wideband channel sounding.

4.2.1 Channel sounding for frequency-domain

Channel sounding for frequency-domain characterisation implies the direct estimation of the channel transfer function from frequency measurements. The complex channel frequency response is attained by sweeping a sinusoidal carrier across various frequencies within the band of interest in quick succession, then at each swept frequency the amplitude and phase of the received signal are compared to the transmitted signal. The transmitted waveform that covers a range of frequencies Δf within the band of interest can be expressed as

$$s(t)_{fd} = \exp\left[2\pi j\left(f_0 t + \Delta f \cdot \frac{t^2}{2T_{chirp}}\right)\right], \quad 0 \leq t \leq T_{chirp}, \tag{4.1}$$

where the term $f_0 t + \Delta f \cdot \frac{t^2}{2T_{chirp}}$ denotes the instantaneous frequency that has a linear relationship with time and allows for different frequencies to be measured at different times. A vector network analyser (VNA) can be used as the swept-frequency solution as it can stimulate and directly measure the complex frequency response of the channel. Another approach is to measure different frequencies at the same time, which means multiple sinusoidal signals with different frequencies, amplitudes and phases are generated by the transmitter and simultaneously transmitted. The complex frequency response is attained by comparing the transmitted signals to the received signals.

4.2.2 Channel sounding for time-domain

Channel sounding for time-domain characterisation is used to estimate the channel impulse response directly. Generally, a periodic narrow pulse is injected into the channel to excite the channel, then correlation methods at the receiver are used to obtain the channel impulse response. The periodic narrow pulse $c(t)$ can be expressed as

$$s(t)_{td} = \sum_{i=0}^{N-1} a_i p\left(t - iT_{rep}\right), \tag{4.2}$$

the number of narrow pulses used in the measurement is denoted by N, the amplitude of the i^{th} pulse is denoted by a_i. $p(t)$ is the channel exciting waveform that is the periodically repeated pulse transmitted at intervals T_{rep}. Depending on the choice of the waveform $p(t)$, a time-domain channel sounder can be realised in two forms, namely impulse sounder and correlative sounder.

4.2.2.1 Impulse sounder

The transmitter of the impulse sounder repetitively transmits a short pulse waveform with a pulse width of T_w within intervals of T_{rep} to excite the channel. The bandwidth of interest is given by $B_w = \frac{2}{T_w}$. At the receiver side, a bandpass filter of bandwidth B_w is applied on the received signal, the signal is then amplified, and the attenuation profile is attained by applying envelope detection. The impulse response is generally displayed on a digital oscilloscope. The operation of a periodic pulse sounder for indoor environments is shown in Fig. 4.1. Intuitively, each transmitted narrow pulse captures the small-scale effects of the multipath propagation environment, which is a "snapshot" of multipath behaviour within a specific time interval, then combining these "snapshots" provides observation of multipath behaviour over the measurement period. Synchronisation for the impulse sounder is of paramount importance in order to maintain the signal phase information. Synchronisation for short range indoor measurements is generally achieved by connecting the transmitter and receiver with a coaxial or fibre cable. For long range outdoor measurements, Global Positioning System (GPS) is more practical and also has the advantage of attaining the location of measurements as well.

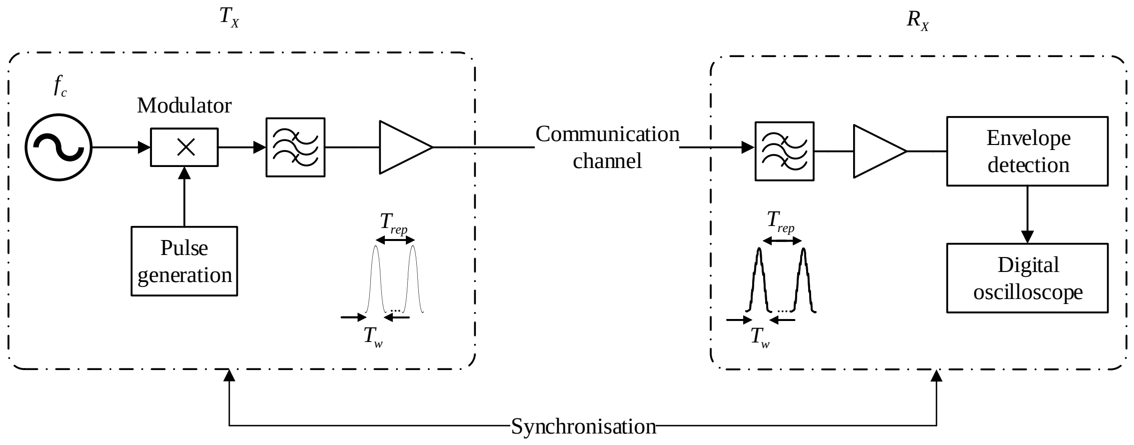

Figure 4.1. Operation principle of a periodic pulse sounder.

4.2.2.2 Correlative sounder

The correlative sounder is based on pulse compression of linear systems, which compresses the bandwidth of the wideband signal in order to attain wideband measurements. Assuming that the transceiver and the channel are linear systems, the output $y(t)$ is expressed as the convolution of the channel impulse response $h(t)$ and the pulse $p(t)$ as

$$y(t) = h(t)\,p(t) = \sum h[\tau]\,p[t-\tau]. \tag{4.3}$$

Correlative sounders generally use a pseudo-random (PN) sequence to excite the channel. A maximum-length PN sequence (m-sequence/MLS) is a class of periodic binary sequences generally used in correlative sounders generated using linear feedback shift registers (LFSR). m-sequences are widely used for wideband channel sounding because they are easily and rapidly created, they are balanced and have excellent AWGN properties that translate into excellent cross-correlation and autocorrelation properties. Pulse compression can be realised in two forms, namely the convolution matched filter and the swept time delay cross-correlation (STDCC).

The convolution matched filter is generally realised as a surface acoustic wave (SAW) filter. This sounding technique has the advantage of attaining channel measurements without the need to re-generate the transmitted m-sequence at the receiver side. However, the complex realisation of SAW filters and the high computation cost limit the performance of this sounding technique in the sounding system. The STDCC technique achieves pulse compression by time dilatation, thereby reducing the data captured and relaxes the memory requirements of the sounding system. The received m-sequence is correlated with an exact copy of the transmitted m-sequence generated at the transmitter. Consider a signal $p[t] = 2a_i - 1 \in \{1, -1\}$, where $a_i \in \{0, 1\}$ and $i \in \{1, ..., L_m\}$. Correlation at the receiver produces the normalised autocorrelation function $R_m[k]$ given as

$$R_m\left[k\right] = \frac{1}{L_m} \sum_{i=1}^{L_m} p\left[i\right] p\left[i+k\right] = \begin{cases} 1 & \text{for } k = 0, \\ -\frac{1}{L_m} & \text{for } k \in \{1, ..., L_m\} \end{cases}. \tag{4.4}$$

Fig. 4.2 shows the operation principle of the correlative sounder. The generated m-sequence is composed of 1s and 0s, and then it is then modulated using Binary Phase Shift Keying (BPSK) to produce ±1s for transmission. Passband modulation by a carrier frequency f_c is performed by the analog front-end. At the receiver, the same m-sequence with BPSK modulation is produced clocked at a slightly lower rate of $f_{RX} - \Delta f$, where Δf is the slip rate. The impulse response of the sounded channel is attained at the output of the correlator that uses (4.4) and (4.3) to produce the time-domain response.

The STDCC sounding technique is commonly referred to as the "sliding correlator sounder" in literature [70]. The sliding correlator was first used by Cox as an effective and efficient method for sounding wide bandwidths of wireless channels. Benvenuto [71] provided the first rigorous mathematical analysis of the sliding correlator in efforts to eliminate early guest-and-test methods of the sliding correlator that relied on the erroneous approximation of design parameters and required tedious tweaking to attain acceptable performance levels.

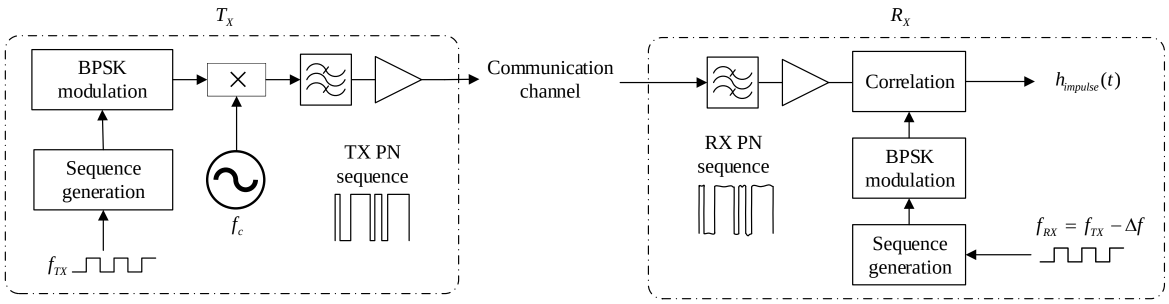

Figure 4.2. Operation principle of a correlative sounder.

Benvenuto's work was expanded upon by Talvilie and Poutanen [72] by providing quantitative descriptions for the relations of the sliding correlator design parameters and performance levels, more especially the dynamic range. Numeric analysis was carried out in [73] to generate plots showing the relationship between the dynamic range and the slide factor parameter for different m-sequences of different lengths, and a systematic design approach was developed from the observed results of the plots. A comprehensive set of design metrics and the rules governing the design process of the sliding correlator sounder for optimal performance are given in [70]. The design rules are developed to attain optimal performance levels of dynamic range, temporal resolution, processing gain and Doppler resolution.

The sliding correlator sounding technique using MLS is used to attain time-domain channel measurements of the hybrid powerline-wireless channel. This approach is cost-effective as it can be realised by cheap off-the-shelf components compared to VNA single-box solutions that tend to be expensive. The sounding method also allows for physical separation between the transmitter and receiver and therefore eliminates the need for synchronisation. Other advantages of the sliding correlator sounder include low peak-to-average power ratio (PAPR), which implies efficient use of the power amplifiers. The m-sequence can be generated with long periods to attain a large time-bandwidth product, which implies high signal-to-noise rates and low error rates. Compared to impulse methods, the correlative sounder allows conducting non-invasive measurements on highly interference sensitive channels. The one pitfall of the correlative sounder is the complicated extraction of phase information, the complexity of the channel sunder can quickly rise when phase information is required.

4.3 POWERLINE-WIRELESS HYBRID CHANNEL

In order to gain an understanding of the underlying issues of a hybrid powerline-wireless channel, the hybrid channel problem is first outlined. The hybrid powerline-wireless channel considered is a unified channel established by the concatenation of an indoor low-voltage powerline cable and wireless propagation environment. Considering a symbol period T_{sym} that is longer than the channel coherence time, the channel can be considered linear and time-invariant in the symbol period T_{sym}. Considering the continuous-time input signal $x(t) \in \mathbb{R}$ band-limited to $[0, B]$ injected into the hybrid channel, where $t \in \mathbb{R}$, then the output of the channel can be expressed as

$$y_p(t) = x_p(t) \star [h_p(t) \star h_w(t)] + n_p(t), \tag{4.5}$$

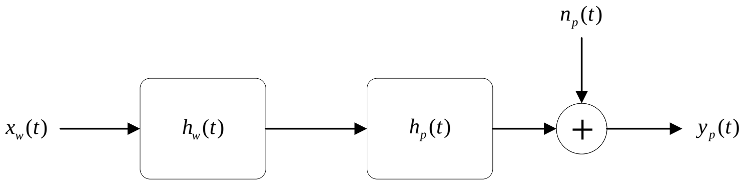

Figure 4.3. Wireless to power line transmission direction.

for the case of a wireless transmitter to a powerline receiver. In the case of a powerline transmitter to a wireless receiver, the channel output can be expressed as

$$y_w(t) = x_w(t) \star [h_w(t) \star h_p(t)] + n_w(t), \tag{4.6}$$

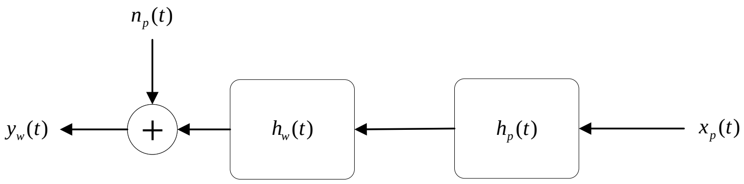

Figure 4.4. Power line to wireless transmission direction.

where $y_p(t)$ and $y_w(t)$ denote the powerline and wireless outputs, respectively, $x_p(t)$ and $x_w(t)$ denote the powerline and wireless inputs, respectively. Powerline and wireless channels are denoted by $h_p(t)$ and $h_w(t)$, respectively. For the sake completeness, the components $n_p(t)$ and $n_w(t)$ represents the noise components of the powerline and wireless channel, respectively. The symbol $\star$ denotes the convolution operator. It should be noted that noise analysis of the hybrid channel is not the focus of this dissertation. Powerline noise characterisation is a subject of many studies and is well addressed in literature. Powerline impulsive noise is usually observed in the tens of megahertz range [31, 34]. Therefore, due to the simplicity of the constructed hybrid channel with only one branch and a PLC centre frequency in the range of hundreds of megahertz, the effects of powerline impulsive noise can safely be avoided.

Channel transfer characteristics $h_p(t)$ and $h_w(t)$ are of paramount importance because they highlight the usefulness of the hybrid channel. The hybrid channel is defined as $h_w(t) \star h_p(t) = h_{eq}(t)$. The frequency response, $H_{eq}(f)$, highlights the attenuation characteristics of the channel, which is simply the Fourier transform of the impulse response of $h_{eq}(t)$. It should be noted that estimation of the channel transfer characteristics is performed by digital processing of the discrete versions of the $y_p(t)$, $y_w(t)$, $x_p(t)$ and $x_w(t)$, that is $y_p[n]$, $y_w[n]$, $x_p[n]$ and $x_w[n]$ respectively. The estimated channel characteristics are also discrete versions of $h_{eq}(t)$, that is $h_{eq}[n]$.

A few challenges are to be faced when characterising and analysing such a hybrid channel. Firstly, the noise components of the powerline and wireless channels cannot be concatenated and modelled as the same process due to considerate variation of the noise sources and noise characteristics [31, 57]. Due to a lack of standard powerline channel models, powerline channel noise interference is a function of a particular powerline network. The impedance experienced in the powerline channels also varies considerably depending on the branching intensity of the powerline network. Connected loads in the powerline network result in varying channel realisations over time [26, 74]. Different channel realisations are observed over time due to varying impedance levels. Additionally, coupling devices for the powerline and wireless channel vary considerably, causing mismatched and asymmetrical power transfer characteristics from powerline to wireless and vice versa. To avoid significant losses due to asymmetrical power transfer characteristics a single branch powerline network is used. The outlined issues show that the measurement, characterisation and analysis of such a hybrid channel is very challenging.

4.4 CHANNEL SOUNDING METHOD

The channel sounding methodology is outlined by first describing the channel excitation method. It should be noted that the sounding methodology was implemented on a digital platform, and discrete versions of the baseband signals were digitally processed to attain the channel transfer characteristics. Channel transfer characteristics can be obtained by exciting the channel using three popular methods, namely impulse-based stimulation, continuous-wave stimulation and sequence-based stimulation. As discussed previously, the performance of continuous-wave and impulse-based methods is severely degraded by interference due to the high dependence on emission measurements. Limitations faced by the continuous-wave and impulse-based methods can be overcome by employing sequence-based methods. The channel is excited by a repetitive sequence structure, which can be varied. The sequence structure is known at the receiver a priori, and then correlation methods at the receiver are used to return a scaled impulse response. The active inference that is present is suppressed by the employed correlation methods. Unlike the continuous-wave and impulse-based methods, sequence-based methods allow for multiple and separate measurements of frequency or impulse response of the channel by employing additional antenna elements.

4.4.1 Pseudorandom binary sequence generator

A sequence-based method employs a pseudorandom binary sequence a_i such that $a_i \in \{0, 1\}$. a_i has a repetitive structure of period L such that $a_{i+L} = a_i$. The sequence can be generated by a recursive algorithm such that the n^{th} term of the sequence is determined by a linear combination of the previous N terms given as

$$a_n = \sum_{i=1}^{N} c_i a_{n-i}. \tag{4.7}$$

The value of the n^{th} term in (4.7) is determined by N previous feedback coefficients $c_i \in \{0, 1\}$. The N previous terms $\{a_{-N}, a_{1-N}, \cdots, a_{-2}, a_{-1}\}$ must be known a priori in order to determine the zeroth term if it is assumed that $c_N = 1$, then a_{n-N} can be used to calculate a_n. The summation in (4.7) uses modulo-2 operators. A characteristic polynomial $f(x)$ can be used to describe the sequence a_i using the feedback coefficients c_i as

$$f\left(x\right) = 1 - \sum_{i=1}^{N} c_i x^i. \tag{4.8}$$

The reciprocal of $f(x)$ is defined as

$$G\left(x\right) = \frac{1}{f\left(x\right)} = \sum_{i=1}^{N} a_i x^i, \tag{4.9}$$

where $G\left(x\right)$ is referred to as the generating polynomial because the coefficient terms of $G\left(x\right)$ are made up of the pseudorandom binary sequence terms a_i. In (4.9) it is assumed that the N previous terms are seeded such that $\{a_{-N}, a_{1-N}, \cdots, a_{-2}\} = 0$ and $a_{-1} = 1$, any seeding variation of the N initial terms such that they are not all simultaneously zero will result in a pseudorandom binary sequence that is a phase shifted version of a_i.

Maximum length sequences (MLS), otherwise known as m-sequences, are a class of pseudorandom binary sequences. MLSs are produced using (4.7). Using previous N terms, an MLS will have the longest possible period of length L defined as

$$L = 2^N - 1. \tag{4.10}$$

MLSs are produced by an efficient characteristic polynomial of (4.8) because it will have the longest non-repeating sequence from only a few of the previous N terms.

Correlative sequences are classified into binary and non-binary sequences. MLSs fall into the class of binary sequences. MLSs have the disadvantage of an out-of-phase error with a value of $v_{oop} = -1$, which introduces an error in the periodic autocorrelation function (PACF). This limits the dynamic range to $D_r = N_{seq} - |v_{oop}|$ [75]. MLSs have the advantage of a constant magnitude and therefore have a peak-to-average-power ratio (PAPR) of unity. This relaxes the automatic-gain-control (AGC) requirements of SDRs and analog RF front-ends. The PACF error of MLSs can be overcome by employing non-binary sequences. There exist perfect non-binary sequences that provide the desired $v_{oop} = 0$ and the full dynamic range $D_r = N_{seq}$ is attained. The v_{oop} can be improved by increasing the length L of the sequence.

A linear feedback shift register (LFSR) is generally used as a hardware realisation of the recursive sequence formula in (4.7). To produce the m-sequence, the previous N bits of the sequence are stored in a shift register of length N-bit and are used to produce the a_n terms of the sequence. Modulo-2 arithmetic is implemented using XOR gates to produce the weighting factors c_i. The a_n term is then produced by weighting the i^{th} terms stored in registers with their respective coefficients c_i. For each clock cycle, the summation according to (4.7) is fed back to the input of the shift register, and the register output is the $(n-N)^{th}$ term. The described sequence generator is known as a simple shift register generator (SSRG) or the Fibonacci implementation [76]. The positions of feedback registers for an SSRG are a function of (4.8). Moreover, only registers with a corresponding coefficient of $c_i = 1$ are selected for feedback summation. This is to ensure that the length of the sequence a_i equals to $L = 2^N - 1$. The SSRG offers low implementation complexity at the cost of long propagation delays because with only one input and one output, each i^{th} term must propagate through all stages of the register. An alternative hardware realisation of (4.7) is the modular shift register generator (MSRG) or the Galois implementation.

The architecture of MSRG has a single output and multiple inputs, therefore (4.8) does not directly describe the feedback loop of the MSRG. For a given characteristic polynomial, the modulo-2 addition is performed between the output of the N^{th} register and that of the $(j-1)^{th}$ register, and the summation is fed into the j^{th} register. At the same time, the N^{th} register output is fed to the shift register output. For a polynomial of $f(x) = 1 - x^2 - x^5$, the SSRG and MSRG architectures are shown in Fig. 4.5 and Fig. 4.6, respectively. MSRG allows for a high degree of flexibility of the generated m-sequence. Unlike the SSRG, the parallel paths in the feedback loop provide shorter propagation delays, and faster clock rates are achieved [70].

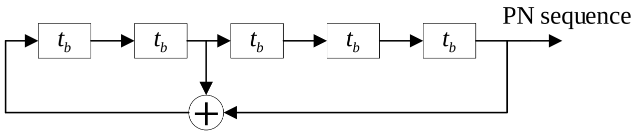

Figure 4.5. Simple shift register PN sequence generator.

Sequence generation for the correlative sounder is performed in software following the SSRG architecture. By using a bit-orientation implementation in software, a direct realisation of

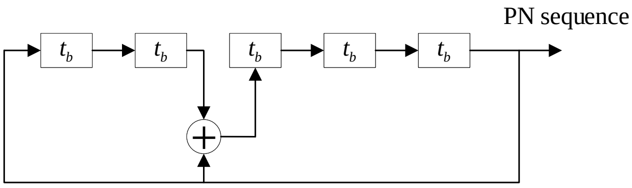

Figure 4.6. Multiple shift register PN sequence generator.

the SSRG architecture is achieved in software. The sequence generator is implemented in software using the flow graph in Fig. 4.7. The generator is generalised for polynomial degrees of up to 32. For an input sequence with length L the degree of the polynomial is calculated, and the toggle mask which is a binary value of length N that defines the feedback position with 1s, is attained from a lookup table. The output bit is initialised to 1. This is because a modulo-2 sum of the output with the feedback positions is fed back into the register, if the most significant bit is 1 an effect of flipping all the bits of the mask is applied, else the bits of the mask are shifted one position to the right for the length of the sequence. The produced sequence is BPSK modulated.

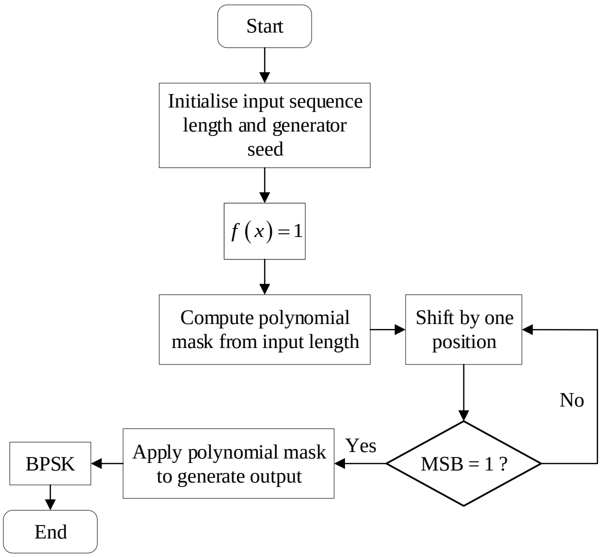

Figure 4.7. PN sequence generator for channel sounding.

4.4.2 Correlative sounder impulse response

The sequence-based hybrid channel sounding discussed here is for the wireless to powerline transmission direction, as will be shown in results, the direction could also be from powerline to wireless. A channel stimulation sequence $x[t]$ is produced at the transmitter, and infinite repetitions of the sequence are emitted from the PRBS source forming the correlative sequence $x_{seq}[t]$ as

$$x\left[t\right]=\sum_{i=-\infty}^{\infty}x_{seq}\left[t-iT_{seq}\right], \tag{4.11}$$

where $T_{seq}=T_s\cdot N_{seq}$ is the duration of the sequence, T_s and N_{seq} are the sampling rate and length of the sequence respectively. The received signal with hybrid channel effects is given as

$$y\left[t\right]=x\left[t\right]\star h_{eq}\left[t\right]+n\left[t\right], \tag{4.12}$$

where $h_{eq}[t]=h_p[t]\star h_w[t]$ is the equivalent low-pass hybrid channel impulse response. For the sake of completeness, the noise term is included. However, it should be noted that PLC noise analysis is not the focus of this work. $y[t]$ is the PLC output $y_p[t]$, $h_{eq}[t]$ contains the frequency selectivity and fading effects of both the wireless and powerline channel. The transmitted signal repetitions may be disrupted by internal sources such as buffer trigger flow events or external sources in the wireless and powerline channels. Therefore, a window function of the sequence duration is used, such that all disrupted sequences are muted, and only full duration sequences are passed for processing. The window output is given as

$$y_{win}\left[t\right]=\sum_{j=-\infty}^{\infty}y\left[t-k_jT_{seq}\right]\boldsymbol{.}\,w\left(\left(\left[t-k_jT_{seq}\right]\right)/T_{seq}\ \right), \tag{4.13}$$

where $k_j>k_{j-1}$ is a monotonous growing index, $w(t/T)$ is a window function for the sequence duration $[0,T)$. The received windowed sequence is then correlated with the stimulation sequence $x_{seq}[t]$ known a priori at the receiver generated using the same PRBS generator as the transmitter. The output is expressed as the complex conjugate time-reversed convolution of the received sequence

$$y_{corr}\left[t\right]=y_{win}\left[t\right]*{x^*}_{seq}\left[-\left(t-T_{seq}\right)\right]. \tag{4.14}$$

The correlation output can then be separated into the signal term $y_{corr,s}[t]$ and noise term $y_{corr,n}[t]$ as

$$\begin{aligned} y_{corr}\left[t\right] &= \left(x\left[t\right] * h_{eq}\left[t\right]\right) * {x^*}_{seq}\left[-\left(t-T_{seq}\right)\right] \\ &+ \left(n\left[t\right] * h_{eq}\left[t\right]\right) * {x^*}_{seq}\left[-\left(t-T_{seq}\right)\right] \qquad (4.15) \\ &= y_{corr,s}\left[t\right] + y_{corr,n}\left[t\right]. \qquad (4.16) \end{aligned}$$

Under the assumption of good AWGN properties of the stimulation sequence chosen, the impact of the noise term can be safely neglected. Convolution associative property is then applied to the correlation output as

$$y_{corr}\left[t\right] = \left(x\left[t\right] * {x^*}_{seq}\left[-\left(t-T_{seq}\right)\right].\right) * h_{eq}\left[t\right]. \qquad (4.17)$$

Taking into account the constant out-of-phase PACR value v_{oop} of the correlative sequence constant gives

$$y_{corr}\left[t\right] = \left(v_{oop} + \left(N_{seq} - v_{oop}\right)\sum_{i=-\infty}^{\infty} \delta\left[t-t_i\right]\right) * h_{eq}\left[t\right], \qquad (4.18)$$

where the measurement time is substituted by $t_i = (i+1)T_{seq} - T_s$. To attain the impulse response, the convolution distributive property and Dirac function shifting property are applied, this provides a time-shifted and scaled value version of the impulse response as

$$y_{corr}\left[t\right] = \left(N_{seq} - v_{oop}\right)\sum_{i=-\infty}^{\infty} h_{eq}\left[t-t_i\right] + v_{oop} * h_{eq}\left[t\right], \qquad (4.19)$$

where the first term of (4.19) is the time-shifted and value-scaled version of the impulse response. The term $v_{oop} * h_{eq}\left[t\right]$ the bias error introduced by a non-zero v_{oop}. The desired channel impulse response is attained from y_{corr} by normalisation with the length of the sequence N_{seq} as $y_{norm}\left[t\right] = \frac{1}{N_{seq}} \cdot y_{corr}\left[t\right]$.

The bias error component of (4.19) gets reduced by the increase in the length of the sequence N_{seq}. The channel impulse result y_{norm} still contains some linear distortions caused by the measurement apparatus and physical realisation components tolerances, and this is corrected for by convolving y_{norm} with $h_{eq,fft}[t]$ as

$$\begin{aligned} y_{ch}\left[t\right] &= y_{norm}\left[t\right] * h_{eq,fft}\left[t\right] \qquad (4.20) \\ &\approx \sum_{i=-\infty}^{\infty} h_{ch}\left[t - t_i\right] = \sum_{i=-\infty}^{\infty} h_{ch}\left[\tau, t_i\right]. \qquad (4.21) \end{aligned}$$

Therefore, the impulse response with the finely granulated time τ is attained.

4.4.3 Correlative sounder implementation

The sequence-based channel sounding method was implemented on a digital platform and using BladeRF x40 SDRs. The transmission of the correlative sequence was used for channel stimulation, and the reception was used for correlation and channel characterisation. The transmitted sequence generator structure is known a priori at the receiver. The transmitter and receiver associated SDRs were connected to embedded host computers running a Linux 18.04 Bionic Beaver operating system. The processing, which is the live sequence generation at the transmitter and sequence correlation at the receiver, is performed under GNU radio platform on a PC. The BladeRF devices' Cypress FX3 microcontroller provides a seamless connection between the PC and the device through USB 3.0. I/Q data samples are RF modulated by the device's LimeMicro LMS6002D RF transceiver, which is software configured for RF transmission and reception through the device's Altera Cyclone IV E FPGA firmware. GNU radio is an open-source software toolkit used to develop and implement SDR applications. C++ and python are the two programming languages used in GNU radio. All the computationally extensive signal processing and performance critical modules are written in C++, and python is used as a high-level language to create a live executable flow graph of the interconnected processing modules. This approach means that the agility of software development in a high-level language can be maximised while at the same time sidestepping its drawback of slow performance by only acting as a "glue" code and offloading the heavy signal processing to the compiled C++ code. Simplified Wrapper and Interface Generator (SWIG) is used to "glue" the python code to the C++ code as shown in Fig. 4.8. SWIG generates a wrapper for C++ modules and generates the corresponding python code (*.py) and library (*.so) so that these classes and functions can be included in python.

Fig. 4.9 shows the executable GNU radio channel sounder transmitter flow graph constructed by interconnected processing modules. A continuous source repeatedly generates the *m*-

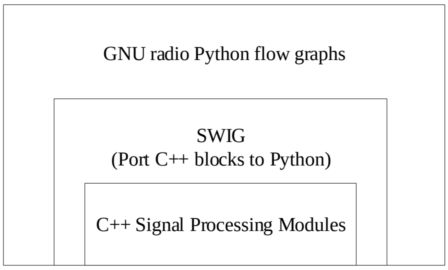

Figure 4.8. GNU Radio Swig interface.

sequence with a sequence with length of $L = 1024$, the polynomial degree for the shift register is calculated as $degree = ceil(\log_2(L))$, which gives a degree of 10, thus $f(x) = x^{10} + x^4 + 1$ and the mask for the shift register is 0x00000204. I/O data types between the flow graphs modules were implemented in complex float-32. A multiplicative constant is then used to scale the BPSK generated PN sequence to amplitude limit of $|1|$, that is because if the signal magnitude is greater than $|1|$, then it will suffer clipping. The Osmocom module is used to interface the BladeRF SDR to the GNU radio platform for data transfer. Passband modulation and transmission of the channel stimulation signal performed through the BladeRF SDR's LMS6002D processor.

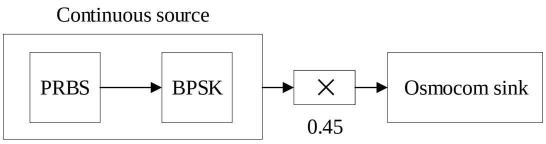

Figure 4.9. GNU radio channel sounder transmitter flow graph.

Fig. 4.10 shows the GNU radio channel sounder receiver executable flow graph constructed by interconnected processing modules. After wireless to powerline channel coupling, the complex float-32 I/Q data samples from the Osmocom module are passed to a DC blocker module. This is because the BladeRF x40 SDR does not perform frequency down conversion using an intermediate frequency, but rather it is a direct-conversion receiver, otherwise known as a homodyne receiver. These types of receivers have a common flaw in a large DC offset in the received signal. To counter this, a DC blocker with a suppression bandwidth of 850 kHz is used to mitigate the effects of DC interference. A sequence gate module is used to window to received PN sequence to the duration of the sequence to mute interferences and ensure that only full length sequences are passed for correlation. Another constant source at the receiver is used to generate the same m-sequence using the same parameters as the transmitter. Cross-correlation between the received and generated m-sequence is performed to calculate the impulse response. Normalisation by the length of the sequence is then applied to the impulse response samples. A file sink is then used to store the attained impulse response for offline processing in Python to extract channel parameters.

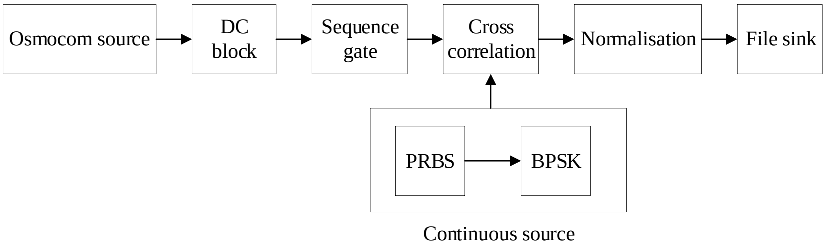

Figure 4.10. GNU radio channel sounder receiver flow graph.

The 2.4 GHz Industrial, Medical and Scientific (ISM) band was used for wireless transmission because it is unlicensed and therefore allowed the channel sounding system to be operated without the need for a license. RF transmission was performed at a centre frequency of 2.42 GHz using omnidirectional antenna elements. Signal down-conversion was performed on the wireless signal using the RF2052 PLL frequency synthesiser and mixer. RF2052 is a low-power, wideband frequency synthesiser chip with local oscillator (LO) generation through an integrated fractional-N PLL with VCOs and dividers that are used to produce a low-phase noise LO signal with a fine frequency resolution of 1.5 Hz. The chip also includes an integrated wideband bidirectional RF mixer that allows for up-conversion and down-conversion of signals in the frequency range of 30 MHz to 2500 MHz. With a centre frequency of 2.42 GHz, an LO signal of with 2.12 GHz centre frequency is generated to produce a PLC signal with a centre frequency 300 MHz. The PLC transmitted signal is received by another SDR set to receive at the lower centre frequency of 300 MHz. I/Q samples passband modulation and demodulation, and low-pass and bandpass filtering are all handled by the analog front-end of the SDRs. The previously discussed PAPR properties of the sequence-based method also relax the gain control requirements of the SDRs.

Adjacent WiFi channels were monitored using Acrylic WiFi Home Scanner. Acrylic WiFi Home is a free tool that is used to scan WiFi channels in 2.4 GHz and 5 GHz bands. It provides real time measurements of WiFi signals' strength in adjacent channels. RF transmission was performed mostly in night times, given the lesser traffic in WiFi channels, therefore mitigating erroneous RF measurements. Caution was exercised to ensure that RF transmission does not exceed the legal transmission power limits regulated by ICASA. The legally enforced maximum transmission power limit of a wireless communication link in the 2.4 GHz band is 100 mW (20 dBm), thus an upper boundary of 20 dBm was placed on RF transmission power.

The use of SDRs and GNU radio allowed for a modular design approach of the channel sounding method and provided the advantage of a high degree of flexibility to design alterations, furthermore, the software-based reconfiguration is cost effective and time efficient. The results of the sequence correlation were recorded and were processed off-line using Python to attain the PDP, frequency response and the RMS-DS, CB and ACA channel statistics. The hybrid channel that was measured and characterised is illustrated by Fig. 4.11.

A simple T-network was constructed to make up the PLC network. The PLC network points A and C were matched to 50 Ω impedance while branch B was left open. One SDR was used for wireless transmission, then frequency down-conversion is performed from 2.42 GHz to 300 MHz using the RF2052 PLL frequency synthesiser/mixer, followed by powerline coupling, and finally the receive SDR. Capacitive coupling was used to interface the powerline channel to the RF hardware. The coupling circuit shown in Fig. 4.12, can be used for both coupling at the transmitter and decoupling at the receiver [77]. A 1:1 transformer is used for galvanic isolation to protect

the SDR hardware. On the primary side of the transformer, transient voltage surge suppressors (TVSS) with a metal oxide varistor (MOV) are used for surge protection of the coupling circuit and SDR hardware from high voltage spikes of the power distribution network. On the secondary side of the transformer and the Zener diodes are connected back to back to limit transient currents on the RF hardware side. The channel sounding parameters are given in Table. 4.1.

4.4.4 Correlative sounder analysis

The channel sounding experiment parameters given in Table. 4.1 impose some limits on the performance of the channel sounder such as dynamic range, maximum multipath delay,

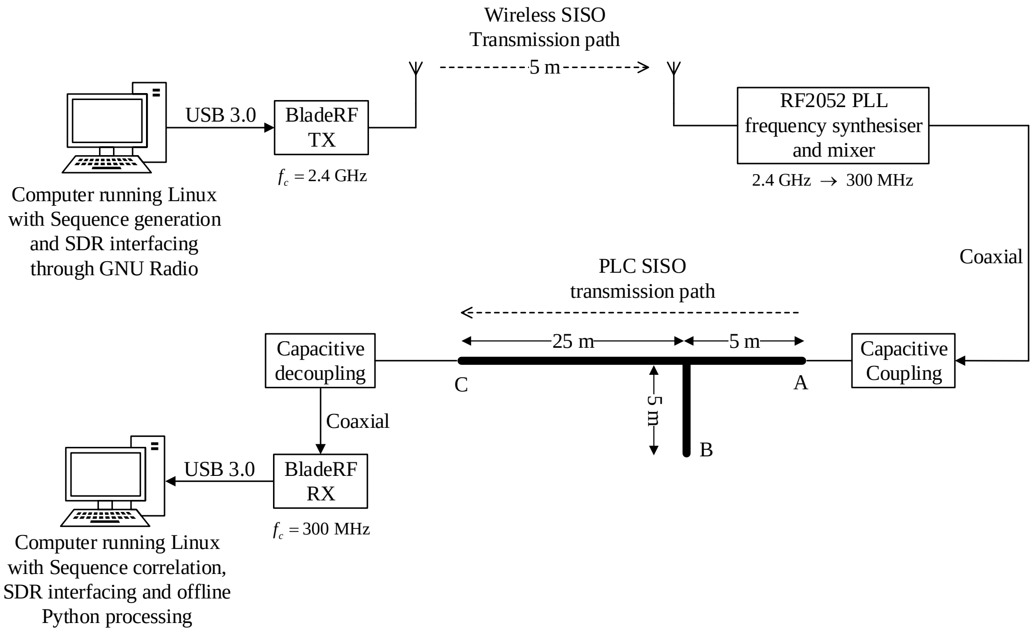

Figure 4.11. Hybrid wireless-powerline channel sounding system.

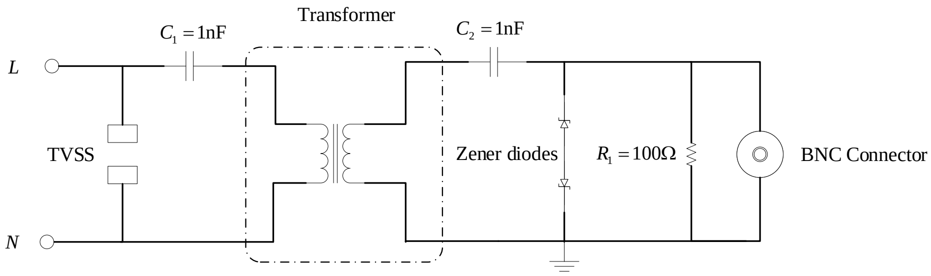

Figure 4.12. Capacitive coupling circuit.

maximum path length, temporal resolution and processing gain. The correlative sounder performance metrics are summarised in Table. 4.2. The performance metrics are the results of rigorous mathematical and statistical analysis of channel sounding through the correlative sounder presented in [70]. Fundamental equations in Table. 4.2 were developed to provide a concise methodology for optimal performance of a correlative channel sounder. The performance metrics have three main dependencies, namely, sequence length L, sliding factor γ and centre frequency f_c. Maximum multipath delay, maximum path length and temporal resolution are each calculated for the powerline channel and wireless channel due to the different centre frequencies.

Table 4.1. Channel Sounding Parameters

Parameter	**Value**
Wireless centre frequency	2.42 GHz
PLC centre frequency	300 MHz
Sampling frequency	35 MHz
Sequence type	MLS
Sequence length	1024
Measurement 3 dB bandwidth	28 MHz
DC suppression bandwidth	850 kHz
Measurement time	10 s

The PN sequence $x_{seq}[t]$ transmitted can be considered a direct sequence spread spectrum signal (DSSS). Sliding correlation is performed on the spread spectrum signal of centre frequency f_c by multiplying the complex-baseband signal with an exact copy of the PN sequence at the receiver with a slower frequency of $f_c' = 0.99 f_c$. The measured channel impulse response using the sliding correlator produces a time-dilated correlation, meaning the measured bandwidth is compressed, thereby easing the hardware requirements. Time dilation as a result of the sliding correlation can be described by the slide factor γ given as

$$\gamma = \frac{f_c}{f_c - f_c'}. \tag{4.22}$$

A minimum γ that provides acceptable levels of dynamic range D_r is given as $\gamma_{min} = 1.41L^{1.09}$. Values of γ less than γ_{min} give D_r that deviates outside of 20% range of the ideal D_r, that is for $\gamma \geq \gamma_{min}$ then $0.8D_{r,ideal} \leq D_r \leq D_{r,ideal}$ where $D_{r,ideal} = 20\log_{10}(L)$ dB.

Frequency shifting of the spread spectrum signal does not affect the fidelity of the correlative sounder, that is the same γ is preserved in the wireless and powerline constituents of the hybrid channel. Frequency shifting merely changes f_c from 2.42 GHz to 300 MHz. For this reason, maximum multipath delay, maximum path length and temporal resolution must each be calculated for wireless and powerline channels. For $L = 1024$ the slide factor is calculated as $\gamma_{min} = 1.41 \cdot 1024^{1.09}$, then $\gamma_{min} \backsimeq 2694$.

Table 4.2. Correlative Sounder Performance Metrics

Capability	Equation
Processing gain	$G_p = 10\log_{10}(\gamma)$ dB
Dynamic range	$D_r \approx 16\log_{10}(L)$ dB
Temporal resolution	$T_{res} = \frac{1}{f_c}$ dB
Maximum multipath delay	$\tau_{max} = \frac{L}{f_c}$ dB
Maximum path length	$d_{max} = c \cdot \frac{L}{f_c}$ dB

4.4.4.1 Processing gain

Processing gain of the sliding correlator is described as the ratio of output SNR to input SNR of the spread spectrum signal, in terms of dB scale G_p is defined as

$$G_p = 10\log_{10}\left(\frac{SNR_{out}}{SNR_{in}}\right)\ dB. \tag{4.23}$$

Processing gain serves to spread the power spectrum of noise and other interference sources in the channel over the measurement bandwidth. Due to multiplication processes at the receiver, the interference power spectral density will be spread across the complex baseband bandwidth given by B_W. In most cases for $f_c \approx f_c^{'}$, therefore the interference power is then reduced by the slide factor magnitude γ, for this reason, the sliding correlator G_p is defined as

$$G_p = 10\log_{10}(\gamma). \tag{4.24}$$

For $\gamma = 2694$, $G_p = 34\ dB$. It should be noted that the definition of G_p for the sliding correlator differs from the processing gain of a DSSS system that uses true correlation, which is given as $G_p = 10\log_{10}(L)$. This discrepancy comes as a result of the nature sliding correlator operations.

4.4.4.2 Dynamic range

The sliding correlator dynamic range D_r represents the ability of the channel sounder to detect weak signals. For an m-sequence length of L and $\gamma = \gamma_{min} = 2694$, D_r is estimated as

$$\begin{aligned} D_r &\approx 16\log_{10}(L) && (4.25) \\ &\approx 48.16\ dB. && (4.26) \end{aligned}$$

4.4.4.3 Temporal resolution

Temporal resolution T_{res} provides a measure of the resolvable relative delay between multipath components. It is the minimum lag between multipath components that can be measured. T_{res} is estimated as

$$T_{res} = \frac{1}{f_c}. \tag{4.27}$$

T_{res} is dependent on the centre frequency f_c, therefore for a centre frequency of 2.42 GHz, the resolvable relative delay for the wireless environment is 0.4132 ns. For a centre frequency of 300 MHz, the resolvable relative delay for the powerline channel is 3.33 ns.

4.4.4.4 Multipath delay and path length

Multipath resolution of the correlative sounder provides a measure of the maximum multipath component that can be unambiguously measured by the channel sounder. It is a function of the m-sequence length L and centre frequency f_c given as

$$\tau_{max} = \frac{L}{f_c}. \tag{4.28}$$

The transmitted m-sequence periodicity places an upper limit on τ_{max}, therefore to ensure that no significant multipath components beyond τ_{max} will be neglected by the channel sounder $L = 1024$. For an m-sequence of length 1024, $\tau_{max} = 0.4231\ \mu s$ for the wireless environment and $\tau_{max} = 3.41\ \mu s$ for the powerline channel. A high value of τ_{max} is required in the powerline environment due to a significant number of multipath propagation components of the channel. It is expected that the information-carrying signal will experience significant multipath propagation in the powerline channel than in the wireless channel because of line-of-sight (LOS) conditions in the wireless channel. The maximum resolvable path length d_{max} of the propagation environment is estimated by multiplying τ_{max} by the free space propagation velocity $c = 3 \times 10^8\ m.s^{-1}$. For the wireless environment, $d_{max} = 127\ m$ and for the powerline channel $d_{max} = 1024\ m$.

4.5 PARAMETER ESTIMATION

Hybridism of the powerline and wireless channel brings forth a concatenation of challenges such as multipath propagation and fading effects experienced in each channel. The previously defined channel sounding method is used to estimate the channel impulse response of the hybrid channel directly. The impulse response $h_{eq}(t)$ represents the imparted low-pass filtering characteristics of the hybrid channel on the information-carrying signal. Applying signal processing transformations to $h_{eq}(t)$, the channel frequency response and power delay profile (PDP) of the hybrid channel can be attained. From the frequency response and PDP, channel performance statistics such as RMS-DS, average channel attenuation (ACA) and coherence bandwidth can be extracted. The PDP is defined as the measure of received signal power through a multipath propagation channel as a function of time delay. It is attained by taking the time or spatial average of the squared impulse response of the measured hybrid channel given as

$$P(\tau) = \frac{1}{N} \sum_{i=1}^{N} |h(\tau, t_i)|^2. \tag{4.29}$$

Fig. 4.13 shows a plot model of the PDP of a multipath channel. Four main time-delay characteristics of the multipath environment can be identified from the PDP. Firstly, the most important time-delay parameter is the root mean square delay spread (RMS-DS) σ_τ. It is defined as the second central moment of the channel PDP, and it will be defined in more detail shortly. In a multipath environment, strong signal echoes that have longer delays will contribute more to σ_τ. Therefore, the channel multipath spread indication is provided by σ_τ, consequently it provides an indication of potential ISI. σ_τ can also be considered as the standard deviation about the channel mean access delay μ_τ. μ_τ is defined as the first central moment of the PDP with respect to the first arrival time τ_A of the multipath propagation channel. τ_A is defined as the time delay that corresponds to the first signal echo arrival of the transmitted signal in the multipath environment. A final time-delay parameter is the maximum excess delay τ_m. τ_m is defined as the time after which the PDP magnitude falls below a predefined threshold. It presents the measured last echo in the multipath channel, therefore $\tau_m = \tau_{max}$.

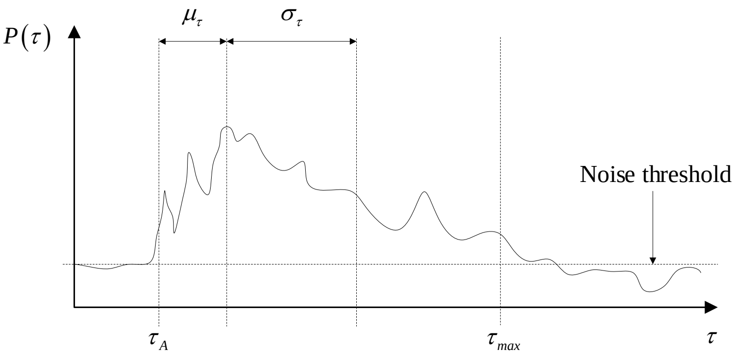

Figure 4.13. Power delay profile of multipath channel.

4.5.1 RMS-DS

RMS-DS is defined as the second central moment of the PDP. It is a distribution of the transmitted signal power in a multipath propagation environment. The RMS-DS for the sampled channel impulse response is given as

$$\sigma_\tau = \sqrt{\mu'_\tau - {\mu_\tau}^2}, \tag{4.30}$$

where μ_τ is the mean access delay such that

$$\mu_\tau = \frac{\sum\limits_{n=0}^{L_{ch}-1} n|h_{eq}[n]|^2}{\sum\limits_{n=0}^{L_{ch}-1} |h_{eq}[n]|^2} \text{ and } \mu'_\tau = \frac{\sum\limits_{n=0}^{L_{ch}-1} n^2|h_{eq}[n]|^2}{\sum\limits_{n=0}^{L_{ch}-1} |h_{eq}[n]|^2}, \tag{4.31}$$

where $h_{eq}[n] = h_{eq}(\tau, t_i)|_{t_i = nT_s}$, where $T_s = 1/f_s$ is the sampling frequency and L_{ch} is the length of the channel for evaluating the RMS-DS.

4.5.2 Coherence bandwidth

Coherence bandwidth (CB) of a multipath channel represents the frequency range over which the channel can be considered to be flat, which is the frequency range over which spectral components are admitted with equal gain and linear phase. The spectral components that fall within the coherence bandwidth frequency range will experience correlated amplitude fading. A wideband signal with a bandwidth that extends beyond the coherence bandwidth will experience frequency selectivity of the channel. The CB parameter provides information about the channel frequency domain that allows for investigating the efficiency of different modulation techniques and for decisions to be made regarding the degree of complexity of the receiver for a communication system.

To date, there is no definitive value for the specification of the CB parameter, this is because for practical channels, the direct evaluation of CB following theoretical analysis is often impractical. In practice, the CB parameter is often evaluated from the PDP response of the channel [78]. CB is generally understood as the frequency separation at which the amplitude correlation falls below some defined threshold, usually the spectral amplitude correlation thresholds are defined as 0.5, 0.7 and 0.9. Taking the Fourier transform of the PDP, an estimate of the frequency correlation function is attained as

$$|S(\Delta f)| = |F(P(\tau))| = \left| \int_{-\infty}^{\infty} P(\tau)\, e^{-j2\pi\Delta f} \right|. \tag{4.32}$$

As shown in Fig. 4.14, $|S(\Delta f)|$ provides the spectral amplitude correlation for the bandwidth of interest. The spectral amplitude correlation threshold is defined at 0.5. In studies involving powerline channel statistical analysis [27, 79, 80], a threshold of 0.5 was observed to relax the requirements of the communication hardware and system physical layer architecture. This is especially beneficial for PLC systems with high operating frequencies, however at lower frequencies, < 100 MHz, a much strict metric of 0.9 correlation threshold is used. The value of the CB for 0.5 correlation threshold denoted by B_{c50} is the value of Δf at which the following condition is met

$$|S(\Delta f = B_{c50})| = 0.5 \cdot |S(\Delta f = 0)|. \tag{4.33}$$

As shown in Fig. 4.14 for spectral correlation, there may be clearly resolvable peaks that may cross the defined threshold of 50% of the maximum correlation value more than once on the plot. In such a case, for the purposes of analysis, B_{c50} is evaluated as the value equal to the lowest Δf frequency for which the plot crosses the predefined threshold. It must be noted that this approach does not affect the final conclusions made about the fading characteristics of the hybrid fading channel.

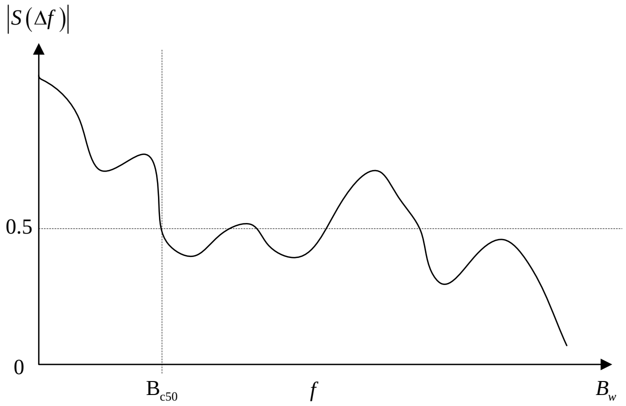

Figure 4.14. Spectral components amplitude correlation.

4.5.3 Average channel attenuation

Average channel attenuation (ACA) indicates the attenuation level of the low-pass transfer characteristics imparted by the hybrid channel on information-carrying signals. The attenuation level also provides an estimate of the expected channel capacity from the hybrid channel. ACA is given as

$$ACA = -10\log_{10}\left(\frac{1}{N}\sum_{n=0}^{N-1}\left|H_{eq}\left[n\right]\right|^{2}\right), \tag{4.34}$$

where $H_{eq}[n]$ is the discrete frequency response of the samples' impulse response $h_{eq}\left[n\right] = h_{eq}\left(\tau, t_i\right)\big|_{t_i=nT_s}$.

4.6 HYBRID CHANNEL PERFORMANCE

A simple hybrid channel was first constructed as shown in Fig. 4.15 with a maximum path length of thirty metres for the powerline channel. Powerline channel path length between the transmitter and the receiver was then reduced by intervals of five meters while keeping the wireless channel path length constant. This was done to produce four other hybrid channel realisations to investigate the effects of powerline channel path length on the hybrid channel performance. The channel sounding method was then applied to the other four hybrid channels to conduct the investigations.

The channel shown in Fig. 4.15 is labelled as channel five. The attained impulse response of channel five is shown in Fig. 4.16. Clear resolvable peaks of the impulse response represent the signal echoes due to the multipath propagation nature of the powerline channel. However, due to the simplicity of the T-network powerline channel, signal echoes are observed to

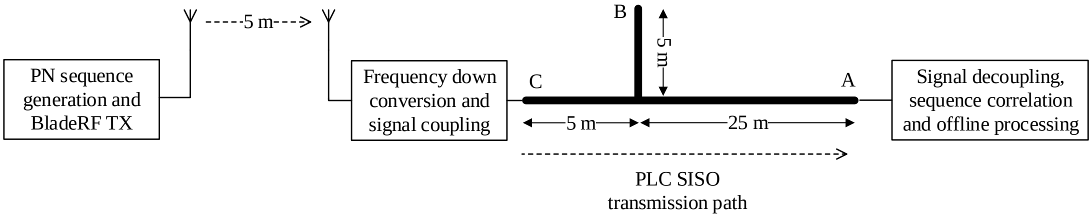

Figure 4.15. Hybrid wireless-powerline channel five.

diminish quickly. This can also be attributed to the fact that the transmitter and receiver are stationary.

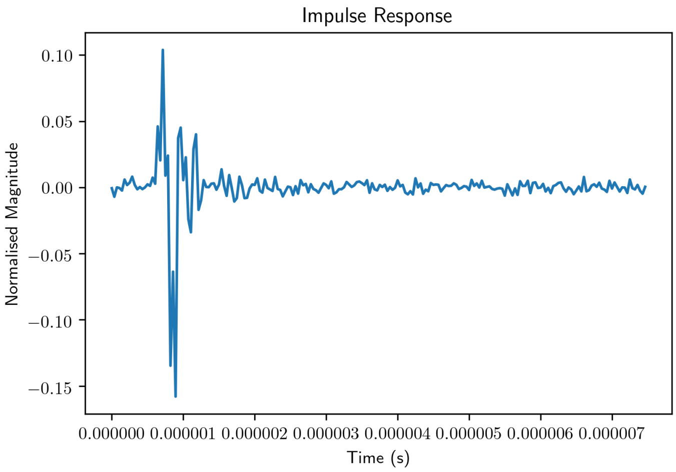

Figure 4.16. Impulse response of hybrid channel five.

From the impulse response of channel five, a Fourier transform was applied to obtain the frequency response characteristics of the channel. The frequency response of the hybrid channel for the wireless to powerline channel transmission direction is shown in Fig. 4.17, and that of the powerline to wireless channel transmission direction is shown in Fig. 4.18. The frequency response in both figures show comparable attenuation profiles. In both transmission directions, a pronounced notch in the frequency response shows that the hybrid channel is frequency selective. Frequency selectivity is a result of the open branch of the powerline channel. Generally, indoor powerline networks are densely branched and frequency selectivity is to be expected. Therefore a robust error detection and error correction method will be required for data transfer and communication applications. Channel attenuation was estimated using the ACA parameter. For the wireless to powerline transmission direction $ACA = 63\ dB$ and for powerline to wireless channel transmission $ACA = 72\ dB$. The high attenuation in powerline to wireless direction is due to the skin effect phenomenon of the powerline cables that the high frequency signal experiences first hand before the wireless channel. As shown in Fig. 4.17 and Fig. 4.18, the location of the notch gives an estimate of the channel coherence bandwidth from the transmission centre frequency. Coherence bandwidth of approximately 2.3 MHz can be observed in both transmission directions. From this observation, a paramount result of channel symmetry can be confirmed. This means that the channel fading characteristics are independent of the transmission direction. Channel symmetry is beneficial for full-duplex communication systems, meaning that the same transmitter and receiver structures can be used.

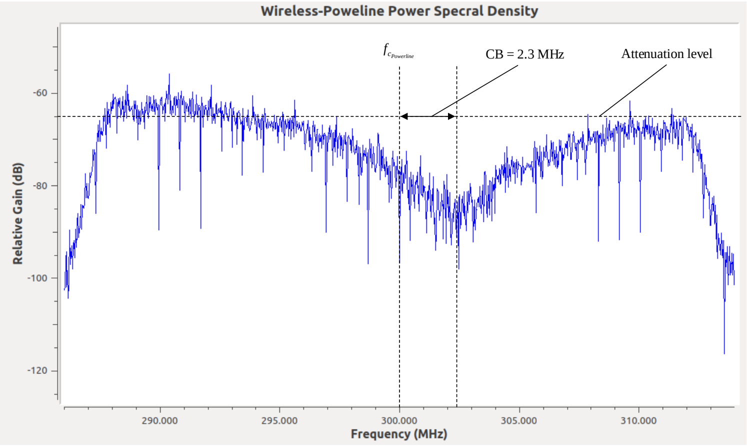

Figure 4.17. Frequency response of wireless to powerline direction of hybrid channel five.

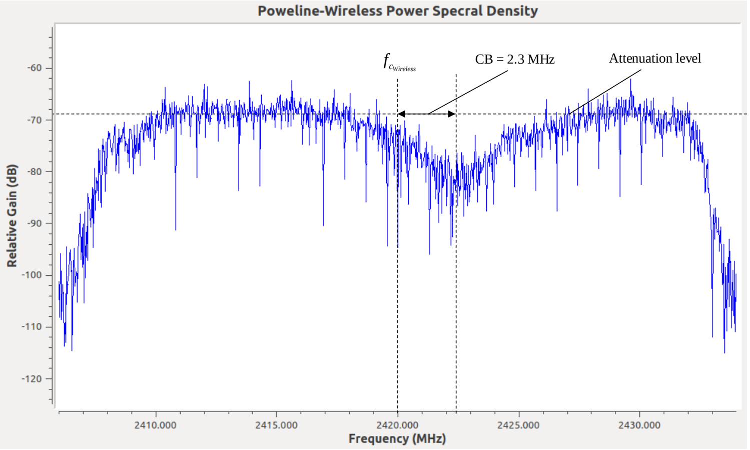

Figure 4.18. Frequency response of powerline to wireless direction of hybrid channel five.

The PDP of channel five estimated from the impulse response is shown in Fig. 4.19. It shows the received signal echoes with varying strengths as a function of time delay. The clearly resolvable peaks of the PDP response show the signal echoes as a result of multipath propagation of the powerline channel. The signal echoes are observed to quickly diminish as a result of the simplicity of the T-network powerline channel. The first signal arrival time is estimated at $\tau_A = 0.31\ \mu s$ and the last echo is estimated at the maximum delay spread of $\tau_{max} = 0.81\ \mu s$. The estimated time delay parameters for channel five are summarised in Table. 4.3.

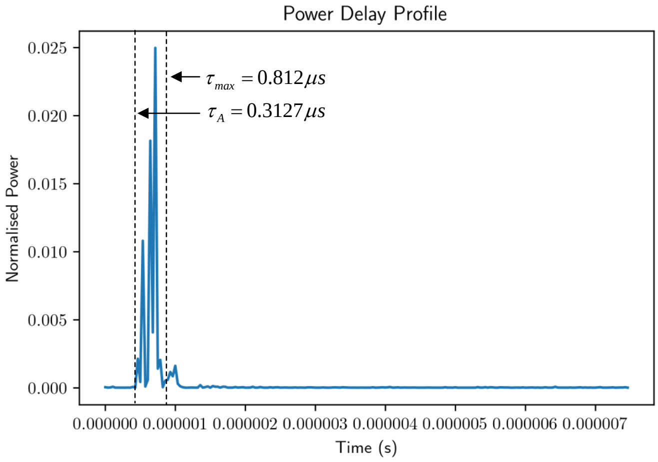

Figure 4.19. Power delay profile of hybrid channel five.

Table 4.3. Channel Five Time Delay Parameters

Channel parameter	**Value**
σ_τ	$0.6572\ \mu s$
μ_τ	$0.446\ \mu s$
τ_A	$0.312\ \mu s$
τ_{max}	$0.812\ \mu s$

Fig. 4.20 shows the spectral components correlation response estimated by applying a Fourier transform to the PDP of channel five. A maximum value of the correlation function is given as $|S(\Delta f = 0)| = 0.3375$. The coherence bandwidth of $B_{c_{50}}$ is estimated by defining a spectral amplitude correlation threshold of 0.5. This means $B_{c_{50}}$ is the frequency value estimated at $0.5 \cdot |S(\Delta f = 0)| = 0.1687$. The corresponding frequency value from the centre frequency is estimated at 2.3 MHz, thus $B_{c_{50}} \approx 2.3$ MHz. The estimated value of $B_{c_{50}}$ substantiates the coherence bandwidth results of the frequency response of the hybrid channel shown in Fig. 4.17 and Fig. 4.18.

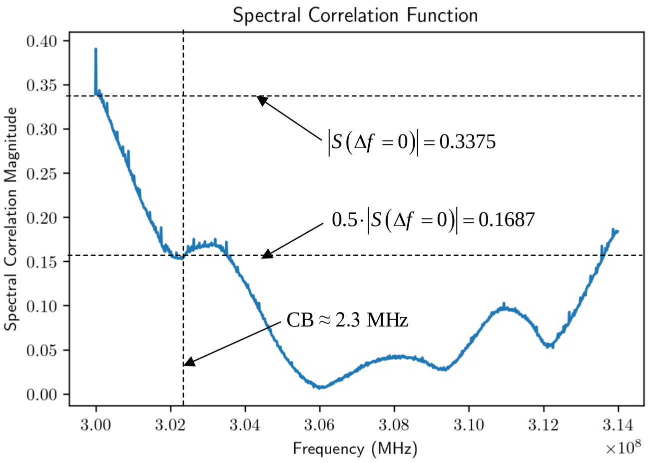

Figure 4.20. Spectral correlation function plot of hybrid channel five.

The effect of powerline channel path length was investigated by reducing the powerline channel length by five metre intervals to realise four variants of the hybrid channel. The channel sounding methodology was applied to each of the four channels to produce the channel responses, PDPs and spectral correlation plots for each channel. Variation of the powerline path length and corresponding channel numbers are shown in Fig. 4.21. The wireless channel path length was kept constant.

The estimated impulse responses for all five channels are shown in Fig. 4.22. For each channel, the impulse responses clearly show resolvable peaks owing to multipath propagation. The normalised magnitude is observed to decrease with the increase in the path length. From the estimated impulse responses, the PDPs of each channel are given in Fig. 4.23. Similar to Fig. 4.22, the normalised power of the PDP is observed to decrease as the powerline channel path length increases. In addition to the undesirable skin effect phenomenon of powerline cables as a result of a high carrier frequency, the impedance of the powerline channel increases with the increase in length. Powerline channel modelling based on the bottom-up approach employs transmission line theory to model the channel transfer characteristics [27, 38, 81, 82]. Channel modelling using this approach is generally achieved by sectioning the powerline channel into unit lengths and calculating the per-unit-length parameters. From transmission line theory, the per-unit-length resistance of the powerline channel is directly proportional to the length of the channel. As a result, the powerline channel impedance increases with channel length.

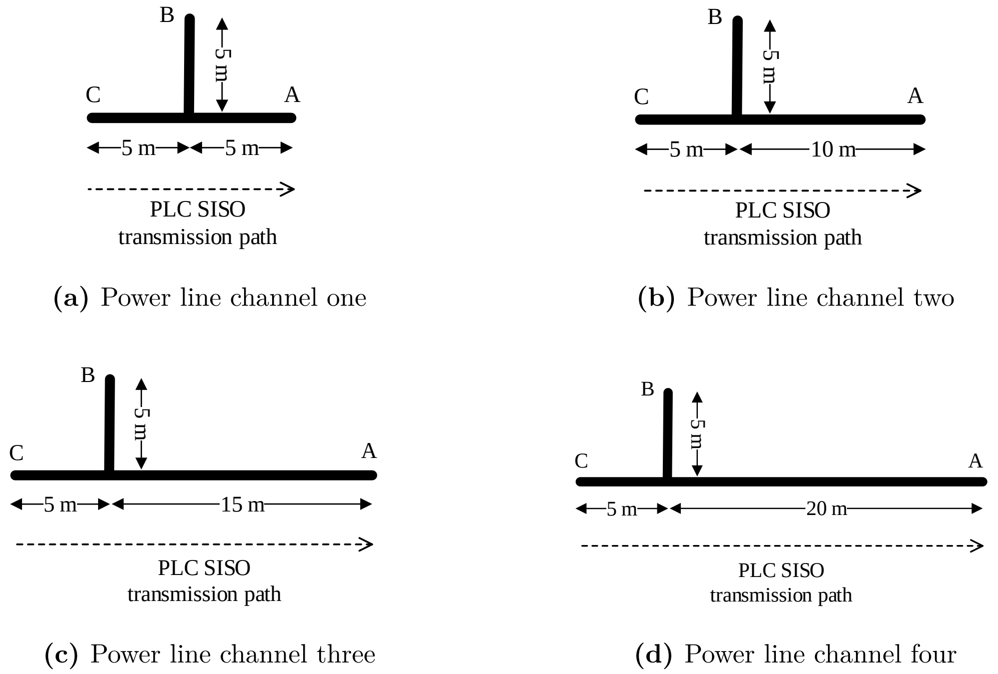

(a) Power line channel one

(b) Power line channel two

(c) Power line channel three

(d) Power line channel four

Figure 4.21. Power line channel path variation while keeping the wireless path constant

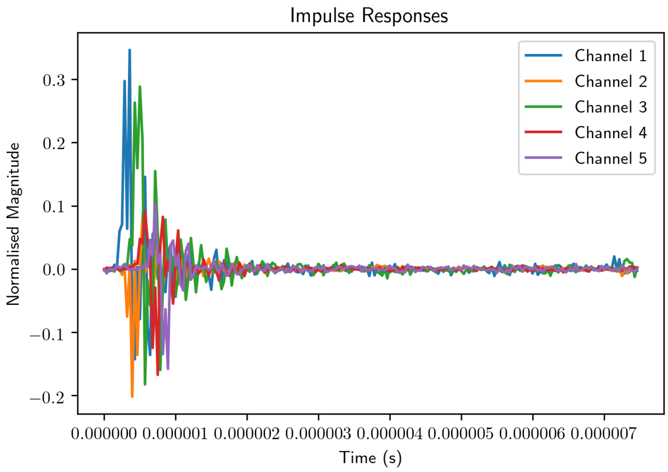

Figure 4.22. Impulse responses of all channels.

Spectral component amplitude correlation plots for all channels are shown in Fig. 4.24. Small but yet notable differences in coherence bandwidth of each channel are observed. Fig. 4.24 shows that the longest powerline channel path has the lowest coherence bandwidth, and the shortest powerline channel path has the highest coherence bandwidth. This observation is corroborated by several studies on the subject of channel characterisation [27, 78–80].

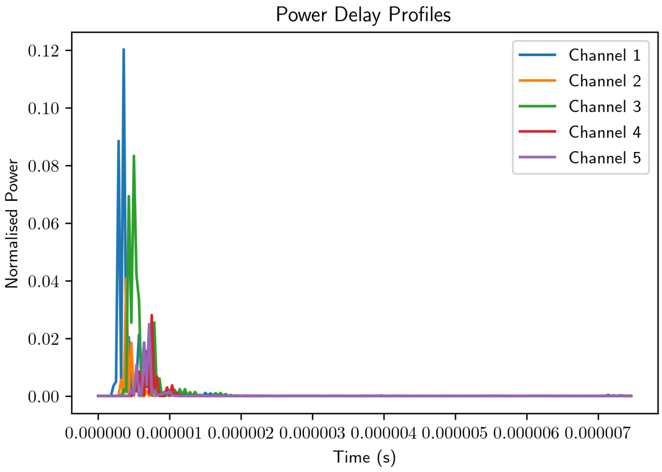

Figure 4.23. Power delay profiles of all channels.

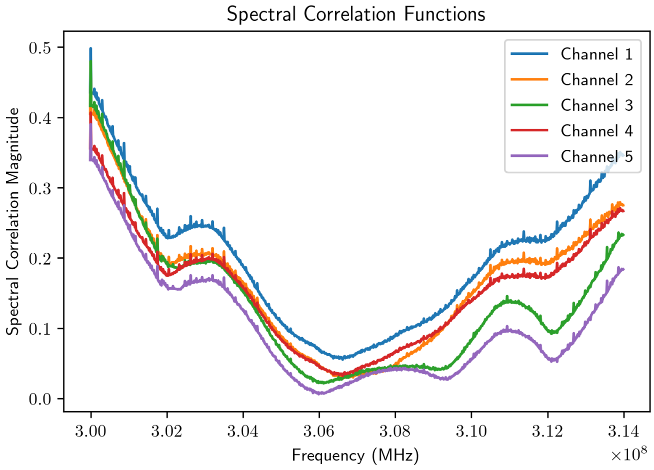

Figure 4.24. Spectral amplitude correlation of all channels.

Some studies use a relation between CB and RMS-DS when conditions such as propagation characteristics of the channel are random, the channel is wide sense stationary and multipath components time delays are uncorrelated are met. The simple inverse relation of $B_{c50} = \frac{1}{5 \cdot \sigma_\tau}$ is used for a spectral correlation threshold of 0.5 and $B_{c90} = \frac{1}{50 \cdot \sigma_\tau}$ is used for a spectral correlation threshold of 0.9. Since σ_τ is directly proportional to the path length, then B_c is inversely proportional to path length.

Estimated PDP timing delays, CB and ACA for all channel realisations for the wireless to powerline transmission direction are summarised in Table. 4.4. It is evident from the

Table 4.4. Performance parameters of powerline channel length path variation

a Channel 1 performance parameters

Channel parameter	**Value**
σ_τ	0.459 μs
μ_τ	0.134 μs
τ_A	0.09 μs
τ_{max}	0.52 μs
ACA	40 dB
B_{c50}	2.46 MHz

b Channel 2 performance parameters

Channel parameter	**Value**
σ_τ	0.514 μs
μ_τ	0.253 μs
τ_A	0.143 μs
τ_{max}	0.59 μs
ACA	45 dB
B_{c50}	2.41 MHz

c Channel 3 performance parameters

Channel parameter	**Value**
σ_τ	0.57 μs
μ_τ	0.317 μs
τ_A	0.184 μs
τ_{max}	0.685 μs
ACA	52 dB
B_{c50}	2.37 MHz

d Channel 3 performance parameters

Channel parameter	**Value**
σ_τ	0.6041 μs
μ_τ	0.385 μs
τ_A	0.209 μs
τ_{max}	0.762 μs
ACA	58 dB
B_{c50}	2.34 MHz

results that channel one outperforms all other channels. These results provide insight into the expected channel transfer characteristics of such channels for data transfer and communication applications. Shorter powerline channel path length should have better transfer characteristics compared to the longer powerline channel lengths.

4.7 SUMMARY

In this chapter, the characterisation of the unified powerline-wireless hybrid channel was presented. This chapter aimed to achieve the second objective of the research, that is, to characterise and analyse the channel transfer characteristics of a hybrid powerline-wireless channel, thereby determining the suitable modulation system for communication and information transfer purposes. The problem of a hybrid powerline-wireless channel was first addressed and the prevailing challenges of characterisation of such a channel. A sequence-based channel sounding method using maximum length sequences and software-defined radio was used to directly estimate the channel impulse response. The generated sequence is known at both the transmitter and receiver, by employing the principle of the sliding correlator at the receiver, time-domain measurements were performed to directly attain the channel impulse response of the powerline-wireless hybrid channel. The performance of the hybrid channel was analysed through average channel attenuation, coherence bandwidth and timing parameters such as RMS delay spread, mean delay spread and maximum delay spread. Channel attenuation was attained from the frequency response, timing delays were attained from the power delay profile of the channel and the coherence bandwidth from the spectral amplitude correlation at a threshold of 0.5. Based on the attained parameters, it was found that the hybrid channel is frequency selective. However, observation of the similarity in the fading profiles for the wireless to powerline channel transmission direction and powerline to wireless channel transmission direction suggests that the channel is symmetrical. This means the channel transfer characteristics are independent of the transmission direction. The effect of the powerline channel path length was investigated by decreasing the powerline length while keeping the wireless path constant and applying the sounding method. It was found that shorter powerline channel lengths showed improved channel transfer characteristics for the overall hybrid channel compared to longer powerline channel lengths.

CHAPTER 5 SIMO-OFDM HYBRID POWERLINE-WIRELESS SYSTEM PHYSICAL LAYER DESIGNS AND IMPLEMENTATIONS

5.1 CHAPTER OVERVIEW

The physical layer (PHY) of a communication system is a fundamental layer that defines the preparation of raw information for transmission over the channel and the processing of received analog signals to extract information. The PHY layer also defines the interface of the communication system to the channel. The design of a PHY layer requires observation and characterisation of the communication channel in order to ensure efficient and reliable communication between the transmitter and receiver. Key performance metrics of the channel such as coherence time, coherence bandwidth and Doppler frequency provide insight into the time variances and frequency selectivity nature of the communication channel. The design of a PHY layer for the hybrid powerline-wireless channel requires obtaining these performance metrics. Previous chapters highlighted the challenges faced in the hybrid channel such as multipath behaviour, noise characteristics and powerline channel losses. Performance analysis of the hybrid channel for single-carrier and multi-carrier modulation was presented in Chapter 3. The attained BER curves showed that multi-carrier is more suited for the hybrid channel and outperforms single-carrier modulation in a PLC environment with impulsive noise. Characterisation of the hybrid powerline-wireless channel in Chapter 4 provided insight into the channel transfer characteristics. Attained results include coherence bandwidth, average channel attenuation and timing delay parameters of the channel. These channel performance parameters highlighted that the PHY layer design for such a hybrid channel must be robust against channel interferences. Based on the work done in previous chapters, orthogonal frequency division multiplexing (OFDM) was chosen as the channel access method for reasons that will become apparent in the next sections of this chapter.

The use of OFDM for PLC channels has been the subject of several studies in literature [26, 83–88]. Optimisation of the conventional OFDM with rectangular pulses was investigated in [83], where pulse shaping was used at the transmitter and windowing at the receiver. The authors argued that the conventional OFDM with rectangular pulses results in reduced spectral containment. The side lobes of the sinc-shaped pulses result in low decay, which has a direct influence on both transmitter and receiver of real systems when distortion appears. The authors proposed that with proper roll-off design, deep frequency notches can be guaranteed at the PSD mask limits. In turn, using non-rectangular windowing at the receiver can reduce the effects of impulsive noise and inter-carrier interference (ICI). Adaptive cyclic prefix insertion and bit loading for PLC-OFDM systems were proposed in [85]. The convention of allocating a guard interval that is longer than the maximum channel dispersion time was found to be wasteful of spectral resources, especially for short powerline channel realisations. A cyclic prefix insertion algorithm was developed with the goal of optimising the channel capacity of the powerline channel. Some gains were attained from the cyclic prefix insertion method at the cost of transceiver complexity. However, these conclusions were based solely on simulation results. A chief drawback of OFDM is the high peak-to-average power ratio (PAPR), which translates into an inefficient use of power amplifiers in real systems. This issue was addressed in [86] through the performance analysis of vector OFDM (VOFDM) in PLC systems. The VOFDM scheme inherently has low PAPR and offers the flexibility of using single-carrier and multi-carrier modulation in the same system, and this comes at the cost of increased transceiver complexity as non-linear processing is required. Gains of at least 2 dB of VOFDM over conventional OFDM were attained, but the results are solely based on simulations. Selective mapping [89] and partial transmit sequencing [90] have been proposed for PLC -OFDM systems to tackle the high PAPR issue.

Previous works in literature have addressed the design and optimisation of OFDM for either PLC or wireless systems. To the best of the author's knowledge, there is no comprehensive design of OFDM for a hybrid powerline-wireless channel available in literature. Section 5.2 presents an overview of OFDM modulation and demodulation. Section 5.3 presents the design of the OFDM transmitter and receiver system for practical implementations. Design of the cyclic prefix duration and OFDM symbol duration in order to mitigate the effects of inter-carrier interference (ICI) and inter-symbol interference (ISI) caused by inherent interferences of the hybrid channel is presented. Proper design of these parameters mitigates carrier frequency offset (CFO) and symbol frequency offset (SFO), which in turn ensures orthogonality of sub-carriers and relaxes the channel estimation and synchronisation requirements at the receiver. Source encoding is crucial to ensure that the system is robust against noise interferences. Source encoding is achieved by forward error correction, data interleaving and cyclic redundancy checksum. Section 5.4 presents the design of selection combining, maximal ratio combining and equal gain combining methods used in the SIMO-OFDM hybrid powerline-wireless receiver. Software and hardware implementations of the SIMO-OFDM hybrid powerline-wireless system are presented in Section 5.5. Section 5.6 presents the signal coupling method used to interface the powerline channel to the wireless propagation environment.

5.2 OFDM OVERVIEW

OFDM is a multi-carrier transmission scheme that is used in communication systems to overcome the effects of frequency selectivity and time variances of a wideband channel. An OFDM system divides the wideband channel into N narrowband sub-channels each of which has sub-carrier frequencies f_k where $k = 0, 1, 2, \dots, N-1$. Therefore, the wideband frequency selective channel can be approximated by multiple frequency-flat narrowband sub-channels. OFDM is a more refined version of the filtered multi-tone (FMT) transmission scheme, unlike FMT where the wideband is fully divided into N narrowband sub-channels, the sub-carrier signals in OFDM overlap. The basic principle of multi-carrier schemes is to maintain orthogonality among sub-carrier signals, as long as orthogonality is maintained among sub-channels, ICI can be suppressed. Until 1971, a bank of oscillators tuned to the sub-carrier signals' frequencies was required at the transmitter for modulation and at the receiver for demodulation. Weinstein and Ebert [91] provided the first breakthrough of OFDM in 1971 when they used Discrete Fourier Transform (DFT) as a method to perform baseband modulation at the transmitter and demodulation at the receiver. DFT modulation and demodulation made OFDM more efficient and reduced the cost of OFDM implementation in practical systems. The second milestone in OFDM history came from Peled and Ruiz [92] when they introduced the cyclic prefix (CP) extension in 1980. Before the CP extension, the idea was to use empty guard spaces in the frequency domain to mitigate channel dispersion effects. Introducing a cyclic extension causes the channel to perform cyclic convolution with the transmitted signal, which in turn effectively maintains the orthogonality among sub-carriers under severe channel conditions. The principle of orthogonality is given by (5.1). Consider a time-limited signal $\{e^{j\omega_k t}\}_{k=0}^{N-1}$ representing the sub-carriers at frequencies $f_k = k/T_{sym}$ in an OFDM symbol, where $0 \leq t \leq T_{sym}$ and T_{sym} is the OFDM symbol period. The sub-carriers denoted by the complex exponential are orthogonal if the integral of their product is zero within a common period

$$\begin{aligned}\frac{1}{T_{sym}}\int_0^{T_{sym}} e^{j2\pi f_k t}e^{-j2\pi f_i t}dt &= \frac{1}{T_{sym}}\int_0^{T_{sym}} e^{j2\pi\frac{k}{T_{sym}}t}e^{-j2\pi\frac{i}{T_{sym}}t}dt \\ &= \frac{1}{T_{sym}}\int_0^{T_{sym}} e^{j2\pi\frac{(k-i)}{T_{sym}}t}dt \\ &= \begin{cases}1 & \forall k = i \in \mathbb{Z} \\ 0 & \text{otherwise}\end{cases}.\end{aligned} \tag{5.1}$$

5.2.1 OFDM modulation

An OFDM transmitter maps groups of bits to a QAM constellation to create symbols, the output data stream of the constellation mapper is then converted to N parallel stream data streams. This step in the transmitter is preceded by source encoding, usually being FEC. Each of the N complex-valued symbols from the serial-to-parallel (S/P) conversion is used to modulate a different sub-carrier. The S/P process extends the transmission time T_s for one symbol to NT_s for N symbols, which forms a single OFDM symbol with length T_{sym} given by $T_{sym} = NT_s$. If the lth transmit symbol that modulates the kth sub-carrier is denoted as $X_l[k]$ for $l = 0, 1, 2 \ldots, \infty$ and $k = 0, 1, 2, \cdots, N-1$, then the passband OFDM signals in continuous-time can be expressed as

$$x_l(t) = \mathbb{R}\left\{\frac{1}{T_{sym}}\sum_{l=0}^{\infty}\left\{\sum_{k=0}^{N-1} X_l[k]\,\varphi_{l,k}(t)\right\}\right\}, \tag{5.2}$$

where $\varphi_{l,k}\left(t\right)$ represents the OFDM symbol at the kth frequency given as

$$\varphi_{l,k} = \begin{cases} e^{j2\pi f_k (t - lT_{sym})} & 0 \leq t \leq T_{sym} \\ 0 & \text{elsewhere} \end{cases}. \tag{5.3}$$

The corresponding discrete-time OFDM signal can be produced by sampling the continuous-time signal at $t = lT_{sym} + nT_s$ where $T_s = T_{sym}/N$. The discrete-time signal is given as

$$x_l\left[n\right] = \sum_{k=0}^{N-1} X_l\left[k\right] e^{j\frac{2\pi kn}{N}}, \quad n = 0, 1, 2, ..., N-1. \tag{5.4}$$

A close observation of (5.4) reveals that it is an N-point IDFT of the QAM constellation mapping output symbols $\{X_l\left[k\right]\}_{k=0}^{N-1}$. As a result, an N-point IDFT can be used to generate the OFDM signal. This was the precise breakthrough made by Weinstein and Ebert. The IDFT can be efficiently implemented by using the Fast Fourier Transform (FFT) algorithm. For an N-point IDFT process the number of computations is given by N^2, the FFT algorithm exploits the symmetrical properties of the IDFT process and reduces the computational complexity to $N \log N$. The discrete-time OFDM signals produced contains real and imaginary components which are sent to a DAC to create the analog waveforms. The analog OFDM signal is then passed to an RF modulator to produce an analog passband signal that is transmitted through the channel, real and imaginary components of the OFDM signal are transmitted using overlapping frequency bands because the RF waveforms are orthogonal to each other.

5.2.2 OFDM demodulation

The OFDM signal received can be reconstructed back to the originally transmitted signal by using the orthogonality among sub-carriers. Consider the received continuous-time signal given as

$$y_l = \sum_{k=0}^{N-1} X_l\left[k\right] e^{j2\pi f_k (t - lT_{sym})}, \tag{5.5}$$

where $lT_{sym} < t < lT_{sym} + nT_{sym}$. Assuming that the orthogonality among sub-carriers is maintained, the transmitted signal can be reconstructed from the received signal as

$$\begin{aligned} Y_l[k] &= \frac{1}{T_{sym}} \int_{-\infty}^{\infty} y_l(t)\, e^{j2\pi k f_k (t - lT_{sym})} dt && (5.6) \\ &= \frac{1}{T_{sym}} \int_{-\infty}^{\infty} \left\{ \sum_{i=0}^{N-1} X_l[i]\, e^{j2\pi f_i (t - lT_{sym})} \right\} e^{-j2\pi f_k (t - lT_{sym})} dt && (5.7) \\ &= \sum_{i=0}^{N-1} X_l[i] \left\{ \frac{1}{T_{sym}} \int_{0}^{T_{sym}} e^{j2\pi (f_i - f_k)(t - lT_{sym})} \right\} && (5.8) \\ &= X_l[k]. && (5.9) \end{aligned}$$

The corresponding discrete-time of the reconstruction process is carried out by sampling the received continuous-time signal at $t = lT_{sym} + nT_{sym}$ and replacing the integral signs with summations as

$$\begin{aligned} Y_l[k] &= \sum_{n=0}^{N-1} y_l[n]\, e^{-\frac{j2\pi kn}{N}} && (5.10) \\ &= \sum_{i=0}^{N-1} \left\{ \frac{1}{N} \sum_{i=0}^{N-1} X_l[i]\, e^{\frac{j2\pi in}{N}} \right\} && (5.11) \\ &= \frac{1}{N} \sum_{n=0}^{N-1} \sum_{i=0}^{N-1} X_l[i]\, e^{\frac{j2\pi (i-k)n}{N}} && (5.12) \\ &= X_l[k]. && (5.13) \end{aligned}$$

Similar to (5.4), a closer look at (5.11) reveals that the reconstruction process is the DFT process of the received signal samples $\{y_l[n]\}_{n=0}^{N-1}$. The OFDM demodulation DFT process can be efficiently implemented using the FFT algorithm. The use of the FFT and IFFT to generate the OFDM symbols and demodulation the received signal is more efficient if the number of sub-carriers is large, $N > 30$, which was appropriate for the developed system with an FFT size of 64.

5.3 OFDM SYSTEM

OFDM transmitter and receiver structures are given in Fig. 5.1 and Fig. 5.2 respectively. Source encoding of the information is composed of an interleaver, convolutional encoder and a cyclic redundancy check code (CRC). Source encoding ensures that the transmitter is robust against the hybrid channel interferences. The encoded information bits are repacked into 2-bits and mapped to a 4-QAM constellation using Gray encoding to reduce symbol detection errors by ensuring that the minimum Hamming distance between adjacent symbols is one. The serial stream is then converted to parallel streams of length $N = 64$, which is the FFT size. The time-domain OFDM symbols are then created by the 64 point IFFT process. In order to protect the successive OFDM symbols against ISI and the transmitted signals against ICI, a cyclic prefix is added to each OFDM symbol. The CP is a copy of N_G samples from the tail of the symbol that is then prepended to each OFDM symbol. The CP extends the symbol by N_G, resulting in a total symbol length of $N_G + N_{sym}$. Proper design of the CP length is crucial to the system performance and to keep receiver complexity low. Passband modulation is then performed by analog front-end modulation of I/Q samples using an SDR.

The SDR analog front-end performs passband demodulation and sampling of received I/Q samples. The CP is removed to obtain the OFDM frame. Data from the OFDM frame preamble is then used to perform synchronisation in two parts. Timing synchronisation to correct STO and frequency synchronisation to correct CFO. Serial-to-parallel conversion is performed and, FFT demodulation is then performed on the OFDM symbols to attain frequency information of each carrier. Data from the OFDM frame header is then used to perform channel estimation using a Least-Squares estimator. One-tap frequency equalisation is then applied to each sub-carrier to mitigate the channel effects. Parallel streams of information are then converted to a serial stream and de-mapped using maximum likelihood detection. Using the de-mapped information bits, a CRC frame check is used to validate the OFDM frame, the bits are de-interleaved and then decoded using a Viterbi algorithm to obtain the transmitted information.

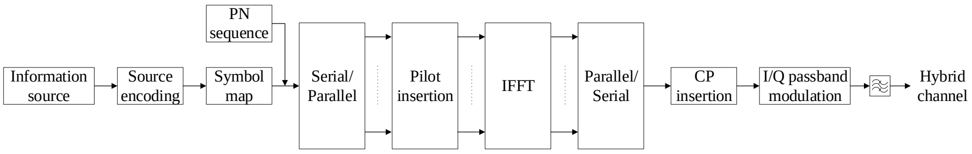

Figure 5.1. OFDM transmitter

5.3.1 OFDM symbol

Frequency selective behaviour of the hybrid channel is characterised by the coherence bandwidth BW_{ch} and maximum delay spread τ_{max}. These parameters are estimated from the PDP of the channel. These channel parameters govern the design of the CP length. The bandwidth

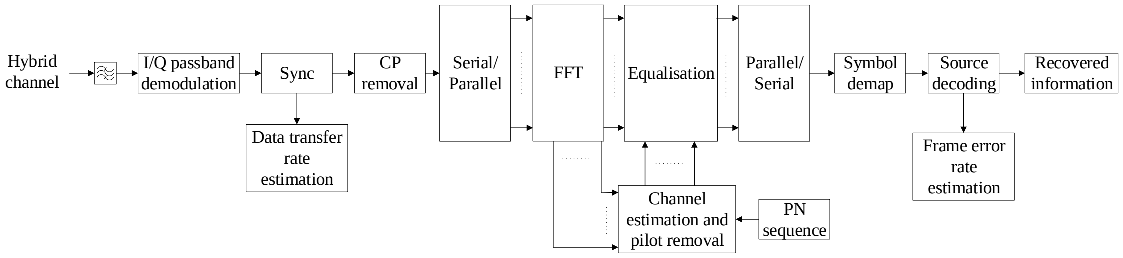

Figure 5.2. OFDM receiver

occupied by the narrowband sub-channels is denoted by Δf_{sc}. Δf_{sc} can also be considered to be the sub-carrier separation. In order to maintain the frequency-flat transmission characteristics of the OFDM sub-carriers, it is required that the sub-carrier bandwidth be much smaller than that of the channel coherence bandwidth, that is $\Delta f_{sc} << BW_{ch}$ where BW_{ch} is the channel coherence bandwidth. This condition simplifies OFDM equalisation at the receiver. The relationship between the OFDM symbol T_{sym} and Δf_{sc} is given by (5.14)

$$T_{sym} = \frac{1}{\Delta f_{sc}}. \tag{5.14}$$

Therefore, in order to maintain the frequency-flat transmission of the sub-carriers, the OFDM symbol period must much larger than τ_{max}, that is $T_{sym} >> \tau_{max}$. A CP is then placed at the head of an OFDM symbol. In order to mitigate interference from signal echoes that result from the multipath propagation behaviour of the channel, the CP length should be longer than or be equal to the maximum delay of the multipath channel, which means $T_G \geq \tau_{max}$. It can be noted that including a CP reduces the bandwidth efficiency of the system. The bandwidth efficiency can be evaluated as

$$\eta_{BW} = \frac{N_{sc-mod}}{N_{sc}+N_G} \cdot \frac{\log M}{BW}, \tag{5.15}$$

where η_{BW} is a unit-less metric that gives the bandwidth efficiency of the channel, N_{sc-mod} and N_{sc} the number of the modulated sub-carriers and total sub-carriers. The number of guard interval samples is denoted by N_G. The total available bandwidth is denoted by BW and M is the size of the QAM constellation. Because the number of total sub-carriers is likely to exceed that of modulated sub-carriers, the relation between the actual modulated bandwidth and the total available bandwidth is given by the unit-less metric ξ_{BW}.

$$\xi_{BW} = \frac{N_{sc-mod}\Delta f_{sc}}{BW}. \tag{5.16}$$

The bandwidth efficiency metric can be rewritten in terms of ξ_{BW} as

$$\eta_{BW} = \frac{\xi_{BW}}{1+\zeta_f} \cdot \log M, \tag{5.17}$$

where ζ_f is given as $\zeta_f = N_G \; N_{sc}$. The ξ_{BW} parameter provides an indication of the complexity of the receiver. High-performance systems have ξ_{BW} close one to such the DVB-T with $\xi_{BW} = 0.95$, while low-performance system has a small ξ_{BW} such as the HiperLAN2 with $\xi_{BW} = 0.8125$. Due to the spectral inefficiency introduced by the CP, the value of ζ_f should be kept as low as possible. The high spectral efficiency of the OFDM system in the dispersive hybrid channel is guaranteed by $T_G = \tau_{max}$. This design criterion guarantees an efficient system assuming that there are no channel variations in the OFDM symbol period. Consequently, the OFDM symbol period for an efficient system is given as

$$T_{sym} = \frac{\tau_{max}}{\zeta_f}, \tag{5.18}$$

where $\zeta_f \leq 0.25$, this upper boundary ensures that $T_{sym} >> \tau_{max}$, hence frequency-flat transmission of the sub-carriers. A trade-off between ξ_{BW} and ζ_f is required to achieve the requirement of high spectral efficiency. Spectral efficiency is defined as

$$\eta_f = \frac{\xi_{BW}}{1+\zeta_f}. \tag{5.19}$$

The value of η_f should be kept as close as possible to one. This is achieved by keeping ξ_{BW} as close as possible to one and keeping ζ_f as low as possible with an upper boundary of 0.25. The value of ξ_{BW} is motivated by the need to keep the implementation cost of the system low while also aiming to achieve acceptable system performance. A value of 0.8 was observed to be a good trade-off of these requirements. The value of ζ_f is somewhat controversial to the condition of high spectral efficiency. However, given the nature noise interference of the powerline channel, slight variations of the maximum delay τ_{max} can be expected. In favour of mitigating ICI and ISI in such cases, the spectral efficiency requirements are relaxed. The

OFDM symbol period is given as

$$\begin{aligned} T_{sym} &= \frac{\tau_{max}}{\zeta_f}, & (5.20) \\ &= \frac{0.8\ \mu s}{0.2} = 4\ \mu s. & (5.21) \end{aligned}$$

The available bandwidth for the OFDM system was chosen as 20 MHz. Rearranging (5.16), the number of modulated sub-carriers is given by

$$\begin{aligned} N_{sc-mod} &= \xi_{BW} \cdot BW \cdot T_{sym}, & (5.22) \\ &= 0.8 \left(20 \times 10^{6}\right) \left(4 \times 10^{-6}\right) = 64. & (5.23) \end{aligned}$$

A suitable FFT and IFFT size of 64 is then used for OFDM modulation and demodulation. The FFT and IFFT processes are implemented using the radix-2 algorithm. Relaxing the spectral efficiency requirements in favour of low receiver complexity requires that $T_G > \tau_{max}$ instead of $T_G = \tau_{max}$. As such $T_G = 1\ \mu s$ and $\zeta_f = 0.25$. With these settings, the number of CP samples is given by

$$\begin{aligned} N_G &= \zeta_f N_{sc}, & (5.24) \\ &= 0.25 \times 64 = 16. & (5.25) \end{aligned}$$

Including a CP makes the symbol appear periodic to the channel. Therefore the inclusion of CP causes the periodic OFDM symbols to be circularly convolved with the channel. The circular convolution in the time domain equates to the multiplication of the signal and the respective channel DFTs as described by (5.26). This result is crucial as it reduces the complexity and computational burden in channel equalisation.

$$\begin{aligned} y_l\left[n\right] &= x_l\left[n\right] \otimes h_l\left[n\right], & (5.26) \\ DFT\left\{y_l\left[n\right]\right\} &= DFT\left\{x_l\left[n\right]\right\} \otimes DFT\left\{h_l\left[n\right]\right\}, & (5.27) \\ Y_l\left[n\right] &= X_l\left[n\right] \otimes H_l\left[n\right]. & (5.28) \end{aligned}$$

5.3.2 Source encoding and decoding

Source encoding is used to detect and correct errors caused by channel impairments on the transmitted information-carrying signal. Given the nature of the hybrid channel, random errors and burst errors can be expected. Random errors refer to changes of single bits in a codeword. Burst errors result when two or more bits in a codeword are changed, the affected bits in a codeword are not necessarily consecutive. The length of a burst error L is measured from the first corrupted bit to the last corrupted bit in a codeword. In a powerline channel, errors are more likely to occur in bursts. This is because impulsive noise is the most detrimental noise type in a powerline channel. It occurs in narrow-band bursts and has the highest PSD, which causes bursts errors. Impulsive noise PSD can reach values as high as 50 dB above background noise with the impulse width lasting from a few microseconds to a few milliseconds. Data interleaving is used to rearrange the source encoded bits without adding redundancy and omission of information bits in efforts to combat burst errors. A Convolutional encoder and a Viterbi decoder are used to effectively detect and correct random errors. Data interleaving is used to spread out errors to make them appear random so that the decoder can correct them.

5.3.2.1 Data interleaving

A basic block interleaver was considered for the implemented system. The interleaver uses a matrix with dimensions $M \times N = L$. L is a one-dimensional stream of information bits of length L that populates the interleaver matrix row-by-row. An output of length L is read out column-by-column before undergoing further processing in the transmitter. At the receiver, the received codewords undergo de-interleaving before they are decoded. A burst interval of length L or less will cause multiple bit errors in a codeword, however single errors in the burst interval are more likely to be corrected by the decoder than the entire burst error. The parameter L is the interleaver depth, it is chosen based on the worst channel conditions, and it must be large enough so that the interleaved codeword can handle the largest burst error interval expected. The pitfall of block interleaving is a delay that is introduced by the row-by-row population of the interleaver matrix. Consider an interleaver with $L = 9$, $M = 3$, and $N = 3$, the input vector is $\mathbf{x}$ and the interleaver matrix is $\mathbf{y}$, operation of a block interleaver can be expressed as

$$x = \begin{bmatrix} x_0 & x_1 & x_2 & x_3 & x_4 & x_5 & x_6 & x_7 & x_8 \end{bmatrix}, \tag{5.29}$$

$$y = \begin{bmatrix} x_0 & x_1 & x_2 \\ x_3 & x_4 & x_5 \\ x_6 & x_7 & x_8 \end{bmatrix}, \tag{5.30}$$

$$T_X = \begin{bmatrix} x_0 & x_3 & x_6 & x_1 & x_4 & x_7 & x_2 & x_5 & x_8 \end{bmatrix}, \tag{5.31}$$

$$R_X = \begin{bmatrix} x_0 & x_3 & x_6 & x_1 & x_4 & x_7 & x_2 & x_5 & x_8 \end{bmatrix}, \tag{5.32}$$

$$\widetilde{y} = \begin{bmatrix} x_0 & x_3 & x_6 \\ x_1 & x_4 & x_7 \\ x_2 & x_5 & x_8 \end{bmatrix}, \tag{5.33}$$

$$\widetilde{x} = \begin{bmatrix} x_0 & x_1 & x_2 & x_3 & x_4 & x_5 & x_6 & x_7 & x_8 \end{bmatrix}, \tag{5.34}$$

A one-dimensional vector is read into an array of length L. Once the array is equal to L, then the matrix is populated row-by-row, after ensuring that all rows are populated, the information is then transmitted using the randomised order. De-interleaving the received information bits follows the same procedure and the order of information bits is recovered. Data interleaving parameters are $M = 96$, $N = 8$ and $L = 768$. The interleaver depth is large enough to handle burst errors in the hybrid channel. The matrix dimensions were chosen to ensure that an input byte, that is 8-bits, can be readily read in column-by-column, this mitigates potential errors due to bit tracking during the de-interleaving. The de-interleaver process at the receiver follows the same procedure to make burst errors appear as random errors for the FEC decoder.

5.3.2.2 Convolutional Encoder and Decoder

Encoding is used to add redundancy to the transmitted information. Redundancy is important for error detection and correction. A convolutional encoder is used for encoding. Convolutional codes are more attractive than their block code counterparts because they can be devised to correct either single-bit errors, burst errors or both. The FEC convolutional encoder is characterised by three parameters k, n and L. k is the number of input bits, n is the number of output bits and L is the encoder constraint length. When a message sequence with k bits is input to the encoder, a redundancy of $m = n - k$ will be added to the output message sequence. The ratio of k to n is the encoder rate R given as

$$R = \frac{k}{n}. \tag{5.35}$$

The encoder output does not only depend on the current k input bits but also on the $L-1$ input bits. The constraint length L represents the memory of the encoder, and it is the number of stages that an input bit can influence the output. The encoder can be represented by a finite state machine (FSM) with 2^{L-1} states. The FSM infers the encoder memory. The states represent all possible $L-1$ previous bit combinations and the state transitions represent all possible encoder outputs for all possible encoder inputs. In practice, an encoder consists of a shift register of length L and n modulo-2 adders. Generator polynomials are used to represent the feedback positions on the shift register array, which are fed into the modulo-2 adders to produce the output bits.

The convolutional encoder was implemented with a constraint length of $L = 7$. The encoder state machine has a total of $2^{7-1} = 64$ states. The input is one bit, and the output is two bits, thus a coding rate of $R = 1/2$. The encoder polynomials for the encoder output are given as $g_A = 133_8 = 1011011$ and $g_B = 171_8 = 1111001$. The polynomials define feed positions from the shift register to modulo-2 adders to generate each of the two output bits as shown in Fig. 5.3.

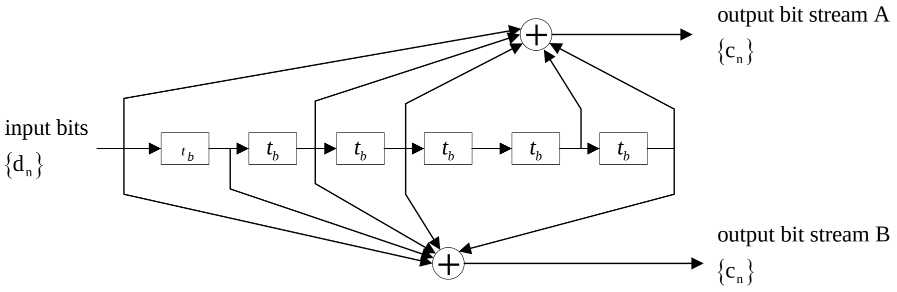

Figure 5.3. Convolutional encoder structure

The FEC decoder was implemented using the Viterbi algorithm. The decoding procedure is facilitated by making use of a trellis structure for the encoder FSM. Considering the FSM state transitions, the correct codeword is obtained by tracking the most likely path through the trellis structure, starting from the default state to the end of the received codeword. Traversing horizontally through the trellis structure represents the time steps, while traversing vertically represents the state transitions. The algorithm determines the most likely codeword using two metrics, namely, branch metric (BM) and path metric (PM). The BM is the Hamming distance between the received codeword when in a particular state and the expected codeword in that particular state. When transitioning from one state to another, there is a maximum of two paths from two states. PM represents the smallest BM when transitioning from one state to another, which is the smallest Hamming distance when transitioning from one state to another. The decoder uses hard decision, and this means that the Hamming distance between the received codeword and the complement of the codeword is the maximum possible BM.

The decoder process shown in Fig. 5.4 has four main functions defined as BM, ACS, Memory and Propagation. The BM function computes the Hamming distance between the received codeword and the expected codeword using modular-2 addition of two bits at a time, this is because a state can only be reached by two paths. The number of ones from the resulting codeword is checked which is the Hamming distance, and this is iterated through all 64 states. The ACS function is used to compute the PM. A state can only be reached by two paths, this means two PMs are calculated for each state. A PM of a state is obtained by the addition of the PM from the previous state and a BM of the current state. The calculated two PMs are compared, and the least PM is stored in memory as the surviving path.

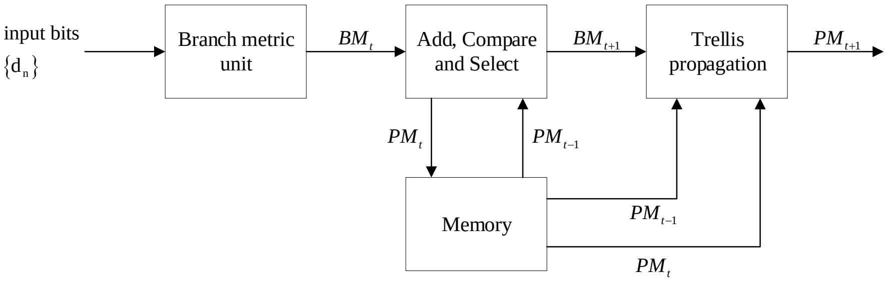

Figure 5.4. Convolutional decoder structure

This process for each state can be summarised by the butterfly diagram in Fig. 5.5. The PMs in state a and b are given by PM_t^a and PM_t^b. Transitioning to states c and d is achieved adding BMs of states c and d, denoted by BM_{t+1}^c and BM_{t+1}^d, to PMs of states a and b, which then equals to PMs of states c and d denoted PM_{t+1}^c and PM_{t+1}^d. The surviving paths for states the c and d are then determined by selecting the minimum between PM_{t+1}^c and PM_{t+1}^d.

This procedure is expressed by (5.36) through (5.41).

$$
\begin{aligned}
PM_{t+1}^{c} &= PM_{t}^{a} + BM_{t+1}^{a,c}, && (5.36)\\
PM_{t+1}^{c} &= PM_{t}^{b} + BM_{t+1}^{b,c}, && (5.37)\\
PM_{t+1}^{d} &= PM_{t}^{a} + BM_{t+1}^{a,d}, && (5.38)\\
PM_{t+1}^{d} &= PM_{t}^{b} + BM_{t+1}^{b,d}, && (5.39)\\
PM_{t+1}^{c} &= \min\left[\left(PM_{t}^{a} + BM_{t+1}^{a,c}\right), \left(PM_{t}^{b} + BM_{t+1}^{b,c}\right)\right], && (5.40)\\
PM_{t+1}^{d} &= \min\left[\left(PM_{t}^{a} + BM_{t+1}^{a,d}\right), \left(PM_{t}^{b} + BM_{t+1}^{b,d}\right)\right]. && (5.41)
\end{aligned}
$$

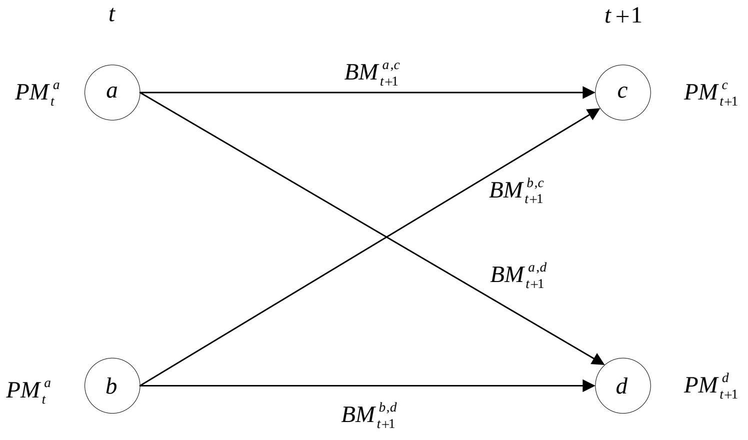

Figure 5.5. Trellis decoding structure

The PM surviving paths given by (5.40) and (5.41) are stored by the memory function and returned to the ACS function to calculate the PMs for the next states. This process is iterated through all 64 states to find all the PM surviving paths for all the states. Once the last PM surviving path is found, the propagation function then backtraces all of the surviving paths that caused transitions from the 64th state to the first state. The recovered codeword is the two-bit outputs of all states of all surviving paths at each time step in the trellis diagram.

5.3.2.3 CRC32 frame check

Information is transmitted and received in OFDM frames. The validity of the OFDM frames needs to be checked at the receiver to detect corrupted frames. A sequence of redundant bits called cyclic redundancy check (CRC) bits are prepended to form a header of the frame so that the resulting frame becomes precisely divisible by the CRC value. At the receiver, long division is performed on the received frame by the same predetermined CRC value, if there is no remainder the received frame is assumed to be correct, else if there is a remainder the frame assumed to be corrupted, it is then rejected, and the frame error rate (FER) incremented accordingly.

A generator polynomial describes the CRC operation. If a k-bit frame is to be transmitted, an r-bit Frame Check Sequence (FCS) is generated by performing long division on the k-bit frame prepended by r zeros of the generator polynomial. The remainder is the r-bit FCS prepended to the OFDM frame such that the resulting frame is $k+r$ bits long. The generator polynomial divisor is a binary value that is $r+1$ bits long and results from setting the polynomial coefficients to 1s and 0s. Setting the polynomial coefficients to 1s and 0s allows for modulo-2 arithmetic to be used for the long division. The generator polynomial used is given as

$$CRC32 = x^{32}+x^{26}+x^{23}+x^{22}+x^{16}+x^{12}+x^{11}+x^{10}+x^{8}+x^{7}+x^{5}+x^{4}+x^{2}+1, \quad (5.42)$$

by setting the polynomial coefficients to 1s and 0s the binary value used for modulo-2 operation is $CRC32_{binary} = 111011011011100010000011001000001$. The division occurs until the dividend is equal to zero, if not, the previous dividend with the CRC32 devisor is realigned such that its first index becomes the first 1, which is then divided by the CRC32 devisor. Once the dividend is equal to zero, the 32-bit remainder is retrieved and is then prepended to the OFDM frame. Due to this process, the checksum prepended output vector is 4 bytes larger than the input vector.

5.3.3 Synchronisation

Data aided synchronisation is used to correct time and frequency offsets between the transmitter and receiver. An additional PN sequence is transmitted to form the preamble of the OFDM frame. Time and frequency synchronisation are then achieved by correlation methods with the same sequence known a priori at the receiver. This method was first proposed by Schmidl and Cox [93]. Since then, there have been numerous works on the application of PN sequence synchronisation in OFDM systems. The PN sequence structure has two matching halves of the sequence in the time-domain. The sequence halves are allocated to even-numbered sub-carriers and nothing on odd-numbered sub-carriers, that is, $T_{PN\ sym}$ is the PN sequence with carrier allocation such that $T_{PN\ sym} = T_{PN\ sym}(k + N_{sc}/2)$, where k in the sub-carrier index and N_{sc} is the total number of sub-carriers for an OFDM symbol.

The received PN sequence is separated into two halves to perform timing and frequency synchronisation. Firstly, timing synchronisation is performed to identify the start of an OFDM frame. The signal energy of the OFDM frame is observed to identify the nulls of the PN sequence where the signal is zero. The nulls are identified by applying an FIR-filter to calculate the moving sum of a length of $T_{PN\ null} = 32$, this is because an FFT size of 64 is used and half of it is the PN sequence nulls. The output of the FIR filter is expressed as

$$y\left(n\right) = \sum_{k=0}^{T_{null}-1} x\left(n-k\right), \tag{5.43}$$

the output $y[n]$ is then multiplied with -1 and is input to a peak detector. A predefined threshold of the peak detector is used to identify the start of an OFDM frame if the threshold is exceeded. Once a frame is detected, the process is carried out iteratively when the signal energy is below the threshold to search for a maximum.

The second part of synchronisation is to estimate and correct carrier frequency offsets. Frequency synchronisation can be performed in two parts, fine frequency synchronisation and coarse frequency synchronisation. The former is for frequency offsets that are smaller than sub-carrier spacing and the latter is for frequency offsets that are larger than the sub-carrier spacing. The carrier frequency mismatch causes a phase offset that can be quantified by $\varphi = \pi T_s \Delta f$, where Δf is the CFO and T_s is the sampling period. For a received PN sequence, the phase offset is attained by multiplying the first half of the sequence with the conjugate of the second half. The CFO Δf is estimated by multiplying the first half with the second half as

$$P\left(d\right) = \sum_{k=0}^{N_{sc}-1} x_i\left(k+d\right) x_i\left(k + d + {}^{N_{sc}}/_{2}\right), \tag{5.44}$$

where k is the sub-carrier index and d the begging of an OFDM symbol, which is the portion of the cyclic prefix unaffected by inter-symbol interference. $P\left(d\right)$ is the summation of terms with similar phase offsets. An optimal starting point for an OFDM symbol is obtained by searching for the maximum of $P\left(d\right)$. The summation of phase offsets is normalised by the energy of the second half of the sequence to define the value of d as

$$R\left(d\right) = \sum_{k=0}^{N-1} \left| x_i(k+d+N/2\ )^2 \right|, \tag{5.45}$$

the metric $\frac{P(d)}{R(d)}$ is then maximised by the optimal value of d. The phase difference is then estimated by the phase of the conjugate of $P\left(d\right)$, that is $\varphi = \angle P\left(d^*\right)$. The frequency offset is then estimated as

$$\Delta f = \frac{\angle P\left(d^*\right)}{\pi T_{sym}}. \tag{5.46}$$

The phase offset φ causes the received signal to rotate about the origin, as such CFO can be eliminated by multiplying an entire frame by $e^{-j\Delta f} = e^{-\frac{\angle P(d^*)}{\pi T_{sym}}}$, which is equivalent to rotating the constellation points in the opposite direction to the CFO phase error. The phase error offsets are limited to $[-\pi, \pi]$. Larger values of φ cause phase ambiguity, in such cases, the receiver complexity and computational cost required to correct the CFO quickly rises.

5.3.4 Channel estimation and equalisation

Information aided channel estimation is achieved by a training PN sequence and pilot symbols in the transmitted OFDM symbols. In order to capture the channel transfer characteristics, pilot insertion in the frequency domain must obey the following equation

$$D_p \leq \frac{1}{\tau_{\max} \Delta f_{sc}}, \tag{5.47}$$

where D_p is the spacing between pilot symbols in the frequency domain, $\tau_{\max}$ is the maximum channel delay spread and Δf_{sc} the sub-carrier spacing. By obeying (5.47) effects of the hybrid channel can be estimated from the received pilot samples. If (5.47) is not fulfilled, channel estimation introduces an ambiguity in the equalisation weights of the estimated channel impulse response. Pilot symbols are inserted at index locations $k \in \{-27, -7, 7, 27\}$ with respective weights of $x \in \{1, 1, -1, 1\}$. These four pilot symbols are transmitted continuously with every OFDM symbol and are known at both the transmitter and receiver.

Fine channel estimation is achieved by sending additional data with the OFDM symbols to form the header of the information received. This additional information is also a PN sequence consisting of ±1 which is known at both the transmitter and the receiver. Channel state information is then estimated by comparing the received PN sequence to the known PN sequence. A simple one-tap equaliser block is then used to mitigate the channel effects. The equalised symbols are then fed to a maximum likelihood decision to detect the correct symbols from the symbols' estimates.

The PN sequence is placed at the head of an OFDM frame. A received OFDM frame consists of a preamble PN sequence used for synchronisation, a header PN sequence used for channel estimation and OFDM symbols. Similar to synchronisation, channel estimation is performed for one OFDM frame at a time, and channel effects are mitigated by equalisation for all OFDM symbols within the particular frame. Carrier allocation for OFDM symbols has a total of 64 sub-carriers. Carrier allocation for the PN sequence for channel estimation has 0s for the first and last 12 sub-carriers, the middle 40 sub-carriers are allocated ±1 to even-numbered sub-carriers and 0s for odd-numbered sub-carriers. After detection of the start of the OFDM frame by synchronisation, the received PN sequence in the ith OFDM frame is given as

$$R_i\left(k+d\right) = C_i\left(k\right) \times H_i\left(k\right) \times e^{\frac{2\pi d N_G}{N_{fft}}} + N_i(k), \quad k = 1, 2, ..., N_{sc}, \tag{5.48}$$

where d is the start of the OFDM frame, k is the sub-carrier index, N_G and N_{fft} denote the length of the CP and the FFT size, respectively. $C_i\left(k\right)$ denotes the kth symbol of the PN sequence known a priori at the receiver, $H_i\left(k\right)$ is the estimated channel coefficients and $N_i(k)$ denotes the noise component. The Least-Squares (LS) estimates method is used to attain the channel coefficients. The LS method was chosen because of the easy implementation and the need to keep the receiver complexity as low as possible. The received PN sequence at the output of the FFT process block is fed into the channel estimator, channel coefficients for the ith OFDM frame are given as

$$H_{LS}\left(k\right) = \frac{R_i\left(k+d\right)}{C_i\left(k\right)} \cdot e^{-\frac{2\pi d N_G N_{sym}}{N_{fft}}} \tag{5.49}$$

where N_{sym} denotes the number of OFDM symbols in the OFDM frame. The PN sequence sub-carrier allocation is ±1 for even numbered sub-carriers and 0s for odd-numbered sub-carriers. Therefore the channel coefficients for the odd-numbered sub-carriers must be interpolated for the remaining half of the sub-carrier indexes. For the sake of simplicity of the receiver, linear interpolation was used for channel coefficients as

$$H_{LS}(2k+1) = H_{LS}(2k) + H_{LS}(2k+2). \tag{5.50}$$

One tap equalisation is then applied to the OFDM symbols after FFT demodulation. Equalisation is followed by maximum likelihood detection of the complex constellation symbols. The correct constellation symbol is detected by calculating the minimum Hamming distance between the received symbol with all possible constellation symbols. The symbol with the smallest Hamming distance is assumed to be correct. The constellation points are Gray encoded to ensure that the minimum Hamming distance between adjacent symbols is one, thereby reducing detection errors and the detector computational cost. Detected symbols are then fed to the QPSK constellation decoder and information bits are obtained for further source decoding.

5.3.5 Sub-carrier allocation

The FFT and IFFT processes facilitate the generation of the OFDM signal at the transmitter and the extraction of the OFDM transmit symbols from the received signal based on the orthogonality principle outlined by (5.2). An FFT size 64 is used for modulation and demodulation. As such, the total number of sub-carriers within an OFDM symbol is 64, 48 of the sub-carriers are allocated to carry information and 4 of the 64 sub-carriers are used as pilot symbols. The FFT carrier allocation structure for OFDM symbols is shown in Fig. 5.6. The 64-point FFT maps the coefficients 1 to 26 to the same numbered FFT indexes, and the coefficients -26 to -1 are translated to 38 to 63 FFT indexes, the rest of the indexes in the range 27 to 37 are unallocated and the zeroth index is unallocated.

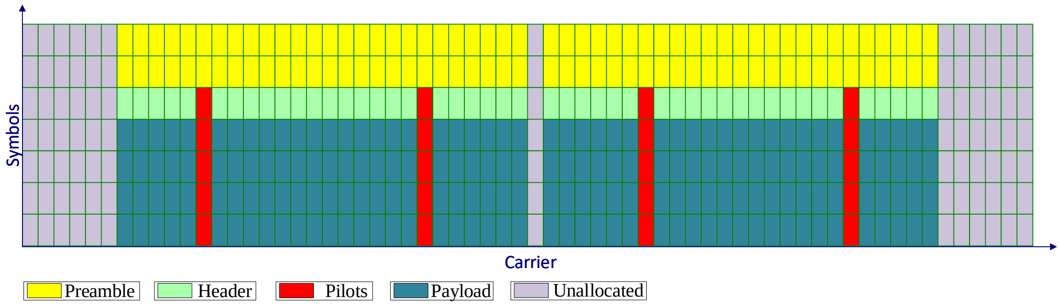

Figure 5.6. FFT carrier allocation for OFDM symbols

5.3.6 Data rate and error rate

The OFDM system performance metrics are date transfer rate and error rate. The data rate is representative of the amount of information that is successfully transmitted and received through the channel, which can also be called system throughput. The error rate is an indication of how robust the system is against the hybrid channel interferences. The error rate is given in terms of frame-error-rate (FER) instead of bit-error-rate (BER).

5.3.6.1 Data rate

The bit rate of an OFDM system, in theory, is given by

$$R_b = \frac{N_{sc-mod}\log_2 M}{T_{sc}}, \tag{5.51}$$

where N_{sc} denotes the number of occupied carriers in an OFDM symbol, M is the constellation size and T_{sc} denotes the time-domain spacing of sub-carriers. T_{sc} can also be defined in terms of the signal transmission bandwidth BW as $T_c = BW/\Delta f_{sc}$, where Δf_{sc} is the sub-carrier spacing. Equation 5.51 assumes that there is no redundancy added to the OFDM symbols. Practical OFDM systems have redundant information transmitted with the payload to aid in synchronisation, channel estimation and payload information validation. FEC encoding also adds redundant parity check bits used to detect and correct transmission errors. The actual value of (5.51) will be smaller for a practical OFDM system. The data rate metric is revised with consideration of redundant information and is given as

$$R_b = \frac{N_{sc}\log_2 M}{T_{sc}} \cdot \alpha_{sync} \cdot \alpha_{CP} \cdot \alpha_{CRC-32} \cdot \alpha_{sync} \cdot \alpha_{parity}. \tag{5.52}$$

where the fractional components α denote the redundancy added. Equation 5.52 gives the effective data transfer rate of the OFDM system in a practical sense. It shows that the actual payload makes up a small fraction of the transmitted information, as such bandwidth efficiency is traded for the extra overhead that is required by the system to have a reliable communication link.

The data rate in kbps is estimated by the procedure given by the flow diagram shown in Fig. 5.7. A large enough window size is defined for multiple OFDM frames, sampling rate and the synchronisation triggers given when a frame is detected using the Schmidl and Cox

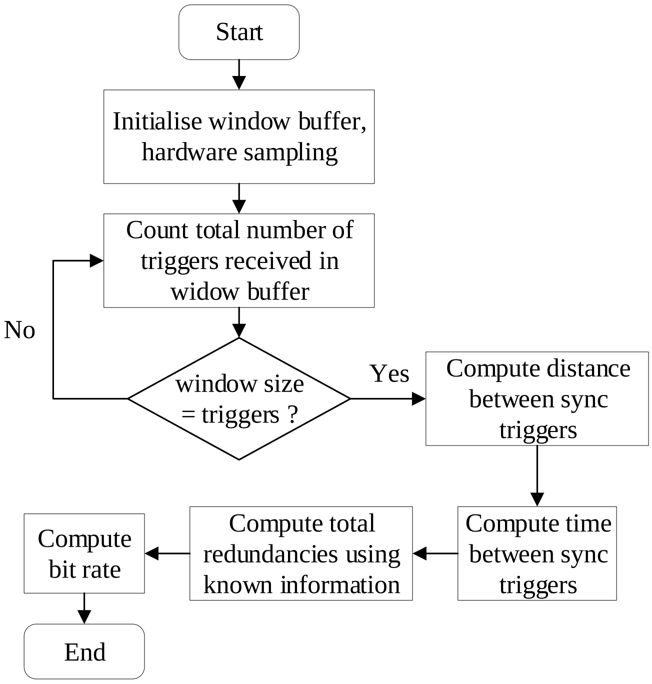

Figure 5.7. Data rate estimation flow diagram

method are also inputs to the estimator. For the defined window size, the number of triggers indicating successful frames are stored. The average distance between triggers is computed, which represents the duration of OFDM frames in the window size, which is the total time is averaged by the total number of triggers. The practical value of T_{sc} is estimated as the product of averaged trigger distance and the sampling rate. The redundant transmitted information used to aid in information recovery is known a priori at the receiver, therefore the fractional redundancies can be readily computed. The effective R_b is then calculated using (5.52) using the estimated parameters. The procedure then repeats for the window size of the next received OFDM frames.

5.3.6.2 Frame error rate

The benchmark of a digital system's performance is usually the BER. The solutions of BER for digital systems in an AWGN environment is only affected by the size of the transmitted information constellation. It is generally shown that using a maximum likelihood detector, the BER of a digital system decreases as the constellation size increases. The BER solution for a QPSK constellation is give as

$$BER_{QPSK} = erfc\sqrt{\frac{2E_b}{N_0}}, \tag{5.53}$$

where $erfc$ is the complementary error function given as

$$erfc\,(x) = 1 - \frac{2}{\sqrt{\pi}}\int_0^x e^{-t^2}dt. \tag{5.54}$$

The normalised SNR per-bit $\frac{E_b}{N_0}$ is not always available in a practical system. BER_{QPSK} is not a good indication of signal quality received in practical systems. For instance, a system may have a low BER, but if the most significant bit of the received codeword is corrupted, the signal quality is deemed unacceptable. For these reasons, frame error rate (FER) was used as a metric of robustness against the hybrid channel. An OFDM frame is transmitted with a CRC32 check code that is used at the receiver to validate the fidelity of the transmission. The FER can be calculated by checking every OFDM frame and then averaging unsuccessful frames over the total number of frames within a given window. Since every OFDM frame needs to pass the checksum, else it is discarded, the FER metric is a stricter than the BER metric, and it serves as an upper-bound limit of the BER of a received codeword.

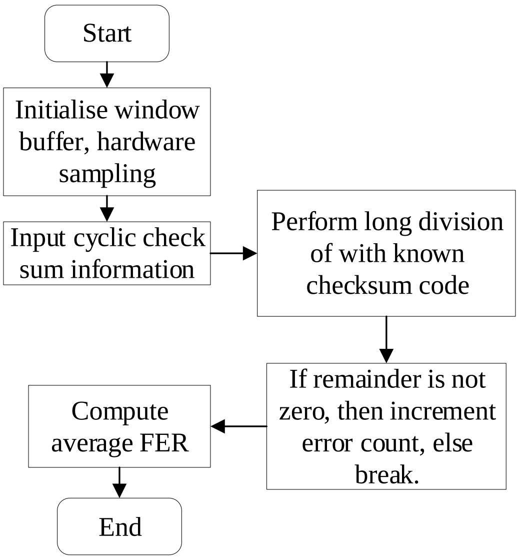

Figure 5.8. Frame error rate estimation flow diagram

FER is estimated by the procedure given by the flow diagram in Fig. 5.8. A large enough window size is defined for multiple OFDM frames, sampling rate and the received CRC32 sequences are inputs to the estimator. For a defined window, the number of received CRC32 sequences is counted, and long division is performed on each received sequence using modulo-2 arithmetic with the checksum sequence known a priori. If the remainder of a particular CRC32 sequence is not zero, then the frame error count is incremented. The FER is computed by averaging the total number of frames in error to the total number of frames within the window size. This process then repeats for the next window size of OFDM frames.

5.4 SIMO-OFDM SYSTEM SIGNAL COMBINING

A SIMO wireless system is established by using one transmit antenna element at the transmitter and multiple receive antenna elements at the receiver defined as $1 \times N_r$. The implemented SIMO-OFDM system has a 1×2 configuration, that is, one transmit antenna element and two receive antenna elements. The apparent spatial distribution of the receive antenna elements invokes spatial diversity in the system. Physically separated antenna elements will experience different propagation paths. Therefore, the idea is that the probability that the multipath signals in multiple fading channels will simultaneously experience deep fading is very low. A powerline channel is used as a method to spatially distribute the receiver antenna elements by at least 10λ apart to invoke sufficient signal diversity that will lower the signal envelope correlation of the incident waveforms on the antenna elements. The invoked signal diversity in the SIMO-OFDM system requires that diversity combining techniques be used at the receiver for demodulation. Diversity combining at the receiver is achieved through selection combining (SC), equal gain combining (EGC) and maximal ratio combining (MRC). The performance of the combining techniques is evaluated through the SNR output of the combiner. The output SNR of the combining techniques, envelope correlation and the frame error rate are then used to evaluate the performance of the SIMO-OFDM system with receive antenna elements spatially distributed through a powerline channel.

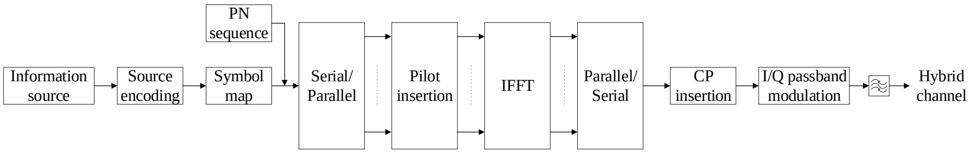

Figure 5.9. SIMO OFDM transmitter

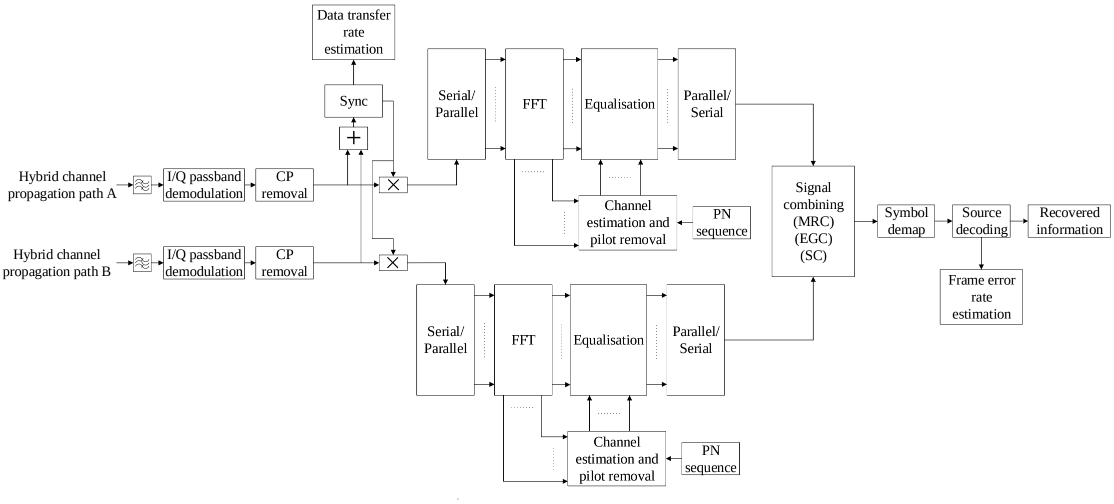

Figure 5.10. SIMO OFDM receiver

The quality of the received signal can be predicted from the SNR available at the demodulator stage. OFDM FER and output SNR of the SIMO-OFDM system are used to produce FER versus SNR plots to evaluate the performance of the system in the next chapter. The SNR at each diversity branch is the ratio of instantaneous signal power to noise power. For the 1 × 2 SIMO-OFDM system, the received signals at the diversity branches are denoted by $\Omega_{1,2}$, the signals contain the same information but are received with different strengths $\upsilon_{1,2}$ and phases $\theta_{1,2}$. For the sake of completeness, the noise components are denoted by $n_{1,2}$. The noise components are assumed to be uncorrelated with each other and any of the signals $\Omega_{1,2}$. The noise components contain the lumped effects of the propagation environment and receiver noise sources. Propagation environment noise sources combine differently with the receiver noise sources, which is unique to each diversity branch, and therefore the components $n_{1,2}$ are very much uncorrelated. Additionally the noise components do not in any way, imply or restrict the signal envelopes. Since the noise components have unrestricted spectral components, $n_{1,2}$ are expected to have zero mean and variance, and a noise power of N. The instantaneously received signal envelopes at instant t_0 are denoted by $\upsilon_{1,2}\left(t_0\right)$, and the instantaneous SNR at instant t_0 where the signal envelopes are assumed to be constant is given by

$$\gamma_{\varphi_{1,2}(t_0)} = \frac{\varphi_{signal}\left(t_0\right)}{\varphi_{noise}\left(t_0\right)} = \frac{{\upsilon_{1,2}}^2\left(t_0\right)}{E\left[{n_{1,2}}^2\left(t_0\right)\right]} = \frac{{\upsilon_{1,2}}^2\left(t_0\right)}{N}, \tag{5.55}$$

where φ_{signal} and φ_{noise} denote the signal and noise power, respectively. $\gamma_{\varphi_{1,2}}$ is a random variable that depends on the distributions of υ_1 and υ_2, and have statistics which are a function of the hybrid channel transfer characteristics. Due to the noise properties previously defined, υ_1 and υ_2 directly depend on the squared magnitude of the signal envelopes. In a practical communication system, the received signal measurements only represent the signal envelope υ and noise information is almost never present. The evaluation of the envelope statistics is what is used to evaluate the performance of a communication link, and a useful measure, in this case, is the voltage SNR γ_v which is defined as the square root of the power SNR γ_φ given as

$$\gamma_{\upsilon_{1,2}} = \sqrt{\gamma_{\varphi_{1,2}}} = \sqrt{\frac{{\upsilon_{1,2}}^2\left(t_0\right)}{N}} = \frac{\upsilon_{1,2}\left(t_0\right)}{\sqrt{N}}. \tag{5.56}$$

The advantage in using γ_v is that it is directly proportional to the signal envelopes υ_1 and υ_2, as such γ_{υ_1} and γ_{υ_2} will have similar envelope statics to υ_1 and υ_2. The evaluation of the input and output γ_v does not take into the noise. Therefore the noise component N is set to $N = 1$. It important to note that when setting N to unity no information is lost since the input envelopes υ_1 and υ_2 can readily be interpreted $\gamma_{\upsilon_{1,2}}$, that is under the assumption of $N = 1$ the signal envelopes υ_1 and υ_2 are directly related γ_{υ_1} and γ_{υ_2}.

5.4.1 Selection combining

Selection combining offers the simplest diversity combining method. The signal at the diversity branch with the largest γ_v is selected for demodulation. γ_v is estimated directly as the envelope υ. The power SNR and voltage SNR for each branch using a selection combiner are given by (5.57) to (5.60). The diversity branch with the maximum γ_v is selected for demodulation as shown by (5.61) and (5.62). The performance of the selection combiner is the resultant SNR after selection, that is simply the maximum of the two. The multiplicative noise power component $\frac{1}{N}$ in (5.61) and $\frac{1}{\sqrt{N}}$ in (5.62) is set to unity. It important to note that when setting N to unity, no information is lost since the input envelopes υ_1 and υ_2 can readily be interpreted $\gamma_{\upsilon_{1,2}}$. Thus, the diversity gain of the selection combiner is also dependent only on the distribution of the envelopes υ_1 and υ_2.

$$\gamma_{\varphi_1} = \frac{{\upsilon_1}^2}{N}, \tag{5.57}$$

$$\gamma_{\upsilon_1} = \frac{\upsilon_1}{\sqrt{N}}. \tag{5.58}$$

$$\gamma_{\varphi_2} = \frac{{\upsilon_2}^2}{N}, \tag{5.59}$$

$$\gamma_{\upsilon_2} = \frac{\upsilon_2}{\sqrt{N}}. \tag{5.60}$$

$$\gamma_\varphi = \max\left(\frac{\upsilon_1{}^2}{N}, \frac{\upsilon_2{}^2}{N}\right). \tag{5.61}$$

$$\gamma_\upsilon = \max\left(\frac{\upsilon_1}{\sqrt{N}}, \frac{\upsilon_2}{\sqrt{N}}\right). \tag{5.62}$$

5.4.2 Maximal ratio combining

Maximal ratio combining (MRC) is a linear diversity combining method used to combine replicas of the same signal received on all diversity branches. Received signal replicas are weighted according to their respective γ_υ, the signals are then linearly combined by addition and the combined signal is passed for demodulation. MRC is an optimal combiner because it exploits the signal diversity of a multiple antenna wireless system, therefore MRC outperforms SC and equal gain combining methods in terms of output SNR. The optimal performance of MRC comes at the cost of increased computational overhead. Firstly, co-phasing of the received signal replicas is crucial for MRC. Linear combining requires that the signal replicas be in phase to mitigate effects destructive interference. Signal replicas linearly combined without proper co-phasing will lead to a more distorted signal. Secondly, correct estimates of the received signal weights are required for optimal performance of the combiner. Incorrect estimation of the combiner weights could mean that signal replicas with severe fading effects contribute more to the combined output signal than favourable signal replicas with less fading, thus leading to a more distorted combined signal.

Consider a sampling time instant t_0, the signal replicas with envelopes υ_1 and υ_2 are weighted with their respective gains and are combined to give $\Omega_{S,M}(t_0)$, which is the combined signal to be demodulated. The respective gains at each diversity branch are estimated by dividing the sampled envelope υ_i with the variance of the respective envelope $Var[\upsilon_i] = \sigma^2{}_{\upsilon_i}$. The envelope with the lowest $\sigma^2{}_{\upsilon_i}$ means that is has fewer effects of fading compared to a higher $\sigma^2{}_{\upsilon_i}$, therefore the lowest $\sigma^2{}_\upsilon$ is then used to calculate the gains of each diversity branch for the MRC combiner. This ensures that the envelope with lesser fading effects contributes more to the combined signal. The combined signal can be expressed as

$$\Omega_{S,M}(t_0) = \upsilon_1(t_0)\left(\frac{\upsilon_1(t_0)}{\sigma^2{}_\upsilon}\right) + \upsilon_2(t_0)\left(\frac{\upsilon_2(t_0)}{\sigma^2{}_\upsilon}\right) \tag{5.63}$$

$$= \frac{\upsilon_1{}^2(t_0) + \upsilon_2{}^2(t_0)}{\sigma^2{}_\upsilon}, \tag{5.64}$$

where the weights are estimated directly from the envelopes of υ_1 and υ_2. The power of the combined signal is then defined as

$$\varphi_{S,M}\left(t_0\right) = {\Omega_{S,M}}^2\left(t_0\right) = \left(\frac{{\upsilon_1}^2\left(t_0\right) + {\upsilon_2}^2\left(t_0\right)}{\sigma^2{}_v}\right)^2. \tag{5.65}$$

To evaluate the γ_v of the MRC combiner, the signal power $\varphi_{S,M}$ and noise power $\varphi_{N,M}$ are required. The signal envelopes υ_1 and υ_2 contain the lumped effects of the noise components $n_{1,2}$, therefore weighting the signal envelopes effectively enhances the noise components $n_{1,2}$ by the same weights. The weighted noise components are also effectively linearly combined to give the noise signal $\Omega_{N,M}\left(t_0\right)$ expressed as

$$\Omega_{N,M}\left(t_0\right) = n_1\left(\frac{\upsilon_1\left(t_0\right)}{\sigma^2{}_v}\right) + n_2\left(\frac{\upsilon_1\left(t_0\right)}{\sigma^2{}_v}\right). \tag{5.66}$$

The noise power $\varphi_{N,M}\left(t_0\right)$ is evaluated by computing the second moment of $\Omega_{N,M}$

$$\begin{aligned}
\varphi_{N,M}\left(t_0\right) &= E\left[\left(\Omega_{N,M}\left(t_0\right)\right)^2\right] && (5.67)\\
&= E\left[\left(n_1\left(\frac{\upsilon_1\left(t_0\right)}{\sigma^2{}_v}\right) + n_2\left(\frac{\upsilon_2\left(t_0\right)}{\sigma^2{}_v}\right)\right)^2\right] && (5.68)\\
&= E\left[\frac{{n_1}^2{\upsilon_1}^2\left(t_0\right)}{\left(\sigma^2{}_v\right)^2} + \frac{2n_1n_2\upsilon_1\left(t_0\right)\upsilon_2\left(t_0\right)}{\sigma^2{}_v} + \frac{{n_2}^2{\upsilon_2}^2\left(t_0\right)}{\left(\sigma^2{}_v\right)^2}\right] && (5.69)\\
&= E\left[\frac{{n_1}^2{\upsilon_1}^2\left(t_0\right)}{\left(\sigma^2{}_v\right)^2}\right] + E\left[\frac{2n_1n_2\upsilon_1\left(t_0\right)\upsilon_2\left(t_0\right)}{\sigma^2{}_v}\right] + E\left[\frac{{n_2}^2{\upsilon_2}^2\left(t_0\right)}{\left(\sigma^2{}_v\right)^2}\right]. && (5.70)
\end{aligned}$$

The transmitter and receiver for the SIMO-OFDM system are stationary. The channel can be considered to be slow fading. As a result the signal components vary considerably slower than the noise in the channel. This means that at the demodulator stage, the channel does not change much, and the signal components υ_1 and υ_2 remain steady. In contrast, the noise components, which have infinite spectral content, vary rapidly over the received signal duration. The noise components are then assumed to be uncorrelated, the middle term of (5.70) then evaluates to zero. Signal components remain steady for long periods due to mitigation of time variations by keeping the transmitter and receiver stationary, which means the signal envelopes υ_1 and υ_2 can be factored out as constants, then $\varphi_{N,M}\left(t_0\right)$ simplifies to

$$\begin{aligned} \varphi_{N,M}\left(t_0\right) &= \frac{{\upsilon_1}^2}{\left(\sigma^2{}_v\right)^2} E\left[{n_1}^2\right] + \frac{{\upsilon_2}^2}{\left(\sigma^2{}_v\right)^2} E\left[{n_1}^2\right] \qquad (5.71) \\ &= \frac{N{\upsilon_1}^2}{\left(\sigma^2{}_v\right)^2} + \frac{N{\upsilon_2}^2}{\left(\sigma^2{}_v\right)^2} = \frac{N\left({\upsilon_1}^2 + {\upsilon_2}^2\right)}{\left(\sigma^2{}_v\right)^2}. \qquad (5.72) \end{aligned}$$

The SNR for the combiner is given by signal power $\varphi_{S,M}\left(t_0\right)$ divided by noise power $\varphi_{N,M}\left(t_0\right)$ as

$$\begin{aligned} \gamma_\varphi &= \frac{\varphi_{S,M}}{\varphi_{N,M}} \qquad (5.73) \\ &= \frac{\left(\frac{{\upsilon_1}^2+{\upsilon_2}^2}{\sigma^2{}_v}\right)^2}{\frac{N\left({\upsilon_1}^2+{\upsilon_2}^2\right)}{\left(\sigma^2{}_v\right)^2}} = N \cdot {\upsilon_1}^2 + {\upsilon_2}^2. \qquad (5.74) \end{aligned}$$

The voltage SNR γ_v is then given as the square root of γ_φ.

$$\begin{aligned} \gamma_v &= \sqrt{\gamma_\varphi}, \qquad (5.75) \\ \gamma_v &= \sqrt{N\left({\upsilon_1}^2 + {\upsilon_2}^2\right)} = \sqrt{N} \cdot \sqrt{{\upsilon_1}^2 + {\upsilon_2}^2} \qquad (5.76) \\ \gamma_v\big|_{N=1} &= \sqrt{{\upsilon_1}^2 + {\upsilon_2}^2}. \qquad (5.77) \end{aligned}$$

The noise power N that is present as a multiplicative factor is set to unity for reasons previously highlighted. The output SNR of the MRC is then given by (5.77).

5.4.3 Equal gain combining

Equal gain combining (EGC) is a simplification of MRC whereby the received signal replicas at each diversity branch are weighted by a predefined gain value and remains unchanged for all time t. Similar to MRC, the weighted signal replicas are linearly combined, and the combined signal is then passed for demodulation. Co-phasing for EGC is also required for linear combining to ensure signal replicas are added in phase and there is no destructive interference. EGC outperforms the SC method but is still inferior to MRC. Unlike MRC, EGC does not require an estimation of the instantaneous combining weights. It is cheaper to implement due to the reduced computational cost of using the same weighting factor.

Consider a sampling time instant t_0, the output of the EGC $\Omega_{S,E}(t_0)$ is a linear combination of the signal envelopes υ_1 and υ_2 weighted by the same gain factor A. $\Omega_{S,E}(t_0)$ can be expressed as

$$\Omega_{S,M}\left(t_0\right) = A\upsilon_1\left(t_0\right) + A\upsilon_2\left(t_0\right) = A\left(\upsilon_1\left(t_0\right) + \upsilon_2\left(t_0\right)\right). \tag{5.78}$$

The signal power $\varphi_{S,E}\left(t_0\right)$ is given the squared magnitude of the combined signal envelopes expressed as

$$\varphi_{S,E}\left(t_0\right) = {\Omega_{S,M}}^2\left(t_0\right) = A^2\left(\upsilon_1\left(t_0\right) + \upsilon_2\left(t_0\right)\right)^2 \tag{5.79}$$

For all time t, the weighted noise components are also effectively linearly combined by the same weighting factor A to give the noise signal

$$\Omega_{N,E}\left(t\right) = An_1 + An_2 = A\left(n_1 + n_2\right). \tag{5.80}$$

The performance of the combiner is evaluated by the SNR improve at the combiner output, the signal power is given by (5.79), the noise power evaluated by computing the second moment of $\Omega_{N,E}\left(t\right)$ as

$$\begin{aligned}
\varphi_{N,E}\left(t\right) &= E\left[{\Omega_{N,E}}^2\left(t\right)\right] && (5.81)\\
&= E\left[A^2\left({n_1}^2 + 2n_1n_2 + {n_2}^2\right)\right] && (5.82)\\
&= A^2E\left[{n_1}^2\right] + A^2E\left[2n_1n_2\right] + A^2E\left[{n_2}^2\right] && (5.83)\\
&= A^2E\left[{n_1}^2\right] + A^2E\left[{n_2}^2\right] && (5.84)\\
&= 2A^2N. && (5.85)
\end{aligned}$$

The term A^2 factors out of the $E\left[\cdot\right]$ operator because it is a constant. Under the assumption of uncorrelated noise components at each diversity branch, the middle term of (5.83) evaluates to zero. The noise power is then given by $E\left[{n_{1,2}}^2\right] = N$, and the noise power after EGC then simplifies to (5.85). γ_φ for the combiner is given by signal power $\varphi_{S,E}\left(t\right)$ divided by noise power $\varphi_{N,E}\left(t\right)$, then the voltage SNR γ_v is given as the square root of γ_φ as

$$\gamma_\varphi = \frac{\varphi_{S,M}}{\varphi_{N,M}}, \tag{5.86}$$

$$\gamma_\varphi = \frac{A^2(\upsilon_1\left(t\right)+\upsilon_2\left(t\right))^2}{2A^2N}, \tag{5.87}$$

$$\gamma_\varphi = \frac{1}{2N}(\upsilon_1\left(t\right)+\upsilon_2\left(t\right))^2. \tag{5.88}$$

$$\gamma_v = \sqrt{\frac{1}{2N}(\upsilon_1\left(t\right)+\upsilon_2\left(t\right))^2}, \tag{5.89}$$

$$\gamma_v = \frac{1}{\sqrt{2N}}\left(\upsilon_1+\upsilon_2\right). \tag{5.90}$$

$$\gamma_v\left|_{N=1}\right. = \frac{1}{\sqrt{2}}\left(\upsilon_1+\upsilon_2\right). \tag{5.91}$$

The value of A does not affect the output SNR of the combiner as shown in (5.88), for simplicity the value of A is then set to unity. The noise power N is also set to unity for reasons previously highlighted. A closer look at (5.91) reveals that unlike SC and MRC, EGC has the potential of deteriorated output SNR performance by combining signals of diversity branches compared to selecting the diversity branch with the strongest signal. Unlike MRC, using the same combining weight for all signal replicas could potentially lead to a case of severe fading effects on the combined signal. Replicas with severe fading could contribute more to the combined signal. In this case, the use of EGC deteriorates the output SNR when compared to selecting the diversity branch with the strongest signal.

5.4.4 Diversity gain

Diversity gain is evaluated as an improvement in SNR of the combined signal over the strongest diversity branch. It is a function of the signal envelope correlation, the diversity branch instantaneous SNR, number of diversity branches, link reliability and the combining technique used. Signal envelope correlation is crucial in evaluating diversity gain for multiple antenna wireless systems, it is a measure of how much signal envelopes υ_1 and υ_2 compare with each other, and it is directly related to the spatial distribution of antenna elements. When antenna elements are located in close proximity, $< \lambda$, signals will peak, fade, increase and decrease simultaneously, and will have a high envelope correlation close to one. When antenna elements are sufficiently spatially distributed, $> 10\lambda$, signals will fade independently and will have a low envelope correlation. Diversity gain and envelope correlation hold a general inverse proportional relationship. Envelope correlation, denoted by ρ, for time sampled signal envelopes υ_1 and υ_2 is given as

$$\rho = \frac{\sum_{i=1}^{N}\left[\upsilon_{1_i}(t) - \overline{\upsilon_1(t)}\right]\cdot\left[\upsilon_{2_i}(t) - \overline{\upsilon_2(t)}\right]}{\sqrt{\sum_{i=1}^{N}\left[\upsilon_{1_i}(t) - \overline{\upsilon_1(t)}\right]^2}\cdot\sqrt{\sum_{i=1}^{N}\left[\upsilon_{2_i}(t) - \overline{\upsilon_2(t)}\right]^2}}. \tag{5.92}$$

In a paper by Turkmani *et al.* [58], an extensive experiment was carried out to perform signal envelope measurements for a SIMO wireless system using SC, EGC and MRC methods. Measurements were conducted at a frequency of 1800 MHz, data from well over 900 measurements from urban, suburban, rural areas and motorways was used to derive diversity gain equations for the SIMO wireless system. Turkmani *et al.* were able to produce equations that best describe diversity gain achieved through SC, MRC and EGC at a 10% CDF level as a function of power imbalance and envelope correlation coefficient. A 10% CDF level translates into 90% reliability. In single branch systems, the signal level that is exceeded for a certain percentage of time can be obtained from the CDF of the signal envelope. Therefore a 90% reliability refers to the signal level above which 90% of the time the signal is found. In this dissertation, diversity gain is evaluated from the produced FER versus γ_v curves for SC, EGC and MRC methods. Diversity gain results in SNR improvement of the combined signal over the strongest diversity branch, and thus for a FER versus γ_v curve, diversity gain manifests itself an increase in the slope of the curve. Observing the slope increase of the FER versus γ_v curve will indicate the attained diversity gain.

5.5 GNU RADIO SOFTWARE AND HARDWARE IMPLEMENTATIONS

GNU Radio was used as the platform to implement the OFDM modulator and demodulator in software. GNU radio is an open-source software toolkit used to develop and implement SDR applications. It consists of a comprehensive library of signal processing modules and allows the user to create custom signal processing modules, the readily available modules and created modules are implemented on SDR platforms. It is used mostly by a community of hobbyists, academic researchers and commercial companies for quick prototyping and testing of RF systems. GNU Radio is primarily developed for Linux environments, but Mac and Windows operating systems are also supported.

C++ and Python are the two programming languages used in GNU radio. All the computationally extensive signal processing and performance-critical modules are written in C++, and Python is used as a high-level language to create executable flow graphs of the interconnected processing modules. This approach means that the agility of software development in a high-level language can be maximised while at the same time sidestepping its drawback of slow performance by only acting as a "glue" code and offloading the computational cost to the compiled C++ code. Simplified Wrapper and Interface Generator (SWIG) is used to "glue" the Python code to the C++ code as shown in Fig. 5.11. SWIG generates a wrapper for C++ modules and generates the corresponding Python code (*.py) and library (*.so) so that these classes and functions can be included in Python. The creation of custom modules was carried out this way in a Linux Ubuntu 18.04 environment for the development of the SIMO-OFDM system.

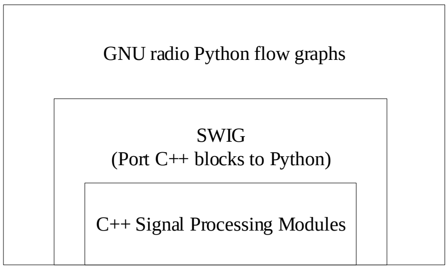

Figure 5.11. GNU radio swig interface.

5.5.1 SIMO-OFDM transmitter

Fig. 5.12 shows the executable GNU radio flow graph constructed by interconnected processing modules. In order to ease the requirements of computational power for a host computer, data flow GNU radio flow graphs employ synchronous mechanisms through stream tags. Data streams are tagged to identify the boundaries of the data frames and packets. Tagging a stream of data allows for parallel processing of the data through four main components of a tag. A tag key identifies what data does the tag represent. A tag value represents the amount of data the tag represents. A tag offset represents the position of the tag in a stream of data. The tag *scrid* is a parameter that identifies from which module the tag was attached. The concept of a tag was used to control data flow in GNU radio flow graphs due to processing delays introduced by some modules.

An audio file is used for information transmission and reception for the SIMO-OFDM system. A continuous data stream is generated by the file source, which is then converted to vectors

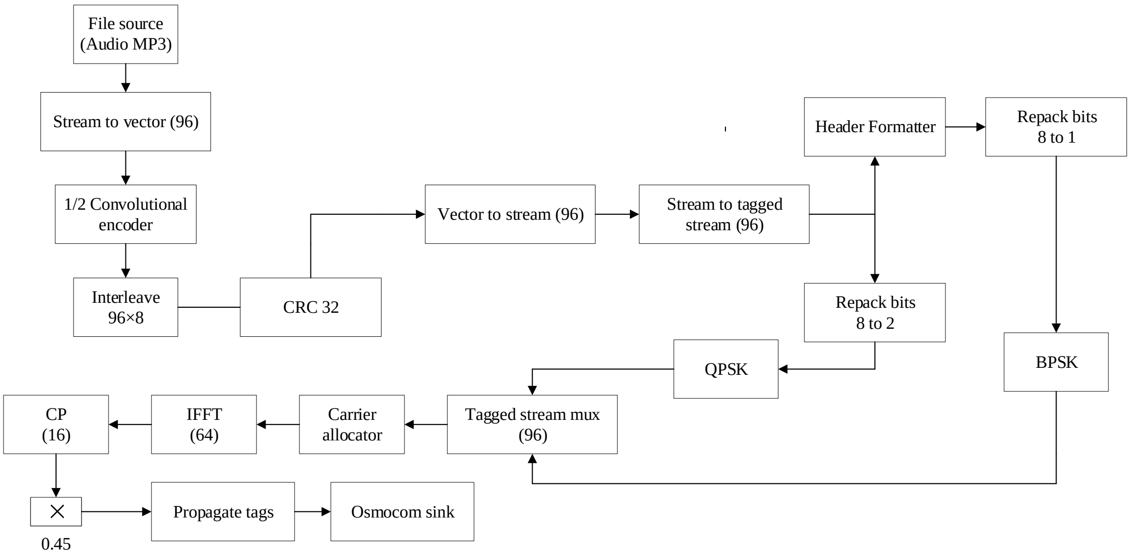

Figure 5.12. GNU radio SIMO-OFDM transmitter flow graph.

of length 96 to be encoded. I/O types between the convolutional encoder, interleaver and CRC32 modules are bytes. An encoding rate of 1/2 implies that the output vector of the encoder will double the input vector size, the interleaver does not add any information, and the CRC2 appends 4-bytes (32 bits) of redundant information. A vector to stream conversion is applied. A tag is attached to the data stream with length 96, which means every 96 items of the byte stream is tagged, forming packets of streams. Generally, data transmitted through a channel is divided into payload and header information. The payload contains the actual information being transmitted, and the header contains information to aid in reception and recovery of the payload. As a result of the difference between the payload and header, they are each processed separately in parallel at both the transmitter and receiver

The header processing path consists of the header formatter and digital modulation. At each tag of 96 items forming a packet in the data stream, the header formatter includes information about the packet length, the location of the packet in the data stream, and includes information about the CRC32 checksum. A repack of bits from 8 to 1 is performed, and header information bits are modulated using BPSK. Header information is known at both transmitter and receiver, and BPSK is used to ease receiver complexity.

The payload processing path consists of repacking of bits from 8 to 2, which leads to an interpolation factor of 4. The data stream of two bits is modulated using QPSK. The header and payload complex data streams are then combined to form a single complex tagged data stream to be transmitted. The following processing branch forms the OFDM modulation. The complex items of the data stream are then allocated to OFDM sub-carriers with indexes -26 to 26, 52 of the 64 sub-carriers are active, with allocation to 48 for the complex data stream and 4 to pilot carriers. A secondary function of the carrier allocator is to include the preamble that contains the PN sequence used to aid in synchronisation at the receiver. In effect, the carrier allocator creates the OFDM frame that contains 10 OFDM symbols with header and preamble components. An IFFT operation is then applied to the time domain data stream to convert it to frequency domain and create the OFDM signal. A CP of length 16 is appended to the OFDM signal for mitigation of multipath interference. A multiplicative constant is then used to scale the OFDM signal to an amplitude limit of $|1|$, that is because if the signal magnitude is greater than $|1|$, then it will suffer clipping. All tags are transmitted to aid in reception and recovery. Passband modulation and transmission of the OFDM signal is performed through the BladeRF x40 SDR LMS6002D analog front-end.

5.5.2 SIMO-OFDM receiver

Fig. 5.13 shows the GNU radio flow graph for the SIMO-OFDM receiver with interconnected processing modules. It should be noted that the SIMO-OFDM system was designed for half-duplex transmission and does not have any MAC layer functionality. Two BladeRF x40 SDRs are used for I/Q sampling of the transmitted OFDM signal from two receive paths. The two data streams of I/Q samples are added to form a single complex stream. Clock synchronisation and sample alignment discussed under the BladeRF hardware architecture in the next section was used to ease the requirements of signal co-phasing required for the combining techniques. The combined data stream is then passed to the Schmidl and Cox synchronisation module with a detection threshold of 0.96. The module outputs a frequency offset error component and a trigger that identifies the beginning of an OFDM frame. A frequency offset component is converted to a frequency modulated signal according to $y\left[n\right] = e^{\left(jk\sum x[n]\right)}$, where $x\left[n\right]$ is the synchroniser output and k is the sensitivity of frequency deviation given by -0.3225.

The received OFDM signal from each diversity branch is delayed by the length of the CP, then frequency offset corrections are applied by multiplying the OFDM signals with the frequency signal from the frequency mod module. Through this frequency correction, the OFDM signals are now co-phased. Signal combining is performed using combining techniques as previously defined for SC, EGC and MRC methods. This module also outputs the SNR improvement γ_v estimated for each combiner, and also estimates the signal envelope correlation from the received signals' envelope sampled data.

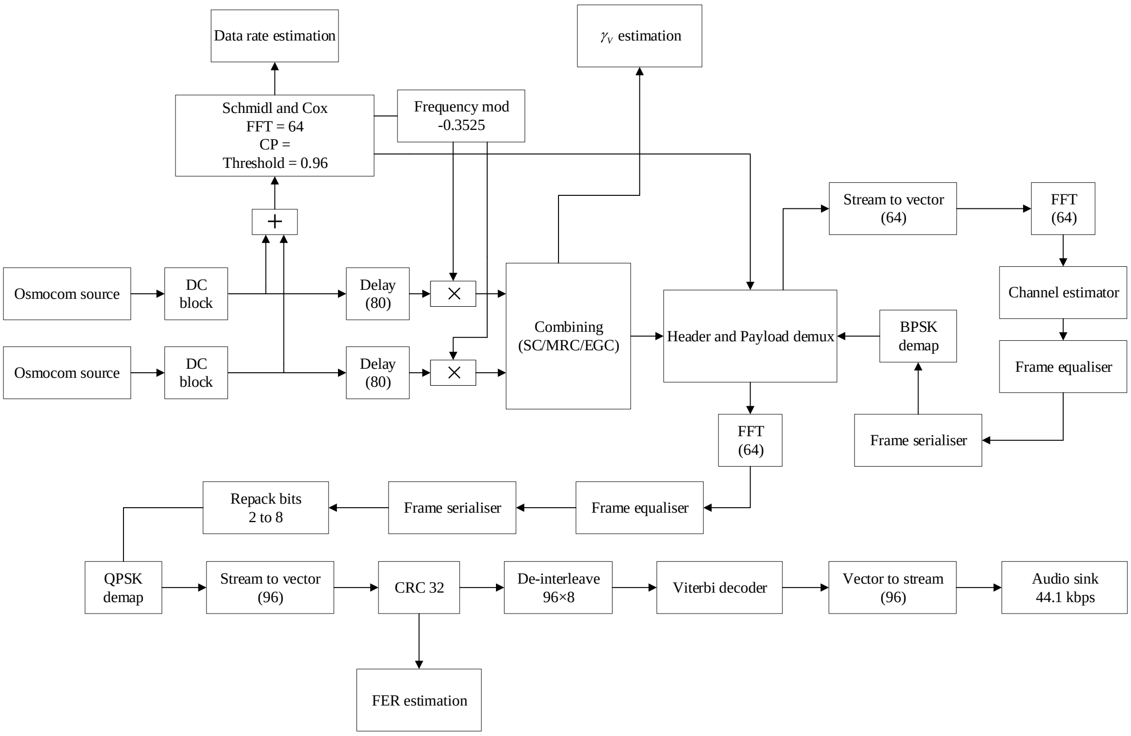

Figure 5.13. GNU radio SIMO-OFDM receiver flow graph.

Demodulation begins with the header payload demux module. This module is used to divide the received signal into the header and payload data streams, which are separated into two parallel processing paths in the flow graph. The demuxer has three inputs, that is the frame detection trigger from the Schmidl and Cox synchronisation module, the combined data stream and the output of the header processing chain is fed back into the demux to also serve as a trigger. Until an OFDM frame is detected, all the data streams received by the demux is discarded as it is considered invalid. As soon as a trigger is received, data streams of length equal to the header information identified by tags attached at the transmitter are passed into the demux. The stream of data is converted to a vector of 64 and an FFT process is applied. The channel estimation module estimates the attenuation effects of the channel using the known PN sequence as described previously, and pilot symbols at dedicated sub-carrier indexes. The complex-valued coarse frequency estimates are passed as tags and will be used for header information and payload information equalisation. Channel estimation using only the header information is used to relax the computational cost of the receiver. The header data stream is then equalised to remove channel effects. The now equalised OFDM frames are passed to the serialiser module to remove pilot symbols and transform the OFDM frame into the complex BPSK symbols. It searches for two tags in the data stream, the number of OFDM symbols in the frame and the number of complex symbols modulated. Then the header BPSK complex-valued symbols given by the serialiser are de-mapped and fed back into the demux.

The payload data stream demodulation follows a similar process as header demodulation. The demuxed payload data stream is passed through an FFT process, then using the channel estimation tags from the header information demodulation, the payload data stream is equalised to remove the effects of the channel. Like the header demodulation, the now equalised OFDM frames are passed to the serialiser module to remove pilot symbols and transform the OFDM frame into the complex QPSK symbols. The symbols are then de-mapped to produce the bit streams, which makes the I/O types now bytes. The CRC32 checksum is applied to validate the OFDM frame, also from which the OFDM frame error rate is estimated. The de-interleaver serves to reorder the information bits and to randomise transmission errors, which then allows for effective detection and correction of single errors by the Viterbi decoder. An audio sink with a sampling rate of 44.1 kHz is used for audio playback through any output device.

5.5.3 BladeRF SDR hardware architecture

The architecture of the BladeRF x40 SDR platform used for RF hardware implementation is shown in Fig. 5.14. Processing of information takes place GNU radio platform on a PC, the device's Cypress FX3 microcontroller provides seamless interfacing between PC and the device through USB 3.0. Passband modulation for transmission is handled by the device's LimeMicro LMS6002D RF transceiver, which is software configured for RF transmission and reception through the device's Altera Cyclone IV E FPGA firmware. The LMS6002D chip RF transmitter and receiver architectures are shown in Fig. 5.15 and Fig. 5.16 respectively. In the RF transmitter, the DAC produces continuous-time analog signals from the I/Q samples. The TXLPF filters remove spectral images due to the DAC zero-hold effect. TXVGA1 is used to amplify the I/Q signals to meet the input levels of the RF mixer. TXPLL generates signal tones that are 90 degrees out of phase, these are used by the mixer for passband modulation and to ensure orthogonality between the real and imagery signals. The last amplifier stage is

TXVGA2, which is used for transmission of the RF signal. TXVGA2 has a range of 0 to 25 dB and this range is controlled in the SIMO-OFDM experiment for error rate performance investigations.

In the RF receiver, the noise effects of the received signal are compensated for by RXLNA amplifier. The RF signal is then passed to the RFMIX, which uses the 90-degree out-of-phase signal tones from RXPLL to demultiplex the I/Q signals. Separate I and Q signals are then amplified by RXVGA2 and RXLPF, which removes spectral images at twice the carrier frequency, this is to condition the I and Q signals for ADC conversion by the device's Cypress FX3 microcontroller. The I/Q data streams are then sampled, and samples are passed to GNU radio on a host PC for demodulation.

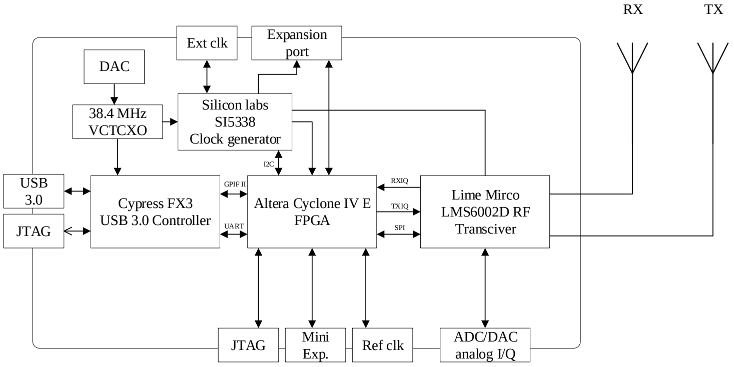

Figure 5.14. BladeRF x40 SDR architecture .

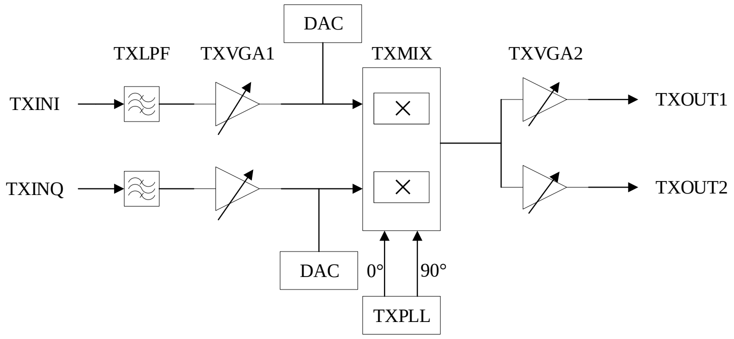

Figure 5.15. LMS6002D RF transmitter architecture.

The BladeRF x40 RF transceiver architecture shows that it does not perform frequency down-conversion using an intermediate frequency, but rather it is a direct conversion receiver, otherwise known as a homodyne receiver. These types of receivers have a common flaw in a large DC offset in the received signal. To counter this, the zeroth (DC) sub-carrier in

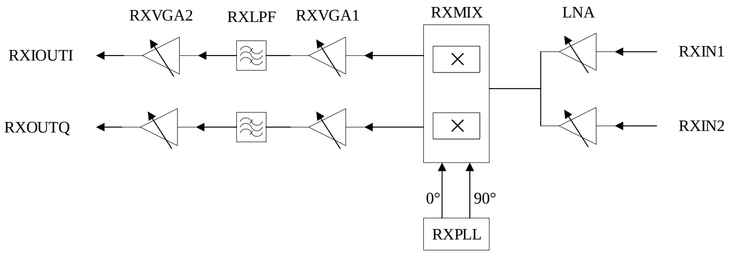

Figure 5.16. LMS6002D RF receiver architecture.

the OFDM signal was not allocated any information and the receive demodulation paths in GNU radio have a DC blocker with a suppression bandwidth of 850 kHz. The 2.4 GHz Industrial, Medical and Scientific (ISM) band was used wireless transmission because it is unlicensed and therefore allowed the system to be operated without the need for a license. RF transmission was performed at a centre frequency of 2.42 GHz using omnidirectional antenna elements.

Adjacent WiFi channels were monitored with Acrylic WiFi Home Scanner. Acrylic WiFi Home is a free tool that is used to scan WiFi channels in 2.4 GHz and 5 GHz bands. It provides real-time measurements of WiFi signals' strength in adjacent channels. RF transmission was performed mostly in night times given the lesser traffic in WiFi channels, therefore mitigating erroneous RF measurements. Caution was exercised to ensure RF transmission does not exceed the legal transmission power limits regulated by ICASA. The legally enforced maximum transmission power limit of a wireless communication link in the 2.4 GHz band is 100 mW (20 dBm), thus an upper boundary of 20 dBm was placed on RF transmission power.

The SIMO-OFDM system uses one transmit antenna element and two receive antenna elements. Therefore, two receive branches are separated by a powerline channel. Therefore two BladeRF SDRs are used to receive the PLC signals for demodulation through their respective distinct paths. In order to ease computational complexity and ensure proper OFDM synchronisation of the two diversity branches, clock synchronisation and sample alignment is performed at the hardware level. Clock synchronisation is used to ensure that the two receivers use the same clock, this ensures that both receivers have common error margins such as phase and time offsets, carrier offset etc., meaning that the resultant combined signal will also have the same error margins which can be coherently corrected for by the Schmidl and Cox synchronisation method. Sample alignment is used to ensure that samples are received at the same starting time into the GNU radio demodulator. Two scripts were developed to configure one receiver as the slave and another receiver as the master. For clock synchronisation, the master outputs a reference clock of 38.4 MHz via an SMB cable to the external clock port of the slave and instructs the slave not to use its internal clock. For the sample alignment, the J71-4 expansion ports of the two devices were connected together, the samples on both master and slave are held until the master fires a trigger to start streaming samples from both devices into GNU radio.

The two receive branches use omnidirectional antenna elements for RF reception. The signals are down-converted, transmitted through the powerline channel and received by the two BladeRF SDRs. RF signal down-conversion is performed using RF2052 PLL frequency synthesiser and mixer. RF2052 is a low-power, wideband frequency synthesiser chip with local oscillator (LO) generation through an integrated fractional-N PLL with VCOs and dividers that are used to produce a low-phase noise LO signal with a fine frequency resolution of 1.5 Hz. The chip also includes an integrated wideband bidirectional RF mixer that allows for up-conversion and down-conversion of signals in the frequency range of 30 MHz to 2500 MHz. The 2.42 GHz wirelessly transmitted signal is down-converted to 300 MHz for powerline transmission. The value of 300 MHz is motivated by exiting standards for broadband PLC applications. Recent developments of PLC technologies have reached operating frequencies of 500 MHz [94]. At such high frequencies, powerline cable EM radiation becomes of particular concern, however, the EM coupling of the powerline is then exploited by employing PLC MIMO systems. The framework of the HomePlug AV2 standard exploits MIMO capabilities of the powerline channel at such high frequencies with the aim of physical layer throughputs of hundreds of Mbps or even Gbps.

5.6 HYBRID POWERLINE-WIRELESS CHANNEL COUPLING

An understanding of the powerline network is required in order to interface the powerline channel to the system successfully. The method of powerline coupling depends on the powerline network, because the system is meant to function in indoor environments, an understanding of the indoor low voltage (LV) ternary wire powerline network must first be gained. The indoor LV powerline cable consists of three wires, namely, live (L), neutral (N) and earth (E). The L wire carries the power waveform with amplitude 230 V and 50 Hz frequency that is used to drive loads. The N wire is used to complete the circuit, it provides a return path for the current delivered by the L wire to the load, and then back to the power source transformer to sink it. The E wire is used as a safety mechanism in case of ground faults because current flow requires a complete circuit. In normal operation, the L and N wires complete the circuit, if the L wire is loose and makes contact with the appliance metal casing, the E wire will always represent the path of least resistance to return to the source. Current sinking occurs because the E and N wires are connected together at the main panel. In case of a fault, a short will occur, thereby drawing too much current and causing a trip. If the E wire is neglected and someone were to touch the appliance, it would result in electric shock. Fig. 5.17 shows the basic LV powerline network wiring in indoor environments.

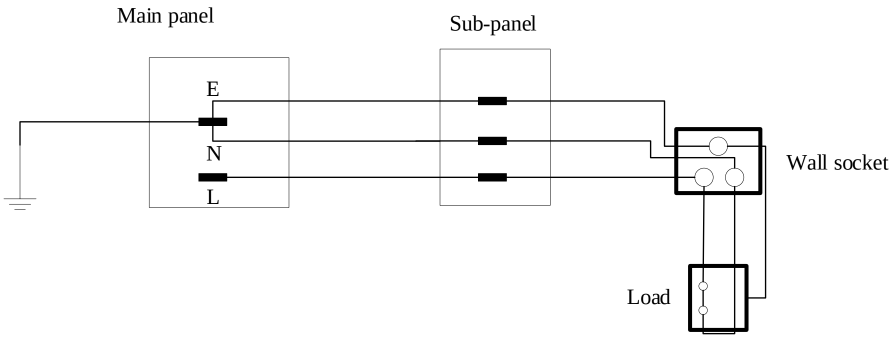

Figure 5.17. Indoor LV ternary wire power network.

Capacitive coupling method was chosen for powerline coupling because it provides a simpler method of interfacing the powerline to RF hardware, it is cheaper, flexible to design alterations, and unlike inductive coupling methods, there is no need to tamper with the powerline cables between the coupling and decoupling ends [23]. The coupling could be implemented in differential mode or common mode. In differential mode, the L and N wires are used as terminals for the PLC signals in LV networks, in medium voltage (MV) and high voltage (HV) networks where N wire is absent, the N and E wires are used as terminals for the signal. In common mode, the L and N wires are used as one terminal, and the E is used as another terminal. Differential coupling mode is the most challenging because powerline channel noise interferences are at their most severe conditions in differential mode compared to common mode coupling.

Wires of the LV powerline network can be used to establish multiple links for a PLC system. Based on the number of connections of a PLC coupling circuit, a PLC coupler can be classified

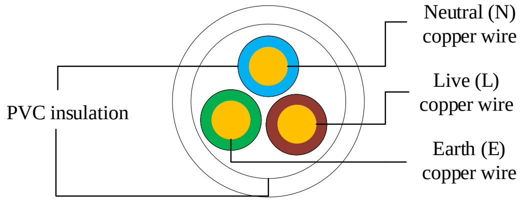

Figure 5.18. Indoor LV Cabtyre power cable.

as a SISO, SIMO, MISO or MIMO coupler [94]. The Cabtyre flexible PVC power cable shown in Fig. 5.18 is generally used for extension cables for indoor LV power distribution networks. Indoor LV power distribution networks generally use flat twin and earth cable. It consists of live (L), neutral (N) and earth (E) wires. Therefore there is a maximum of three links that can be established for information transmission in a PLC system using such a powerline channel [94]. SISO coupling offers the simplest and cheapest coupling method. The PLC signal is transmitted and received in the powerline channel using only one path formed by L-N, L-E or N-E wires. Most PLC technologies generally use this coupling method. A SIMO coupling method injects a PLC signal on one path of L-N, L-E or N-E wires, and is received through two paths formed by L-N and L-E, or N-E and L-E, or L-N and N-E wires. A MISO coupling method injects the same signal into two paths formed by L-N and L-E, or N-E and L-E, or L-N and N-E wires, and received by one path of L-N, L-E or N-E wires. The SIMO and MISO coupling methods exploit the electromagnetic interference (EMI) of the powerline channel, whereby current flowing in the same direction in the powerline causes the addition of electromagnetic fields. The electromagnetic fields of signals transmitted in the same direction then induce current fields in other paths of the powerline channel, ultimately causing the same signal to travel in multiple paths in the same direction with varying signal strengths, which improves the reliability of the communication link of a PLC system. In a MIMO PLC coupler, all paths are used simultaneously to transmit and receive information. For instance, in a 3×3 MIMO PLC coupler, a PLC signal is injected into all paths L-N, L-E and N-E, then it is received on all paths simultaneously.

For the implemented 1×2 SIMO-OFDM system, the receive antenna elements are distributed using an LV powerline network using the L-N, L-E and N-E paths. SISO coupling methods are used for both coupling and decoupling of signals received at both diversity branches. The signal received at diversity branch 1 is coupled and decoupled on the powerline channel using

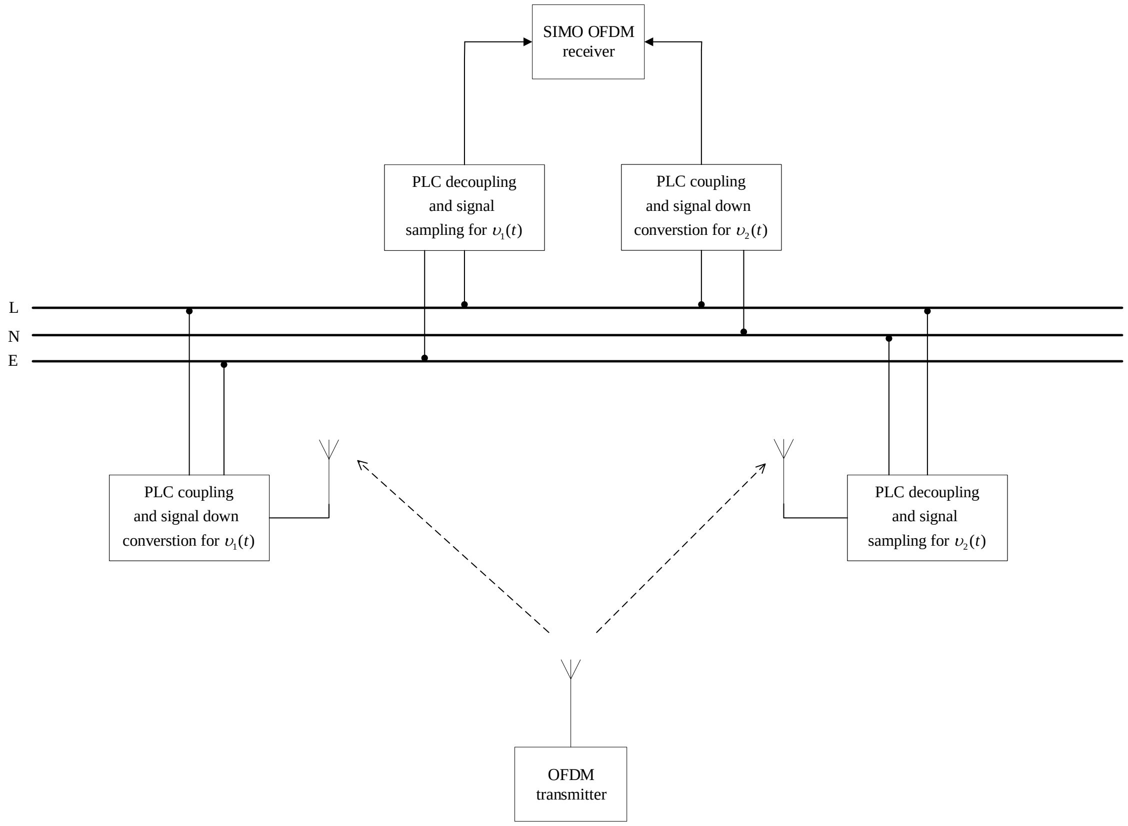

Figure 5.19. SISO PLC coupling paths for the SIMO system.

path L-E. The signal received at diversity branch 2 is coupled and decoupled on the powerline channel using path L-N. The SISO PLC paths are also used to spatially distribute the antenna elements several fractions of the signal wavelength λ apart, as shown in Fig. 5.19

In capacitive coupling, a series capacitor is used to achieve the high-pass filter transfer characteristics that will admit the high-frequency PLC signals, and attenuate the 230 V power waveform. Equation 5.93 shows the frequency and impedance inverse relationship of the series capacitor, and the high-frequency RF signal will experience low attenuation levels. In contrast, the AC power waveform will experience high attenuation levels. The capacitor will be in series with the transmitter and receiver, which generally have a load of 50Ω as shown in Fig. 5.20. The cut-off frequency of the high-pass filter transfer characteristics to admit the RF signal is given by (5.94).

$$Z = \frac{1}{-j\omega C} = \frac{1}{j2\pi fC}\angle -90^\circ. \tag{5.93}$$

$$f_{HPF} = \frac{1}{2\pi Z_L C}. \tag{5.94}$$

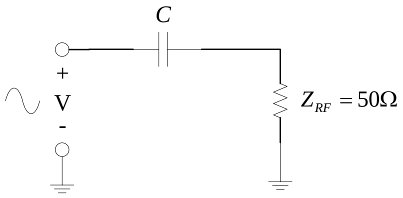

Figure 5.20. High pass filter used for PLC coupling.

Capacitive coupling circuits for $v_1(t)$ and $v_2(t)$ are shown in Fig. 5.21 and Fig. 5.22 respectively. The broadband coupling circuit was adapted from [77], it provides high-pass filter transfer characteristics that admit the high-frequency PLC signal and attenuates the AC power waveform. The coupling circuit can be used for both coupling at the transmitter and decoupling at the receiver [77]. A 1:1 transformer is used for galvanic isolation to protect the SDR hardware. On the primary side of the transformer, transient voltage surge suppressors (TVSS) with a metal oxide varistor (MOV) are used for surge protection of the coupling circuit and SDR hardware from high voltage spikes of the power distribution network. On the secondary side of the transformer, Zener diodes are connected back to back to limit transient currents on the RF hardware side.

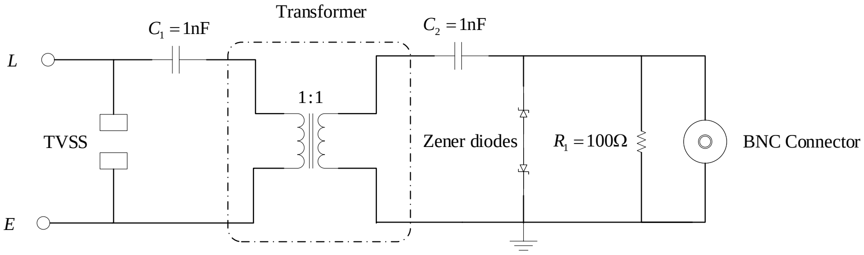

Figure 5.21. PLC coupling and decoupling circuit for signal $v_1(t)$.

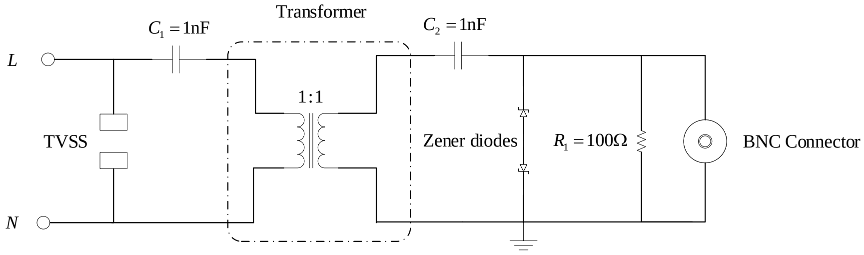

Figure 5.22. PLC coupling and decoupling circuit for signal $v_2(t)$.

5.7 CHAPTER SUMMARY

The designs and implementations of a physical layer structure for the powerline-hybrid channel were presented in this chapter. This chapter aimed to achieve the third objective of the research work, that is, to implement a suitable physical layer structure for the powerline-wireless hybrid channel for communication and information transfer purposes, thereby attaining error rate performance for such a hybrid channel. OFDM was chosen as the favourable channel access method based on the work done in previous chapters. Results of the characterisation of the powerline-wireless hybrid channel were used in this chapter to design an OFDM symbol with a suitable guard length interval to mitigate the multipath propagation effects of the hybrid channel. Robustness against hybrid channel interferences was achieved through convolutional encoding and Viterbi decoding, data interleaving and CRC32 checksum validation of OFDM frames. Methods of estimating data transfer rate and error rate were designed and implemented. Designs and implementations of SC, EGC and MRC signal combining methods were presented. GNU radio software designs and implementations of the SIMO-OFDM were presented. BladeRF SDR hardware implementations were presented. Subsequently, a full SIMO-OFDM hybrid powerline-wireless system was designed to investigate the effect of spatial diversity through spatial distribution of antenna elements using a powerline channel. Possible signal coupling methods for the SIMO-OFDM hybrid powerline-wireless system were presented, and capacitive signal coupling was used to interface the powerline channel to the wireless propagation environment, hence establishing the hybrid channel. Additionally, capacitive coupling allows powerline transmission to be performed at a much lower frequency than wireless transmission.

CHAPTER 6 SIMO-OFDM HYBRID POWERLINE-WIRELESS SYSTEM RESULTS

6.1 CHAPTER OVERVIEW

In this chapter, the hypothesis of the research work is tested. It is hypothesised that if a powerline channel is used to spatially distribute antenna elements of a multiple antenna wireless system, the error rate performance of the system can be improved. This performance improvement is a manifestation of the diversity gain attained through diversity techniques. Development of the SIMO-OFDM hybrid powerline-wireless system to test the hypothesis was presented in previous chapters. The SIMO-OFDM system uses a powerline channel to distribute the receive antenna elements multiple signal wavelengths apart. OFDM is used as the channel access method for both the powerline channel and wireless channel. From Chapter 4, it was concluded based on the characterisation of the hybrid powerline-wireless channel that such a channel has frequency selective and dispersive channel transfer characteristics. Key hybrid channel parameters extracted highlighted that a robust multi-carrier modulation method would be required to overcome the inherent challenges of such a channel. Section 6.2 outlines the SIMO-OFDM hybrid powerline-wireless system experimental procedure. Section 6.3 presents FER versus γ_v curves produced for a SISO system, and for SC, MRC and EGC combining methods in a SIMO-OFDM wireless system. This experiment was performed to validate the functionality of the SIMO-OFDM system. Section 6.4 presents FER versus γ_v curves are produced for SC, MRC and EGC combining methods for different powerline channel path lengths. The diversity gain of the SIMO-OFDM system for the combining methods manifests as an increase in the slope of the produced FER versus γ_v plots for different powerline channel path lengths. Section 6.5 presents throughput analysis of the SIMO-OFDM hybrid powerline-wireless system.

6.2 SIMO-OFDM HYBRID POWERLINE-WIRELESS SYSTEM EXPERIMENT

The experimental setup of the SIMO-OFDM hybrid powerline-wireless system is shown in Fig. 6.1. At the transmitter, a host PC with the OFDM transmission algorithms implemented in GNU Radio under a Linux environment, an audio file is used as input and is prepared for transmission. A centre frequency of 2.42 GHz is used for wireless transmission. Two receive branches with omnidirectional antenna elements are used at the receiver for RF reception. The two receive branches are spatially distributed by multiples of the wireless signal wavelength through a powerline channel. The 2.42 GHz received RF signal at each branch are down-converted to a centre frequency 300 MHz for powerline channel transmission.

Two BladeRF SDRs are then used to receive the OFDM signals through the powerline channel at a centre frequency of 300 MHz. Received samples from each receive branch are then passed to a GNU radio platform on a host PC for demodulation and audio playback of the transmitted audio file.

Table 6.1. SIMO-OFDM hybrid powerline-wireless system experiment parameters

Parameter	Value
Channel access method	OFDM
Wireless transmission	2.42 GHz
Powerline transmission	300 MHz
Transmission conditions	Line-of-sight (LOS)
Powerline spatial distributions	[10λ;20λ;50λ;100λ]
Coupling method	Capacitive
Information transmitted	Audio file (MP3)
Number of transmitters	1
Number of receivers	2
Transmit power (dBm)	[0,2,...,20] dBm
Measurement time	60 seconds

Parameters of the SIMO-OFDM hybrid powerline-wireless system experiment are summarised

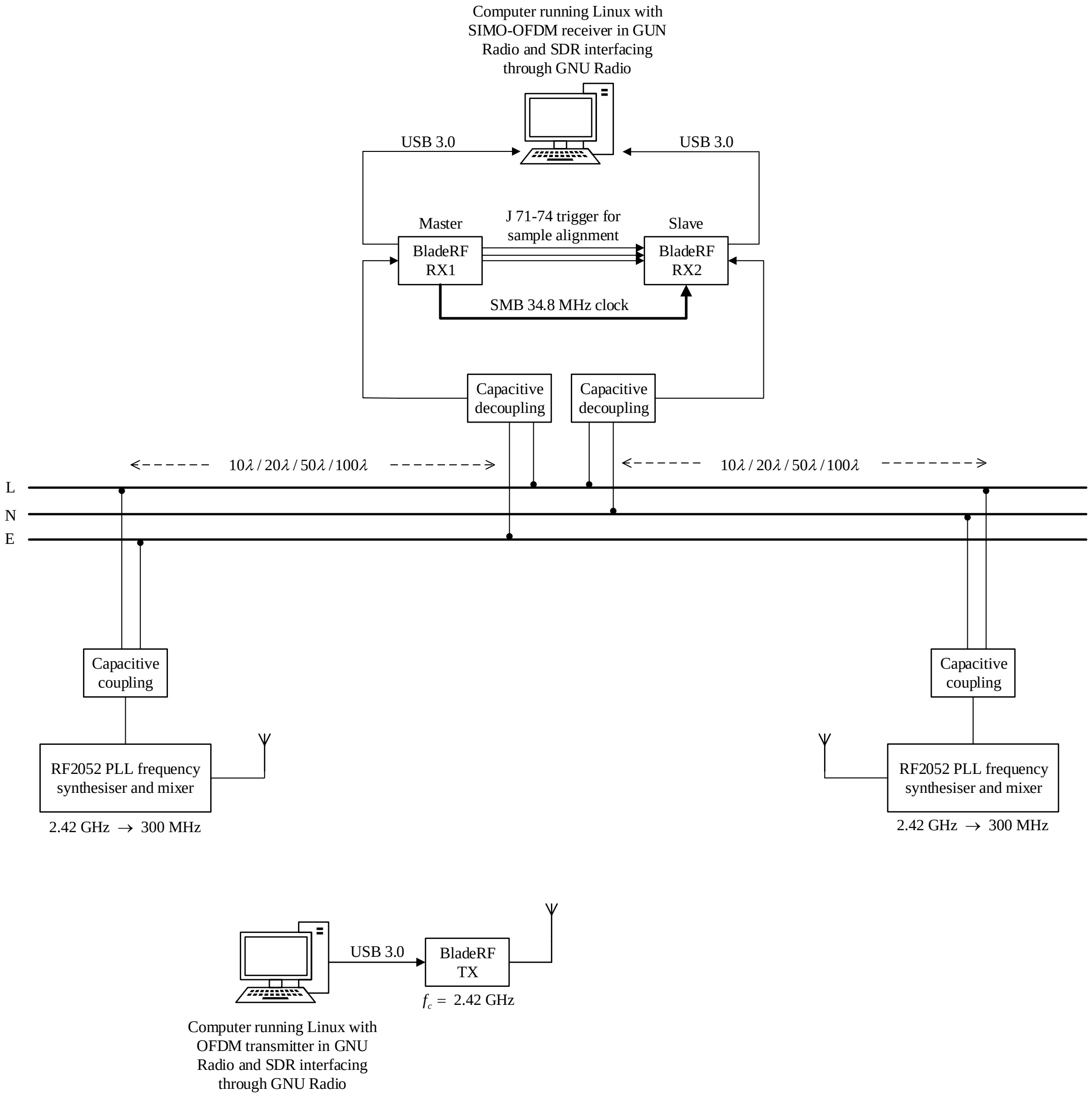

Figure 6.1. SIMO-OFDM hybrid powerline-wireless system experiment setup

in Table. 6.1. The transmission power of the BladeRF SDR transmitter is varied from 0 dBm to a maximum of 20 dBm in increments of 2 dBm, which is done for each antenna element spatial distribution. For a particular spatial distribution and for each signal combining scheme, γ_v is estimated iteratively for all increments of 2 dBm in the range of the transmit power for a measurement time of 60 seconds. Wireless transmission was performed under line-of-sight conditions.

6.3 SIMO-OFDM WIRELESS SYSTEM ERROR RATE PERFORMANCE

The SIMO-OFDM system was tested first without powerline channel antenna element spatial distribution. The objective of this test was to validate the functionality of the SIMO-OFDM system. The performance of the SC, EGC and MRC combining techniques was evaluated through the produced FEC versus γ_v curves. For the test as shown in Fig. 6.2, three BladeRF x40 SDR boards were used, one host PC running Linux 18.04 with GNU radio transmission algorithms and another host PC at the receiver with GNU radio reception algorithms. An audio file was used as input and prepared for transmission, at the receiver demodulation was performed, and audio playback was used to confirm the functionality of the SIMO-OFDM system.

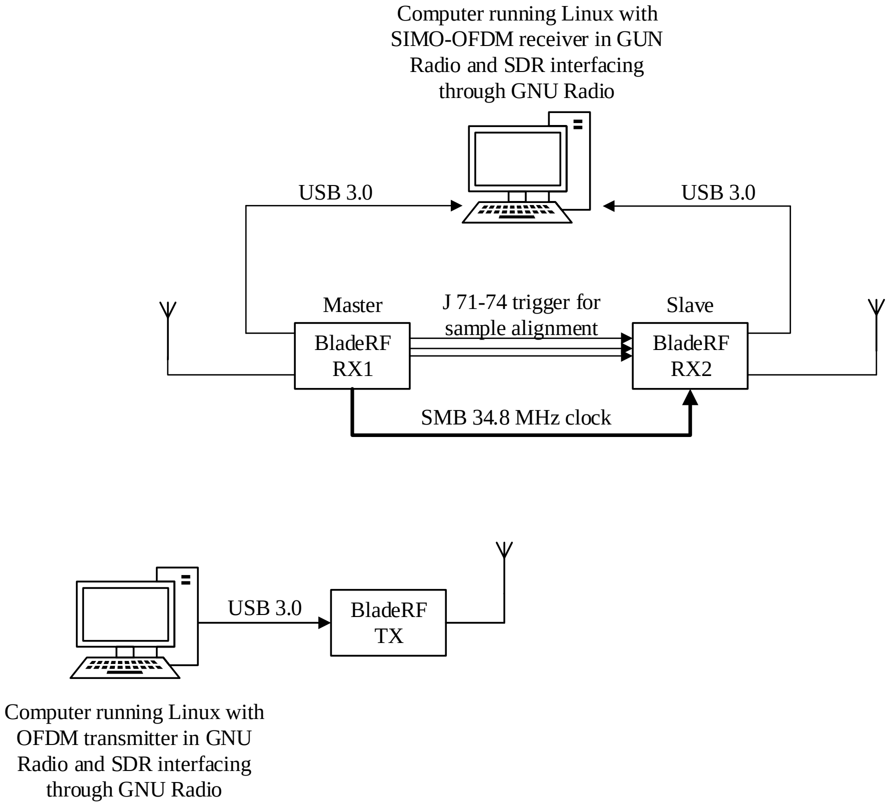

Figure 6.2. SIMO-OFDM system without antenna element spatial distribution through power line

Receive antenna element spatial distribution was estimated using the following equation

$$d_t d_r = \frac{\lambda R}{\max\{M_t, N_r\} \operatorname{Cos}\theta_t \operatorname{Cos}\theta_r} \tag{6.1}$$

where $d_t d_r$ is a design metric for MIMO wireless systems that is a product of the transmit antenna spacing d_t and receive antenna spacing d_r [95]. λ is the signal wavelength and R is the path length from the transmitter to the receiver, θ_t and θ_r are the angle of elevation of the transmitter and receiver antenna elements. Equation 6.1 is used to provide the antenna element spacing for MIMO system under rich scattering environments. For the case of a SIMO system, the value of d_r was set to unity because there is only one antenna element used at the transmitter. Path distance R between the transmitter and receiver was set to $R = 5\ m$. Angles of elevation θ_t and θ_r were set to zero, and both the transmitter and receiver antenna elements were positioned at the same height from the ground during the tests. $\lambda = c/f$, with $c = 3 \times 10^8\ m.s^{-1}$ and $f = 2.42$ GHz, then $\lambda = 0.124\ m$. Substituting all these values, $d_r = 0.31\ m$. This is the separation of antenna elements commonly used for indoor commercial routers. Fig. 6.3 shows the error rate performance of SC, EGC and MRC with the minimum antenna element separation of $d_r = 0.31\ m$. For the sake of completeness, the error rate performance of a SISO link with a path length of $R = 5\ m$ is also included.

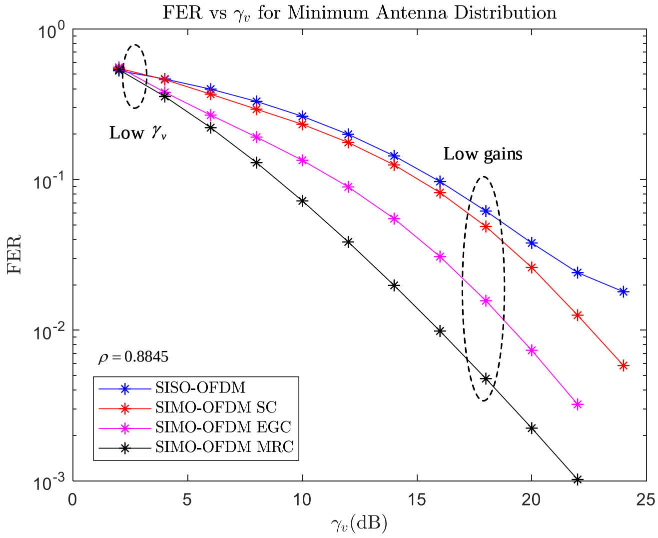

Figure 6.3. FER vs γ_v for SISO, SC, EGC and MRC methods for minimum antenna separation

High error rates are experienced for all combiners and the SISO link in the low region of γ_v, this is expected due to low transmit power. Error rate performance of the SISO link and SC method closely compare with each other, this is mainly due to a high envelope correlation of $\rho = 0.8845$ for the minimum separation of $d_r = 0.31\ m$. $\rho = 0.8845$ is representative of EM coupling effects experienced in the multipath propagation environment, therefore coupling effects are experienced by signals in both the powerline and wireless channels. It should be noted that ρ represents the lumped EM coupling effects of the propagation environment. EM coupling due closely located antenna elements causes distortions in the radiation patterns. $d_r = 0.31\ m$ is much lower than the recommended separation of $10\lambda = 1.24\ m$ in literature to render notable diversity gain improvements. However, at $d_r = 0.31\ m$ minimal diversity gains are attained for all γ_v regions.

6.4 SIMO-OFDM HYBRID POWERLINE-WIRELESS SYSTEM ERROR RATE PERFORMANCE

FER versus γ_v curves for the SIMO-OFDM system with spatial distribution through a powerline channel shown in Fig. 6.1 are given in this section. Experimental parameters are kept the same as in Table. 6.1, with spatial diversity is investigated through receiver antenna element spatial distributions of 10λ, 20λ, 50λ and 100λ multiples of the wavelength $\lambda = 0.124\ m$. The distributions are then given as $1.24\ m$, $2.48\ m$, $6.2\ m$ and $12.4\ m$. For each distribution, the FER versus γ_v curve is produced for SC, EGC and MRC combiners, including the estimated signal envelope correlation. Diversity gain is then evaluated as the change in the slope of the curves.

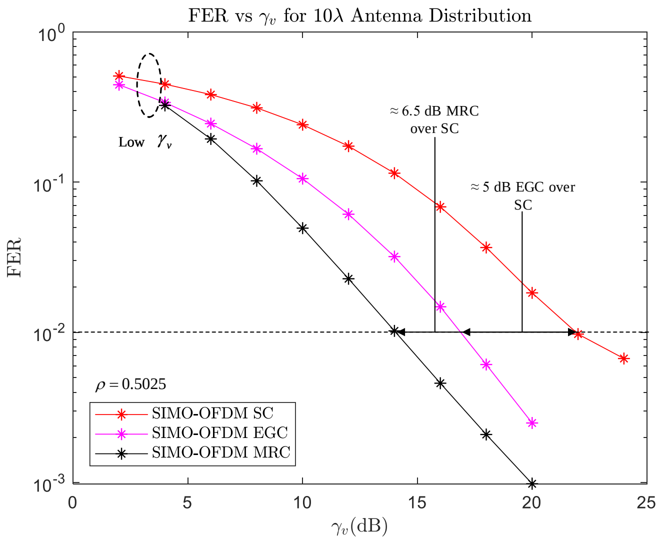

Figure 6.4. FER vs γ_v for SC, EGC and MRC methods for 10λ

Fig. 6.4 shows the SIMO-OFDM error rate performance of SC, EGC and MRC for 10λ antenna element distribution through a powerline channel. Optimal error rate performance was achieved through MRC, and SC provided the worst FER performance, however, significant gains are attained for all combining methods for γ_v regions. For an error rate of 10^{-2}, EGC requires 5 dB less power than SC, hence a diversity gain improvement of approximately 5 dB for EGC over SC. Gain improvements come as a result of co-phased linear signal combining of EGC and MRC methods. For the same error rate, diversity gain improvement of 6.5 dB is attained for MRC over SC. 10λ means that $d_r = 1.24\ m$, a lower envelope correlation of $\rho = 0.5025$ is attained. ρ is lower because of the inverse proportional relationship with d_r. It should be noted that ρ is representative of the lumped EM coupling effects the hybrid channel.

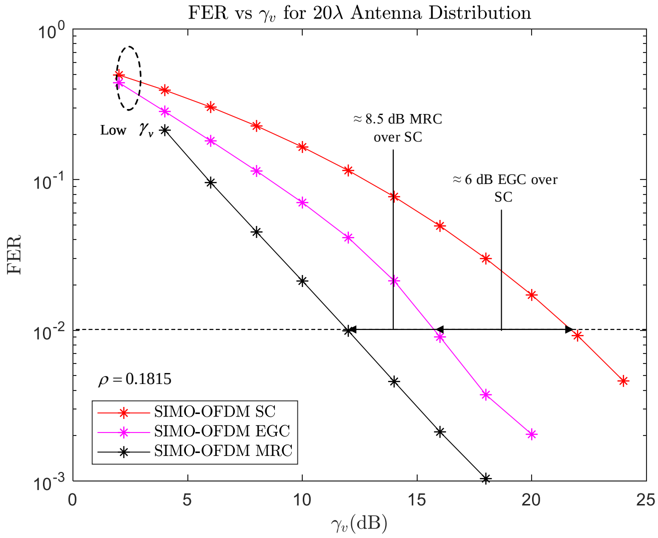

Figure 6.5. FER vs γ_v for SC, EGC and MRC methods for 20λ

Fig. 6.5 shows the error rate performance attained for SC, EGC and MRC methods for 20λ antenna distribution using a powerline channel. MRC continued to outperform all combiners for all γ_v regions. For an error rate of 10^{-2}, diversity gain improvement of 6 dB is attained for EGC and 8.5 dB for MRC compared to SC. Gain improvements of 1 dB and 2 dB are attained for EGC and MRC, respectively, for 20λ compared to 10λ antenna element spatial distribution. 20λ means that $d_r = 2.48\ m$, an increase in d_r shows a significant decrease in envelope correlation given by $\rho = 0.1815$. Increase of d_r results in reduced EM coupling effects.

FER performance of all combining methods for a large distribution of 50λ is given by Fig. 6.6. The goal of such a large distribution was to investigate the consistency of gains attained by spatial diversity. Moreover, to investigate at what point do losses experienced in the hybrid

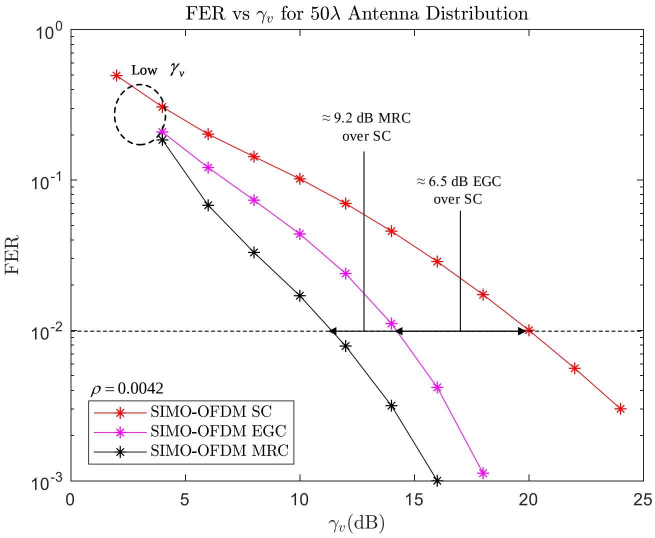

Figure 6.6. FER vs γ_v for SC, EGC and MRC methods for 50λ

channel become significant due to limitations placed on antenna element spatial distribution by the experimental parameters and apparatus. Narrowing of the γ_v regions is observed between the EGC and MRC curves as a result of losses in the hybrid channel. A 1 dB gain improvement is attained for all combiners for 50λ compared to 20λ antenna element spatial distribution. An even lower envelope correlation of $\rho = 0.0042$ is given for 50λ, that is $d_r = 6.2\ m$.

Fig. 6.7 shows the FER performance at the spatial distribution of 100λ. At this point, losses experienced in the hybrid channel begin to affect the system performance. Significant narrowing between EGC and MRC curves is observed for all γ_v regions. For an error rate of 10^{-2}, EGC requires 6.2 dB less than SC, a loss of 0.3 dB is experienced at 100λ compared to 50λ for EGC. For the same error rate, MRC requires 8.5 dB less than SC, giving a total loss of 0.7 dB for MRC. At such a high antenna element distribution, the signal envelope correlation should ideally be zero, however, this would imply that only a wireless channel is used. Given the nature of the hybrid channel, as a result of EM coupling effects still present in the powerline channel propagation paths, the envelope correlation is given by $\rho = 0.0028$.

FER performance for each combiner for 10λ, 20λ, 50λ and 100λ antenna element spatial distributions are given in Fig. 6.8 for SC, Fig. 6.9 for EGC and Fig. 6.10 for MRC. Gains attained for SC FER curves show an almost linear increase with the increase in d_r. The

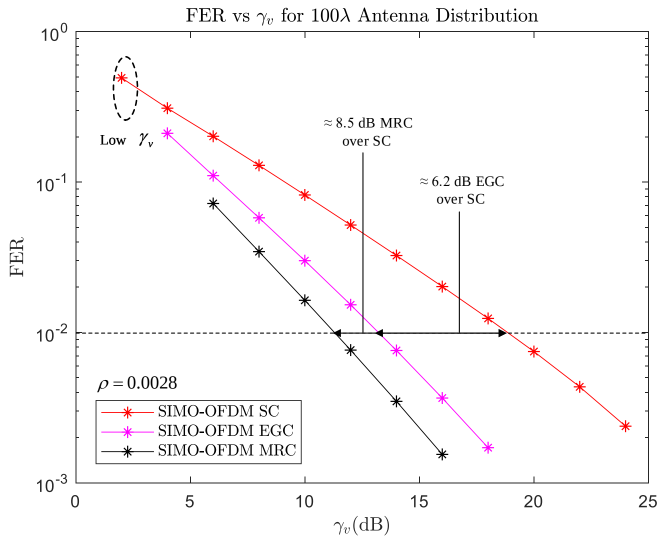

Figure 6.7. FER vs γ_v for SC, EGC and MRC methods for 100λ

approximate linear characteristics are due to the simple implementation of selecting the strongest diversity branch, even at 100λ. Narrowing between 50λ and 100λ spatial distribution curves can be attributed to losses of the hybrid powerline-wireless channel that become significant at a 100λ powerline distribution. Gains attained for EGC FER performance also show an approximately linear relationship with the increase in d_r. Losses experienced in the hybrid channel as d_r increases result in the erroneous estimation of instantaneous signal envelopes. The FER curve at 100λ show losses in gains in lower γ_v regions and narrowing between 50λ and 100λ curves for all γ_v regions. An almost exact error rate performance between 50λ and 100λ curves for MRC show that little to absolutely no gains are attained by increasing d_r beyond 50λ. FER curves for 100λ show further gain losses in the low γ_v regions as the result of the hybrid channel. An increase in γ_v does not offer error rate improvements. Losses are attributed to unfavourable channel transfer characteristics for long powerline channel path lengths, as was shown in Chapter 4. Additionally, an increased powerline channel length effectively turns the channel into a radiating element. The PLC signal paths in close proximity potentially experience enhanced EM coupling which in turn distorts the PLC signals. An advantage of short powerline channel lengths is that signal energy can be detected at lower transmit powers. Effectively, short powerline channels have favourable transfer characteristics as was shown in Chapter 4. This is observed by the error rate estimates available for the full range of γ_v for 10λ and 20λ. For 50λ and 100λ, signal energy is detected at higher transmit powers. This is observed by error estimates staring at higher γ_v ranges.

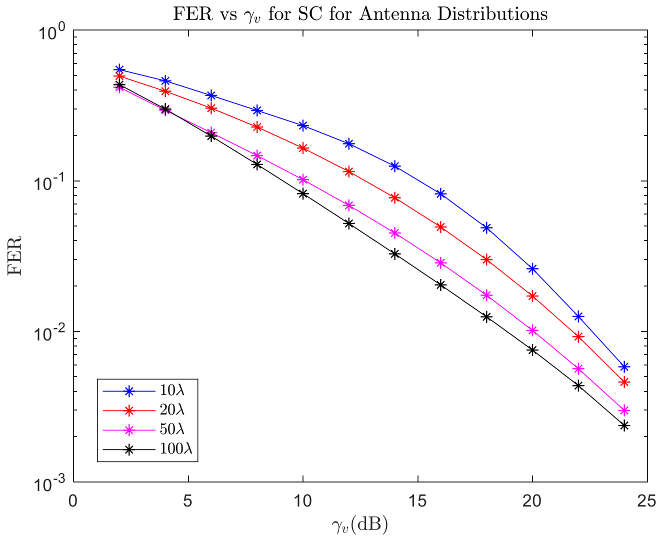

Figure 6.8. FER vs γ_v of SC for 10λ, 20λ, 50λ and 100λ

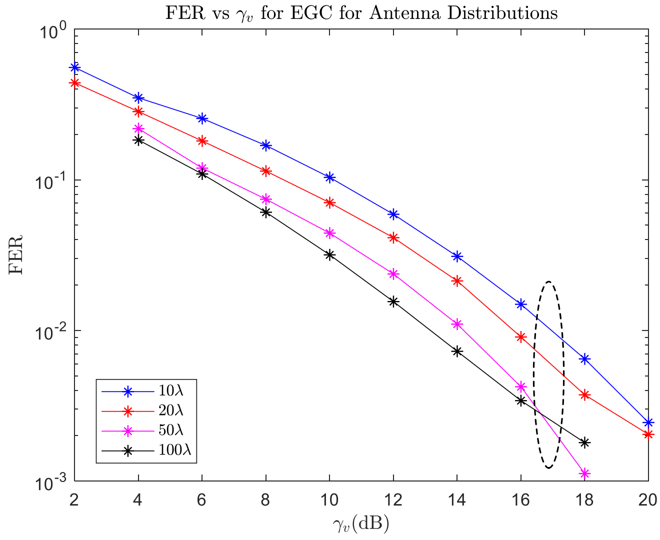

Figure 6.9. FER vs γ_v of EGC for 10λ, 20λ, 50λ and 100λ

It is evident from the FER performance of the combiners that spatial distribution of 50λ is placed as an upper boundary on the achievable distribution through a powerline channel for the SIMO-OFDM system. Ultimately the upper boundary is a limitation of the experimental parameters and apparatus. Using a much lower frequency for PLC, losses experienced at 100λ powerline channel distribution could be mitigated, and the upper boundary could be improved. A lower frequency than 300 MHz would allow for larger antenna element distribution through

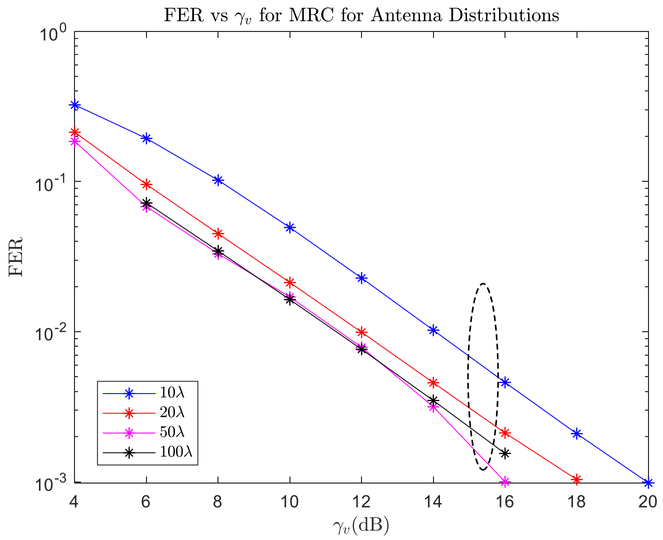

Figure 6.10. FER vs γ_v of MRC for 10λ, 20λ, 50λ and 100λ

the powerline channel beyond 100λ, therefore it would require longer powerline lengths at lower frequencies for PLC signal paths to experience enhanced EM coupling. However, a lower frequency for PLC comes with a higher probability of impulsive noise interferences that could severely distort the PLC signal. In the case of OFDM, impulsive noise could cause loss orthogonality among sub-carriers, thus increasing the complexity of synchronisation requirements of the receiver. This trade-off was made to keep the complexity of the receiver low.

6.5 SIMO-OFDM HYBRID POWERLINE-WIRELESS SYSTEM THROUGHPUT

The throughput of the SIMO-OFDM system is of the amount of information that is successfully transmitted and received through the hybrid powerline-wireless channel. An audio file was transmitted and received, and continuous audio playback quality was used to determine if the information was successfully transmitted through the hybrid channel and successfully recovered. Continuous audio playback was successfully achieved with antenna element distributions of 10λ, 20λ and 50λ. Audio playback for 100λ antenna element distribution was continuously interrupted for EGC and MRC methods. Interruptions can be attributed to erroneous estimations instantaneous signal envelopes, which results in erroneous signal combining. Losses experienced by EGC and MRC at 100λ are shown in Fig. 6.9 and Fig. 6.10, respectively. Due to the experiment parameters, an upper boundary of 50λ is placed on successful continuous audio playback.

The data transfer rate is only dependent on the structure of the information. Theoretical analysis of the transfer rate generally assumes that no redundant information is transmitted with the payload. In practical systems, the payload is transmitted along with redundant information that is used to aid in payload recovery at the receiver. The theoretical data transfer rate metric was revised with consideration of redundant information represented by the fractional components $\alpha_{total} = \alpha_{sync} \cdot \alpha_{CP} \cdot \alpha_{CRC-32} \cdot \alpha_{parity}$. The redundant information is known at both the transmitter and receiver, thus added redundancies can be readily computed at the receiver giving the effective data rate as

$$R_b = \frac{N_{sc} \log_2 M}{T_{sc}} \cdot \alpha_{total}, \tag{6.2}$$

where the fractional components α denote the redundant information added. Equation 6.2 gives the effective bit rate of the OFDM system in a practical sense. It shows that the actual audio information makes up a small fraction of the transmitted information. Therefore bandwidth efficiency is traded for the extra overhead that is required by the system to have a reliable data transfer link. Following the procedure for data rate estimation in Chapter 5, a consistent R_b of 320 kbps was attained with deviations of ± 5 kbps for SC, EGC and MRC methods for antenna element spatial distributions of 10λ, 20λ and 50λ. For good audio playback quality, transfer rates of +96 kbps are recommended for MP3 files. At a stereo sampling rate of 44.1 kHz, good audio quality was attained. For 100λ antenna element spatial distribution, deviations from the 320 kbps rate were as high as $\pm$ 150 kbps due to losses and erroneous signal envelope estimations. Continuous audio playback interruptions could also be attributed to delays introduced by the processing of redundant information at the receiver for recovery. These interruptions become severe with increased redundant information, such as higher FEC encoding rates, longer CP lengths, longer CRC32 checksum etc., which then causes non-continuous audio playback. For the purposes of the investigations conducted in this dissertation, the information structure with the chosen and added redundancies was deemed suitable and continuous audio playback was achieved.

6.6 CHAPTER SUMMARY

This chapter aimed to test the hypothesis of the research work. It was hypothesised that if a powerline channel is used to spatially distribute antenna elements of a multiple antenna wireless system by at least 10λ, error rate performance improvements can be attained. The objectives of the research work were addressed in previous chapters. The hypothesis was tested by setting up an experiment for a 1×2 SIMO-OFDM system with antenna element spatial distribution through a powerline channel. The effectiveness of the spatial diversity was investigated by incrementing the spatial distribution by multiples of the signal wavelength. Error rate performance improvements were observed by the increase in the slope of the produced FER versus γ_v curves with the increase in spatial distribution. An increase in the slope of the FER versus γ_v is a manifestation of the achieved diversity gain. Concurrently, signal envelope correlation was observed to decrease with an increase in spatial distribution. This implies that the wirelessly transmitted signal is received by increasingly independent diversity branches. Experimental parameters and apparatus of the SIMO-OFDM system placed limitations on the achievable spatial distribution, hence diversity gain. Nevertheless, as a result of the attained error rate performance, the hypothesis is proven and accepted.

CHAPTER 7 CONCLUSIONS

Spatial diversity in multiple antenna wireless systems is based on the idea that multiple information-carrying signals received on spatially distributed diversity branches will propagate in different paths and will experience different fading conditions. The received information-carrying signals are combined, hence an improvement in link reliability due to the exploitation of the multipath propagation environment. In consumer electronics antenna elements are often located in close proximity, $< \lambda$, due to form size constraints, as such performance improvement through spatial diversity is limited even though multiple antenna systems are employed. If antenna elements are sufficiently separated, $> 10\lambda$, multiple information-carrying signals will experience different propagation paths with different fading conditions. Through diversity combining the instantaneous fading effects are mitigated and the mean output signal level is improved. Power line communication was used as a method to spatially distribute antenna elements of a 1×2 wireless SIMO-OFDM system for indoor environments. PLC has the advantage of reusing existing indoor AC power wiring as a communication channel, and therefore the deployment cost of PLC is very low. Spatially distributing receive antenna elements of the 1×2 SIMO-OFDM system using a powerline channel requires that hybridism of powerline and wireless channels be employed. A hybrid powerline-wireless channel is established by concatenating a powerline channel and a wireless channel using powerline coupling. This cooperative use of powerline and wireless channels allows for the convergence of the different technologies instead of rivalling. Such hybrid systems provide critical insight into the behaviour of hybrid channels, their potential benefits and inherent limitations.

7.1 RESEARCH OUTCOMES

- A comprehensive literature study was conducted covering topics of power line communication, signal diversity and hybridism of powerline and wireless channels. An overview of the current status of cooperative use of power line communication and wireless technologies were presented, from which a research gap of the application of hybrid powerline-wireless channels in multiple antenna wireless systems was identified. In particular, a hybrid channel established by cascading a powerline channel and a wireless channel. Through the use of a correlative sequence-based channel sounding method, it has been shown that such a unified channel is frequency selective and has dispersive channel transfer characteristics. The extraction of the channel time delay parameters shows that a multi-carrier system is more suited for such a channel. This was substantiated by an investigation of single-carrier modulation and multi-carrier modulation in a multipath propagation powerline channel environment conducted in simulation. OFDM was chosen as the candidate for multi-carrier modulation. The produced BER curves highlighted that OFDM is robust against the powerline channel inherent interferences compared to single-carrier modulation.

- A physical layer structure for the SIMO-OFDM hybrid powerline-wireless system was designed using GNU radio software platform and BladeRF x40 SDR hardware. OFDM symbol structure was designed based on the extracted time delay parameters of the hybrid channel to be robust against channel multipath propagation effects. Source encoding and decoding of the physical layer structure was designed to be robust against interferences of the hybrid channel. SC, EGC and MRC signal combining methods were designed and implemented. Estimation methods for error rate, data transfer rate and SNR of the SIMO-OFDM system were designed and implemented. Capacitive signal coupling was used to interface the powerline channel to the wireless propagation environment, hence establishing the hybrid channel. This method also allowed powerline transmission to be performed at a much lower frequency than wireless transmission.
- An experiment was conducted to investigate the effect of spatial distribution on a 1×2 SIMO-OFDM hybrid powerline-wireless system for indoor environments. Results of the experiment were error rate curves produced for powerline channel distribution lengths of 10λ, 20λ, 50λ and 100λ. Error rate performance improvements were achieved for 10λ, 20λ and 50λ powerline spatial distributions as a manifestation of diversity gain. At 100λ, the powerline channel inherent inferences were overwhelming and losses were experienced. For EGC and MRC, longer powerline channel lengths showed unfavourable transfer characteristics, which resulted in the erroneous estimation of the signal envelopes. Experimental parameters and apparatus placed a limitation on the achievable spatial distribution of diversity branches, hence the achievable diversity gain. Nevertheless, all

the objectives of the research work were achieved, the research questions posed were addressed, and the hypothesis of the research work was tested and accepted.

7.2 FUTURE WORK

The research work conducted in this dissertation provided the first investigation of cooperative use of wireless and powerline channels by using a powerline channel to spatially distribute diversity branches of a 1×2 SIMO-OFDM hybrid powerline-wireless system. Experimental parameters and apparatus placed a limitation on the achievable spatial distribution of diversity branches, hence the achievable diversity gain. The attained results can be improved by employing different techniques in the experiments. Further investigation on the application of cooperative use of PLC and wireless technologies can prove to be beneficial for emerging next-generation communication technologies. In this regard, possible future research avenues to advance this research area are suggested as follows.

- The developed SIMO-OFDM system can be extended to a full MIMO-OFDM system through the development of a physical layer structure employing space-time coding techniques. Through the spatial distribution of both transmitter and receiver antenna elements, system error rate and throughput performance metrics can be investigated.
- Characterisation of a hybrid powerline-wireless channel through analytical analysis proves to be a difficult task. The computational complexity of mathematical modelling can be offloaded to machine learning (ML) techniques. ML techniques can be applied to collect data of such hybrid channels and capture the input-output relations. This can be applied to levels of characterisation and modelling, physical layer design and MAC layer design for such hybrid systems.
- Primarily, the idea of spatial diversity is to improve error rate and throughput performance of a multiple antenna wireless system. However, when antenna elements of a wireless system are widely separated, an improvement in servicing multi-users can be attained. In commercial routers, antenna elements can be used for both uplink and downlink, by widely separating antenna elements, uplink and downlink can be handled by one antenna element. Therefore each antenna element services multiple independent users that operate at the same frequency and sharing the same band. Consequently, coverage of broadband services can be effectively improved.

REFERENCES

[1] M. K. Simon and M. S. Alouini, *Digital Communication over Fading Channels*, 2nd ed. John Wiley and Sons, 2005.

[2] J. G. Proakis, *Digital Comminications*, 5th ed. McGraw-Hill, 2008.

[3] J. R. Barry, E. A. Lee, and D. G. Messerschmitt, *Digital Communications*, 3rd ed. Springer Science and Business Media, 2004.

[4] Y. S. Cho, J. Kim, W. Y. Yang, and C. G. Kang, *MIMO-OFDM Communications with Matlab*, 1st ed. John Wiley and Sons, 2010.

[5] S. M. Alamouti, "A Simple Transmit Diversity Technique for Wireless Communications," vol. 16, no. 8, pp. 1451–1458, 1998.

[6] V. Tarokh, H. Jafarkhani, and a. R. Calderbank, "Space-Time Block Codes from Orthogonal Designs," *IEEE Transactions on Information Theory*, vol. 45, no. 5, pp. 1456–1467, 1999.

[7] D. Mitic, A. Lebl, B. Trenkic, and Z. Markov, "An overview and analysis of BER for three diversity techniques in wireless communication systems," *Yugoslav Journal of Operations Research*, vol. 25, no. 2, pp. 251–269, 2015.

[8] D. Lee, G. J. Saulnier, Z. Ye, and M. J. Medley, "Antenna diversity for an OFDM system in a fading channel," in *Proceedings Military Communication Conference*, no. 6,

1999, pp. 1104–1109.

[9] H. M. Jones, A. Saha, and T. D. Abhayapala, "The Effect of Finite Antenna Separation on the Performance of Spatial Diversity Receivers," *International Symposium on Signal Processing and Its Applications*, vol. 2, no. 7, pp. 515–518, 2003.

[10] M. Rahman and S. Majumder, "Analysis of a Power Line Communication System Over a Non-white Additive Gaussian Noise Channel and Performance Improvement Using Diversity Reception." in *2011 IEEE Symposium on Industrial Electronics and Applications (ISIEA)*, 2011, pp. 304–307.

[11] Y. H. Ma, P. L. So, and E. Gunawan, "Performance Analysis of OFDM Systems for Broadband Power Line Communication Under Impulsive Noises and Multipath Effects," *IEEE Transactions on Power Delivery*, vol. 20, no. 2, pp. 674–681, 2005.

[12] S. W. Lai and G. G. Messier, "Using the wireless and PLC channels for diversity," *IEEE Transactions on Communications*, vol. 60, no. 12, pp. 3865–3874, 2012.

[13] J.-h. Lee and Y.-h. Kim, "Diversity Relaying for Parallel Use of Power-Line and Wireless Communication Networks," *IEEE Transactions on Power Delivery*, vol. 29, no. 3, pp. 1301–1310, 2014.

[14] O. A. Gonzalez, J. Urminsky, M. Calvo, and L. D. Haro, "Performance analysis of hybrid broadband access technologies using PLC and Wi-Fi," in *International Conference on Wireless Networks, Communications and Mobile Computing*, 2005, pp. 564–569.

[15] M. Sayed and N. Al-Dhahir, "Narrowband-plc/wireless diversity for smart grid communications," in *2014 IEEE Global Communications Conference*, Dec 2014, pp. 2966–2971.

[16] ——, "Differential modulation diversity combining for hybrid narrowband-powerline/wireless smart grid communications," in *2016 IEEE Global Conference on Signal and Information Processing (GlobalSIP)*, Dec 2016, pp. 876–880.

[17] S. W. Lai and G. G. Messier, "Using the wireless and plc channels for diversity," *IEEE Transactions on Communications*, vol. 60, no. 12, pp. 3865–3875, December 2012.

[18] T. R. Oliveira, C. A. Marques, M. S. Pereira, S. L. Netto, and M. V. Ribeiro, "The Characterization of Hybrid PLC-Wireless Channels: A Preliminary Analysis," *2013 IEEE 17th International Symposium on Power Line Communications and Its Applications (ISPLC2013)*, pp. 98–102, 2013.

[19] Luis Guilherme, Thiago Oliveira, Fernando J. A. Andrade, Michelle Pereira, and Moises Vidal Ribeiro, "Measurement of Hybrid PLC-wireless Channels for Indoor and Broadband Data Communication," in *Simpósio Brasileiro de Telecomunicações (SBrT2013)*, 2013, pp. 1–5.

[20] M. Ribeiro, H. Latchman, F. Andrade, T. Oliveira, S. Lima Netto, and A. Picorone, "Characterization of Hybrid Communication Channel in Indoor Scenario," *Journal of Communication and Information Systems*, vol. 31, no. 1, pp. 224–235, 2016.

[21] M. Zimmermann and K. Dostert, "A Multipath for the Powerline Channel," *IEEE Transactions on Communications*, vol. 50, no. 4, pp. 553–559, 2002.

[22] W. Zhu, X. Zhu, E. Lim, and Y. Huang, "State-of-art power line communications channel modelling," *Procedia Computer Science*, vol. 17, pp. 563–570, 2013.

[23] H. C. Ferreira, L. Lampe, J. Lampe, and T. G. Swart, *Powerline Communications: Theory and Applications for Narrowband and Broadband Communications over Powerline*, 1st ed. Torquay, UK: John Wiley and Sons, 2010.

[24] L. Lampe, A. M. Tonello, and J. G. Swart, *Power Line Communications: Principles: Standards and Applications from Multimedia to Smart Grid*, 2nd ed. West Sussex, UK: John Wiley and Sons, 2016.

[25] F. Zwane and T. J. O. Afullo, "Power Line Communication Channel Modelling: Establishing the Channel Characteristics," in *South African Universities Power Engineering*

Conference (SAUPEC2014), Durban, South Africa, 2014, pp. 505–509.

[26] A. M. Tonello, F. Versolatto, and A. Pittolo, "In-home power line communication channel: Statistical characterization," *IEEE Transactions on Communications*, vol. 62, no. 6, pp. 2096–2106, 2014.

[27] S. Galli, "A novel approach to the statistical modeling of wireline channels," *IEEE Transactions on Communications*, vol. 59, no. 5, pp. 1332–1345, 2011.

[28] H. Philipps, "Modelling of powerline communication channels," in *International Symposium on PowerLine Communication and its Applications*, Lancaster, UK, 1999.

[29] S. Galli and T. C. Banwell, "A deterministic frequency-domain model for the indoor power line transfer function," *IEEE Journal on Selected Areas in Communications*, vol. 24, no. 7, pp. 1304–1315, 2014.

[30] J. A. Corchado, J. A. Cortes, F. J. Canete, and L. Diez, "An MTL-Based Channel Model for Indoor Broadband MIMO Power Line Communications," *IEEE Journal on Selected Areas in Communications*, vol. 34, no. 7, pp. 2045–2055, 2016.

[31] M. Zimmermann and K. Dostert, "Analysis and Modeling of Impulsive Noise in Broad-Band Powerline Communications," *IEEE Transactions on Electromagnetic Compatability*, vol. 44, no. 1, pp. 250–258, 2002.

[32] K. Khalil, P. Corlay, F.-x. Coudoux, M. G. Gazalet, and M. Gharbi, "Analysis of the Impact of Impulsive Noise Parameters on BER Performance of OFDM Power-Line Communications," pp. 1–4, 2010.

[33] S. A. Bhatti, Q. Shan, I. A. Glover, R. Atkinson, I. E. Portugues, P. J. Moore, and R. Rutherford, "Impulsive noise modelling and prediction of its impact on the performance of WLAN receiver," in *European Signal Processing Conference (EUSIPCO)*, no. 17, Glasgow, Scotland, 2009, pp. 1680–1684.

[34] M. O. Asiyo and T. J. O. Afullo, "Analysis of Bursty Impulsive Noise in Low-Voltage Indoor Power Line Communication Channels: Local Scalling Behaviour," *South African Institute of Electrical Engineers*, vol. 108, no. 3, pp. 98–107, 2017.

[35] U. R. C. Vitor and M. T. de Melo, "Comparison between power line communication multipath model and coaxial cable interferometer theory," *International Journal of Communication Systems*, vol. 30, no. 1, pp. 151–162, 2012.

[36] R. Abenov, D. Pokamestov, and A. Geltser, "Multipath powerline communications channel (PLC) modelling," *2015 IEEE International Conference on Microwaves, Communications, Antennas and Electronic Systems (COMCAS2015)*, pp. 2–4, November 2015.

[37] C. Paul, *Analysis of Multiconductor Transmission Lines*, 2nd ed. New Jersey: John Wiley and Sons, 2008.

[38] F. T. Ulaby, A. Michielssen, and U. Ravaioli, *Fundamentals of Applied Elecctromagnetic*, 6th ed. West Sussex, UK: Pearson, 2010.

[39] A. Voglgsang, T. Langguth, G. Korner, H. Steckenbiller, and R. Knorr, "Measurement, Characterization and Simulation of Noise on Powerline Channels," in *International Symposium on PowerLine Communication and its Applications*, 2000, pp. 139–146.

[40] A. Paulraj, R. Nabar, and D. Gore, *Introduction to Space-Time Wireless Communications*, 1st ed. Cambridge University Press, 2003.

[41] R. Deepa, K. Baskaran, P. Unnikrishnan, and A. Kumar, "Study of Spatial Diversity Schemes in Multiple Antenna Systems," *Journal of Theoretical and Applied Information Technology*, vol. 5, no. 5, pp. 619–624, 2009.

[42] J. Ghosh, A. Dey, and S. Bachhar, "Performance Analysis by Improving Bit Error Rate (BER) through various Diversity Techniques in Wireless Communication," *International Journal of Computer Applications*, vol. 95, no. 9, pp. 1–5, 2014.

[43] H. Ma, L. Lampe, and S. Hranilovic, "Hybrid visible light and power line communication for indoor multiuser downlink," *IEEE/OSA Journal of Optical Communications and Networking*, vol. 9, no. 8, pp. 635–647, Aug 2017.

[44] M. B. Rahaim, A. M. Vegni, and T. D. C. Little, "A hybrid radio frequency and broadcast visible light communication system," in *2011 IEEE GLOBECOM Workshops (GC Wkshps)*, Dec 2011, pp. 792–796.

[45] J. A. Cortes, L. Diez, F. J. Canete, and J. J. Sanchez-Martinez, "Analysis of the indoor broadband power-line noise scenario," *IEEE Transactions on Electromagnetic Compatibility*, vol. 52, no. 4, pp. 849–858, Nov 2010.

[46] S. M. Nlom, A. R. Ndjiongue, and K. Ouahada, "Cascaded plc-vlc channel: An indoor measurements campaign," *IEEE Access*, vol. 6, pp. 25 230–25 239, 2018.

[47] H. Ma, L. Lampe, and S. Hranilovic, "Coordinated broadcasting for multiuser indoor visible light communication systems," *IEEE Transactions on Communications*, vol. 63, no. 9, pp. 3313–3324, Sep. 2015.

[48] O. A. Gonzalez, J. Urminsky, M. Calvo, and L. de Haro, "Performance analysis of hybrid broadband access technologies using plc and wi-fi," in *2005 International Conference on Wireless Networks, Communications and Mobile Computing*, vol. 1, June 2005, pp. 564–569 vol.1.

[49] S. W. Lai, N. Shabehpour, G. G. Messier, and L. Lampe, "Performance of wireless/power line media diversity in the office environment," in *2014 IEEE Global Communications Conference*, Dec 2014, pp. 2972–2976.

[50] B. Tan and J. Thompson, "Relay transmission protocols for in-door powerline communications networks," in *2011 IEEE International Conference on Communications Workshops (ICC)*, June 2011, pp. 1–5.

[51] W. Gheth, K. M. Rabie, B. Adebisi, M. Ijaz, G. Harris, and A. Alfitouri, "Hybrid power-

line/wireless communication systems for indoor applications," in *2018 11th International Symposium on Communication Systems, Networks Digital Signal Processing (CSNDSP)*, July 2018, pp. 1–6.

[52] D. Middleton, "Statistical-physical model of electromagnetic interference," *IEEE Transactions on Electromagnetic Compatibility*, vol. 19, no. 3, pp. 106–126, 1977.

[53] R. Kant, Z. Alam, and P. K. Verma, "Modelling and Simulation of Noise Effects in Power Line Communications," *International Journal of Research and Engineering*, vol. 03, no. 11, pp. 6–12, 2016.

[54] M. Ghosh, "Analysis of the effect of impulse noise on multicarrier and single carrier QAM systems," *IEEE Transactions on Communications*, vol. 44, no. 2, pp. 145–147, 1996.

[55] B. P. Lathi and Z. Dhing, *Modern Digital and Analog Communication Systems*, 4th ed. Oxford University Press, 2010.

[56] A. H. Najarkolaei, W. Hosny, and J. Lota, "Bit Error Rate Performance in Power Line Communication Channels with Impulsive Noise," *2015 17th UKSim-AMSS International Conference on Modelling and Simulation (UKSim)*, pp. 248–251, 20.

[57] L. Wang, G. Deconinck, and E. V. Lil, "Performance analysis of Broadband Power line Communications under impulsive noise and crosstalk," in *2012 URSI Benelux Conference on Telecommuication and Microwaves*, no. 10, Brussels, 2012, pp. 1–3.

[58] A. A. Arowojolu, A. M. D. Turkmani, A. A. Arowojolu, A. M. D. Turkmani, P. A. Jefford, and C. J. Kellett, "An Experimental Evaluation of the Performance of Two-Branch Space and Polarization Diversity Schemes at 1800 MHz," *IEEE Transactions on Vehicular Technology*, vol. 44, no. 2, pp. 318–326, 1995.

[59] Q. T. Zhang, "Probability of error for equal-gain combiners over rayleigh channels: some closed-form solutions," *IEEE Transactions on Communications*, vol. 45, no. 3, pp. 270–273, 1997.

[60] S. M. Alamouti, "A simple transmit diversity technique for wireless communications," *IEEE Journal on Selected Areas in Communications*, vol. 16, no. 8, pp. 1451–1458, 1998.

[61] Y. Wu and J. P. Linnartz, "Effects of Antenna Mutual Coupling on the Performance of MIMO Systems," *29th Symposium on Information Theory in the Benelux*, pp. 1–8, May 2008.

[62] X. Chen, S. Zhang, and Q. Li, "A Review of Mutual Coupling in MIMO Systems," *IEEE Access*, vol. 6, pp. 24 706–24 719, 2018.

[63] X. Cuiwei, Z. Qiuming, C. Xiaomin, L. Xinglin, and Y. Ying, "Effect of Mutual Coupling on Multiple Antenna Channel," *International Journal of Modeling and Optimization*, vol. 6, no. 4, pp. 252–255, 2016.

[64] Y. Wu, J. W. Bergmans, and S. Attallah, "Effects of antenna correlation and mutual coupling on the carrier frequency offset estimation in MIMO systems," *2010 6th International Conference on Wireless Communications, Networking and Mobile Computing (WiCOM2010)*, 2010.

[65] H. Shi, S. Gong, and T. Zheng, "The effect of mutual coupling on the channel performance of MIMO communication system," *2012 10th International Symposium on Antennas, Propagation and EM Theory (ISAPE 2012)*, pp. 335–339, 2012.

[66] V. S. Abhayawardhana, I. J. Wassell, D. Crosby, M. P. Sellars, and M. G. Brown, "Comparison of empirical propagation path loss models for fixed wireless access systems," in *2005 IEEE 61st Vehicular Technology Conference*, vol. 1, May 2005, pp. 73–77.

[67] V. Erceg, "TGn channel models," in *IEEE 802.11 document 802.11-03/940r4*.

[68] A. A. Abouda, H. M. El-Sallabi, and S. G. Haggman, "Effect of mutual coupling on ber performance of alamouti scheme," in *2006 IEEE Antennas and Propagation Society International Symposium*, July 2006, pp. 4797–4800.

[69] J. D. Parsons, D. A. Demery, and A. M. D. Turkmani, “Sounding techniques for wideband mobile radio channels: a review,” *IEE Proceedings I - Communications, Speech and Vision*, vol. 138, no. 5, pp. 437–446, Oct 1991.

[70] R. J. Pirkl and G. D. Durgin, “Optimal sliding correlator channel sounder design,” *IEEE Transactions on Wireless Communications*, vol. 7, no. 9, pp. 3488–3497, Sep. 2008.

[71] N. Benvenuto, “Distortion analysis on measuring the impulse response of a system using a crosscorrelation method,” *AT T Bell Laboratories Technical Journal*, vol. 63, no. 10, pp. 2171–2192, Dec 1984.

[72] J. Talvitie and T. Poutanen, “Self-noise as a factor limiting the dynamic range in impulse response measurements using sliding correlation,” in *Proceedings of IEEE 3rd International Symposium on Spread Spectrum Techniques and Applications (ISSSTA'94)*, vol. 2, July 1994, pp. 619–623.

[73] G. Martin, “Wideband channel sounding dynamic range using a sliding correlator,” in *VTC2000-Spring. 2000 IEEE 51st Vehicular Technology Conference Proceedings (Cat. No.00CH37026)*, vol. 3, May 2000, pp. 2517–2521.

[74] A. M. Tonello and F. Versolatto, “Bottom-up statistical PLC channel modeling - Part II: Inferring the statistics,” *IEEE Transactions on Power Delivery*, vol. 25, no. 4, pp. 2356–2363, 2010.

[75] G. Martin, “Wideband Channel Sounding Dynamic Range using a Sliding Correlator,” in *VTC 2000 - Spring*, Piscataway, NJ, 2000, pp. 2517–2521.

[76] R. C. Dixon, *Spread Spectrum Systems with Commercial Applications.* John Wiley and Sons, 1994.

[77] P. A. Janse Van Rensburg, “Effective Coupling for Power-Line Communications,” D.Ing (Electrical and Electronic), University of Johannesburg, 2008.

[78] J. Sadowski, "Measurement of Coherence Bandwidth in UHF Radio Channels for Narrowband Networks," *International Journal of Antennas and Propagation*, vol. 2015, pp. 3–5, 2015.

[79] M. Tlich, A. Zeddam, F. Moulin, and F. Gauthier, "Indoor power-line communications channel characterization up to 100 MHz-Part II: Time-frequency analysis," *IEEE Transactions on Power Delivery*, vol. 23, no. 3, pp. 1402–1409, 2008.

[80] T. R. Oliveira, A. A. Picorone, C. B. Zeller, S. L. Netto, and M. V. Ribeiro, "On the statistical characterization of hybrid PLC-wireless channels," *Electric Power Systems Research*, vol. 163, pp. 329–337, 2018.

[81] A. M. Tonello and F. Versolatto, "Bottom-up statistical PLC channel modeling-part I: Random topology model and efficient transfer function computation," *IEEE Transactions on Power Delivery*, vol. 26, no. 2, pp. 891–898, 2011.

[82] E. G. Bakhoum, "S-parameters model for data communications over 3-phase transmission lines," *IEEE Transactions on Smart Grid*, vol. 2, no. 4, pp. 615–623, 2011.

[83] J. J. Sánchez-Martínez, J. A. Cortés, L. Díez, F. J. Cañete, and L. M. Torres, "Performance analysis of ofdm modulation on indoor plc channels in the frequency band up to 210 mhz," in *2010 IEEE 17th International Symposium on Power Line Communications and Its Applications (ISPLC2010)*, March 2010, pp. 38–43.

[84] K. M. Rabie and E. Alsusae, "On improving communication robustness in plc systems for more reliable smart grid applications," *IEEE Transactions on Smart Grid*, vol. 6, no. 6, pp. 2746–2756, Nov 2015.

[85] A. M. Tonello, S. D'Alessandro, and L. Lampe, "Cyclic prefix design and allocation in bit-loaded ofdm over power line communication channels," *IEEE Transactions on Communications*, vol. 58, no. 11, pp. 3265–3276, November 2010.

[86] B. Adebisi, K. M. Rabie, A. Ikpehai, C. Soltanpur, and A. Wells, "Vector ofdm trans-

mission over non-gaussian power line communication channels," *IEEE Systems Journal*, vol. 12, no. 3, pp. 2344–2352, Sep. 2018.

[87] J. A. Cortés, F. J. Cañete, L. Diez, L. M. Torres, and S. L. M. Hispania, "On plc channel models: An ofdm-based comparison," in *2013 IEEE 17th International Symposium on Power Line Communications and Its Applications*, March 2013, pp. 333–338.

[88] A. A. Atayero, A. A. Alatishe, and Y. A. Ivanov, "Power Line Communication Technologies : Modeling and Simulation of PRIME Physical Layer," in *World Congress on Engineering and Computer Science*, vol. 2, San Francisco, USA, 2012.

[89] J. S. Lee, H. Oh, J. Kim, and J. Y. Kim, "Performance of scaled slm for papr reduction of ofdm signal in plc channels," in *2009 IEEE International Symposium on Power Line Communications and Its Applications*, March 2009, pp. 166–170.

[90] T. T. Nguyen and L. Lampe, "On partial transmit sequences for par reduction in ofdm systems," *IEEE Transactions on Wireless Communications*, vol. 7, no. 2, pp. 746–755, February 2008.

[91] S. Weinstein and P. Ebert, "Data transmission by frequency-division multiplexing using the discrete fourier transform," *IEEE Transactions on Communication Technology*, vol. 19, no. 5, pp. 628–634, October 1971.

[92] A. Peled and A. Ruiz, "Frequency domain data transmission using reduced computational complexity algorithms," in *ICASSP '80. IEEE International Conference on Acoustics, Speech, and Signal Processing*, vol. 5, April 1980, pp. 964–967.

[93] T. M. Schmidl and D. C. Cox, "Robust frequency and timing synchronization for OFDM," *IEEE Transactions on Communications*, vol. 45, no. 12, pp. 1613–1621, 1997.

[94] L. Guilherme, S. Costa, A. C. M. D. Queiroz, B. Adebisi, V. L. R. Costa, and M. V. Ribeiro, "Coupling for Power Line Communication : A Survey," *Journal of Communication and Information Systems*, vol. 32, no. 1, pp. 8–22, 2017.

[95] D. Gesbert, H. Bolcskei, D. A. Gore, and A. J. Paulraj, "Outdoor mimo wireless channels: models and performance prediction," *IEEE Transactions on Communications*, vol. 50, no. 12, pp. 1926–1934, Dec 2002.